INTERACTION OF HYDROGEN WITH TITANIUM DIOXIDE AND
PALLADIUM-TITANIUM DIOXIDE SURFACE AT LOW AND HIGH
TEMPERATURE

A THESIS SUBMITTED TO
THE GRADUATE SCHOOL OF NATURAL AND APPLIED SCIENCES
OF
MIDDLE EAST TECHNICAL UNIVERSITY

BY

MELİS YARAR

IN PARTIAL FULFILLMENT OF THE REQUIREMENTS
FOR
THE DEGREE OF MASTER OF SCIENCE
IN
CHEMICAL ENGINEERING

JUNE 2022

Approval of the thesis:

INTERACTION OF HYDROGEN WITH TITANIUM DIOXIDE AND PALLADIUM-TITANIUM DIOXIDE SURFACE AT LOW AND HIGH TEMPERATURE

submitted by **MELİS YARAR** in partial fulfillment of the requirements for the degree of **Master of Science** in **Chemical Engineering, Middle East Technical University** by,

Prof. Dr. Halil Kalıpçılar
Dean, Graduate School of **Natural and Applied Sciences**   _____

Prof. Dr. Pınar Çalık
Head of the Department, **Chemical Engineering**   _____

Prof. Dr. Deniz Üner
Supervisor, **Chemical Engineering, METU**   _____

Examining Committee Members:

Prof. Dr. Gürkan Karakaş
Chemical Engineering, METU   _____

Prof. Dr. Deniz Üner
Chemical Engineering, METU   _____

Prof. Dr. Christoph Müller
Mechanical and Process Engineering, ETH Zürich   _____

Asst. Prof. Dr. Gökhan Çelik
Chemical Engineering, METU   _____

Asst. Prof. Dr. Necip Berker Üner
Chemical Engineering, METU   _____

Date: 20.06.2022

I hereby declare that all information in this document has been obtained and presented in accordance with academic rules and ethical conduct. I also declare that, as required by these rules and conduct, I have fully cited and referenced all material and results that are not original to this work.

Name Last name : Melis Yarar

Signature :

ABSTRACT

INTERACTION OF HYDROGEN WITH TITANIUM DIOXIDE AND PALLADIUM-TITANIUM DIOXIDE SURFACE AT LOW AND HIGH TEMPERATURE

Yarar, Melis
Master of Science, Chemical Engineering
Supervisor : Prof. Dr. Deniz Üner

June 2022, 123 pages

In this work, the role of Pd loading on the Pd morphology and subsequent reactivity of Pd/TiO_2 catalyst for CO oxidation and titania surface reduction were investigated. 2D patches of Pd metal were identified on titania surface at low loadings ($\leq 2\%$). 2D patches give rise to mild-temperature and low pressure reduction of titania surface. In the presence of 2D Pd room temperature reduction was studied with quantitative Temperature Programmed Reduction (TPR) measurement which revealed that 70% of titania surface on $1\%Pd/TiO_2$ was reduced at 300K, owing to Pd acting as a reduction promoter. Pd metal phase change from 2D to 3D with increasing Pd amount was identified by quantitative TPR analysis and HR-TEM measurements. Rate of room temperature reduction of titania surface by hydrogen spillover process disclosed by TPR analyses was found to be directly correlated with the surface area of Pd structures for $\leq 2\%$ Pd loaded samples. Consequently for 2D particles, atomic hydrogen exhange between metal and support was taking place all through the surface area of metal. Paramagnetic centers formed during hydrogen exposure was monitored with *in-situ* room-temperature Electron Spin Resonance

(ESR) Spectroscopy technique. The oxygen vacancies and Ti^{+3} species was only detected on low Pd loadings and under vacuum condition. The dependency of ESR signal on pressure was studied with saturation-recovery continous wave ESR experiments which revealed regulation of spin-lattice relaxation time with pressure decrease. Hydrogen spillover process was monitored with operando Nuclear Magnetic Resonance (NMR) spectroscopy and it was modelled using hydroxyl signal growth rate. CO oxidation measurements were conducted to reveal changes in catalytic activity by nanoscale nature of the Pd/TiO_2 catalyst. In particular, increase in Pd loading in 2D region increased CO conversion substantially while increasing Pd loading when Pd is 3D no significant change occurred.

On the other hand, at high temperature hydrogen reduction was found to led to phase change and Magnéli phase production. The phase boundary between $Ti_{11}O_{21}$ and anatase or rutile phases was found to be able to accommodate hydrogen and release when the temperature was changed.

Keywords: Titanium Dioxide, 2-D Materials, Electron Spin Resonance Spectroscopy, Magnéli Phase

ÖZ

HİDROJENİN DÜŞÜK VE YÜKSEK SICAKLIKTA TİTANYUM DİOKSİT VE PALADYUM-TİTANYUM DİOKSİT YÜZEYLERİYLE ETKİLEŞİMİ

Yarar, Melis
Yüksek Lisans, Kimya Mühendisliği
Tez Yöneticisi: Prof. Dr. Deniz Üner

Haziran 2022, 123 sayfa

Bu çalışmada, Pd yükleme miktarının Pd morfolojisi ve buna bağlı Pd/TiO$_2$ katalizörünün reaktivitesi üzerine etkisi incelenmiştir. Düşük metal yüklemeli (≤2%) örneklerde 2 boyutlu Pd parçalarının TiO$_2$ yüzeyinin düşük basınç ve sıcaklıkta hidrojenle indirgenmesini sağladığı görülmüştür. Oda sıcaklığında hidrojenle indirgenme Sıcaklık Programlı İndirgeme (TPR) cihazıyla izlenmiş ve nicel ölçümler Pd'un indirgenme destekçisi olarak görev yaparak 300K'de 1%Pd/TiO$_2$ yüzeyinin %70'inin indirgenmesine yol açtığını göstermiştir. Nicel TPR ölçümleri, Yüksek Çözünürlüklü Transmisyon Elektron Mikroskopu görüntüleriyle uyumlu şekilde, Pd yükleme miktarı arttıkça Pd yapılarının iki boyutludan üç boyutluya dönüşmelerine yol açtığını kanıtlamıştır. TPR ölçümleriyle varılan sonuçlara göre iki boyutlu Pd'a sahip örneklerde (≤2%) oda sıcaklığındaki indirgenme Pd yüzey alanı ile doğrudan orantılıdır. Buna dayanarak, iki boyutlu örneklerde metal ve destek arasındaki atomik hidrojen alışverişinin metalin tüm yüzey alanı boyunca gerçekleştiği kanıtlanmıştır. Hidrojenleme sonrası oluşan paramanyetik merkezler oda sıcaklığında *in-situ* Elektron Spin Rezonans (ESR) Spektroskopisi ile takip edilmiştir. Oksijen vacancy ve Ti^{+3} merkezleri sadece düşük

Pd yüklemeli örneklerde ve vakum koşulunda gözlemlenmiştir. Saturation-Recovery ESR deneyleriyle bu sinyallerin basınç ile ilişkisi izlenmiş ve spin-lattice relaxation zaman sabitinin basınca bağlı değiştiği gözlemlenmiştir. Hidrojen spillover süreci *operando* Nükleer Manyetik Rezonans (NMR) Spektroskopisi ile takip edilmiş ve hidroksil sinyalinin büyüme hızına göre modellenmiştir. Katalitik CO oksidasyonu ölçümleri nano düzeyde meydana gelen değişiklerin aktiviteye etkisini anlamak amacıyla gerçekleştirilmiştir. Aktivitenin iki boyutlu yapılarda metal eklenmesi ile büyük oranda arttığı ancak üç boyutlu örneklerde bir değişime uğramadığı sonucuna varılmıştır.

Öte yandan, yüksek sıcaklıktaki hidrojenle indirgemenin faz değişimine ve Magnéli fazı üretimine yol açtığı görülmüştür. Açığa çıkan $Ti_{11}O_{21}$ fazı ve anataz veya rutil fazı arasındaki yüzeyin hidrojen tutabildiği ve sıcaklık değişince hidrojeni salabildiği görülmüştür.

Anahtar Kelimeler: Titanyum dioksit, 2-boyutlu Materyaller, Elektron Spin Rezonans Spektroskopisi, Magnéli Fazı

To my grandfather

ACKNOWLEDGMENTS

Firstly, I would like to express my deepest gratitude to my supervisor Prof. Dr. Deniz Üner who has humbly let me in her research group as an undergraduate student and being the source of wisdom and endless motivation ever since. She has enlightened me not only academically but in all facets of life. I cannot thank her enough for inspiring my enthusiasm for research and sharing the excitement of discovery.

Further, I would like to present my warmest thanks to all Uner group members. I am grateful to Begüm Yılmaz, Selin Ernam and Elif Ferligül for their help and guidance in laboratory and valuable friendship. I thank Dr. Atalay Çalışan for his help with TPR and CO oxidation and Dr. Asmae Bouziani for her help with TPR and NMR. I acknowledge the technical assistance of İsa Çağlar for his help with the equipment I have benefitted during my research.

I would like to give special thanks to Hasan Ertürk and İlker Delibaş, for sticking with me. I wouldn't enjoy the last seven years enough if it wasn't for them. I thank my dear friend Betül Sena Süzen for the laughter and support she provided since the undergraduate. I was lucky to have Beste Avcı, my dear roommate. I am grateful for my childhood friends Buse Dinçer, Özge Özlem, Sıla Taşoğlu, İrem Bilgin; to feel their friendship close no matter we are physically far apart is precious.

Above all, I am the luckiest to be the daughter of Özlem and Kenan Yarar. My gratitude for them can never be expressed in words. I am thankful for having my grandfather: Abdurrahman, the mastermind of the family and my inspiration.

Lastly, I am grateful for having Su in my life; all the unforgettable memories and endless and unconditional love she provided for fifteen years and hopefully more.

TABLE OF CONTENTS

LIST OF TABLES

LIST OF FIGURES

FIGURES

xvii

LIST OF SYMBOLS

SYMBOLS

b	Line shape factor for ESR signal
BET	Brunauer–Emmett–Teller
CW	Continuous Wave
EPR	Electron Paramagnetic Resonance
ESR	Electron Spin Resonance
h	Planck's constant
HCTEM	High-Contrast Transmission Electron Microscopy
HRTEM	High-Resolution Transmission Electron Microscopy
ICP-OES	Inductively Coupled Plasma - Optical Emission Spectrometry
I	ESR signal intensity
k	Boltzmann's constant
m	Mass
N_{lower}	Number of spins at lower energy state of Zeeman Splitting
NMR	Nuclear Magnetic Resonance
N_{upper}	Number of spins at upper energy state of Zeeman Splitting
TCD	Thermal conductivity detector
P	Microwave power
TPR	Temperature programmed reduction
UV	Ultraviolet
ν	frequency
XRD	X-ray diffraction crystallography

CHAPTER 1

INTRODUCTION

1.1   Titanium Dioxide

Owing to its chemical stability, non-toxicity and economic viability, titanium dioxide has been used across a wide spectrum of industries such as paint[1], cosmetics[2], plastics, paper, medical[3] as well as applications like gas sensors[4,5], solar cells[6,7], batteries[8], air-water purification[9]. Along with this broad range of applications, it was addressed by an accelerating number of research activities focusing on its use as a catalyst since 1970s. Its stable oxidation states and surface defects are the key features that make titanium dioxide, also named as titania, such a highly investigated catalyst. Titania is a semiconductor having a molecular orbital bonding structure that valence and conduction bands formed by oxygen 2p and titanium 3d states[10,11]. A respective bandgap 3.2 eV makes titania active only under irradiation of a wavelength in ultraviolet region of the electromagnetic spectrum[12]. Upon absorption of UV irradiation, electrons primarily in valence band are excited to unoccupied conduction band[10,12]. The photogenerated electrons are created and positively charged holes are left in valence band. In the conduction band electrons can reduce Ti^{+4} species to Ti^{+3} while O^{2-} species converted to O^- in the holes in valence band[13]. The process can be summarised by the following reaction scheme:

$$TiO_2 \xrightarrow{h\upsilon} e^- + h^+$$

$$Ti^{+4} + e^- \rightarrow Ti^{+3}$$

$$O^{2-} + h^+ \rightarrow O^-$$
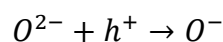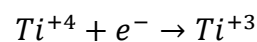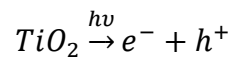
If not prevented, these charge carriers recombine very quickly, in fact in about 30ns[14]. If not recombined, they can react with adsorbed species on the catalyst surface. Additionally, if holes completely oxidise O^{2-} species, formed O_2 molecules can desorb from surface leaving an oxygen vacancy behind[10]. Oxygen vacancies and Ti^{+3} species are the most important defect sites on titania structure.

1.2   Defects in Titania Structure

Defects in catalyst structures have known to be affecting the catalytic activity by regulating the chemical environment around the reactive interface[15]. As well as catalytic activity; electronic, optical, mechanical and physical properties of the materials have been reported to be enhanced by the introduction of defects in the structure[16,17]. The potential that these defective sites possess even lead to the emergence of a new discipline called 'Defect Engineering' which focuses on implementation of defects in order to improve the properties of the materials. Correspondingly, the characteristics of titania depend on the presence of defects, prominently: oxygen vacancies. In fact, oxygen vacancies in titania structure were attributed as "fingerprints of electronic structure" by Pacchioni [18] due to its ability to manipulate oxidation state as the formation of oxygen vacancies is accompanied by reduction of Ti^{+4} to Ti^{+3}. As explained by Pacchioni, when an oxygen vacancy is formed by removal of O from structure, resulting electrons are moved to conduction band of neighbouring Ti atoms where a reduction from Ti^{+4} to Ti^{+3} takes place which leads to a shift in binding energy as well as formation of paramagnetic centers.

There are numerous studies in literature that report enhancements in catalytic properties of titania by defect formation. Color change of titania after UV illimanation was first observed by Renz [19]. Since the pioneer discovery of Fujishima and Honda[20] which revealed titania is an effective photocatalyst for water splitting reaction, many efforts were dedicated to shift absorption capability of titania from UV to visible region.

Soon later oxygen vacancies and Ti^{+3} species found to possess visible light absorption characteristics[21–24]. Along with visible light absorption, oxygen vacancies and Ti^{+3} centers were discovered to be preventing recombination of charge carriers produced upon irradiation[25,26]. Park et al.[27] explained the role of defects to prevent recombination of charge carriers as they trap electrons and holes produced which enhances the reactions that proceed through participation of e^-/h^+ pairs. In addition to photocatalytic activity, defects were found to be dissociative adsorption sites for many reactants as they create a charge imbalance and localized electron clouds around the defective sites[24,28]. Moreover, oxygen vacancies have the ability to reduce metals adsorbed. Pan et al.[29] showed oxygen vacancies can immediately reduce gold particles deposited on defective sites as they can easily transfer electrons onto gold ions.

In addition to UV irradiation, several methods were suggested to be effective to create surface defects on titania such as: thermal treatment coupled with reductive H_2 atmosphere[30,31], vacuum annealing[32,33], high energy particle bombardment [34–36], etc. Among all the suggested methods, thermal treatment at pressurized hydrogen atmosphere is the most studied which led to the emergence of 'black titania' studies as well as the discovery of a special group of titania sub-oxides which are classified as Magnéli phases.

1.3   Objectives

In this study, formation of defective Pd supported titania at high and low temperatures under hydrogen atmosphere which correspond to the formation of Magnéli phase and black titania equivalents, respectively was studied to reveal the effect of Pd loading, dispersion and nanoscale nature of the metal. The process was monitored *in-situ* by Electron Spin Resonance (ESR) Spectroscopy and *operando* by Nuclear Magnetic Resonance (NMR) Spectroscopy; while reduction principles were studied with Temperature Programmed Reduction (TPR) analysis and reaction tests was done by CO oxidation.

CHAPTER 2

LITERATURE REVIEW

2.1   Black Titania

In 2011, black titania term was introduced to titania literature by Chen et al. [37] after realising titania's colour turn into black when treated with hydrogen gas under elevated pressure and temperature as well as many defects are formed. Also, this new material has the ability to interact with visible light. Similar ways this material was synthesised and properties were examined by many others[38–41]. Black titania's superior properties to white titania were found to be arise from disordered core-shell structure[41–43] and high content of oxygen vacancies and Ti^{+3} species[30,40]. Many groups have shown that black titania can be synthesised under H_2 atmosphere with temperatures as high as 600°C and in time scales of around 3 hours[38]. Hydrogen calcination, plasma treatment [44,45], reduction in the presence of metal atoms [46], electrochemical processes [47,48] are other suggested methods. As seen, the methods previously mentioned are mostly rather sophisticated. Hence, a great effort was spent to come up with easier ways to synthesise black titania over time. As a result of all the work studied black titania synthesis, finally in 2016, Xu et al. [49] synthesised titania which is high in defect concentration and black at room temperature with the help of Pd on titania surface.

2.2   Magnéli Phases of Titania

Magnéli phase refers to a group of compounds having Ti_nO_{2n-1} stoichiometry which is synthesized at a reducing gas or metal atmosphere at temperatures as high as 1000K or above[50–52]. Formation reaction of Magnéli phases was summarised by Walsh and Wills as[53]:

$$n\,TiO_2 + H_2 \leftrightarrow Ti_xO_{2n-1} + H_2O$$
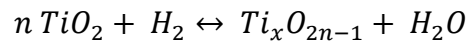
These phases of titania have proven to exhibit distinct electrical and optical properties over the years[54–57]. Due their high stability and activity Magnéli phases are frequently used as chemical catalysts[58,59]. They are considered as good candidates for electrodes due to their high dielectric constant, which caused them to be employed in the development of electronic devices[60–62].

Although the enhanced properties of Magnéli phases caused them to be used in many applications and hence these structures were highly studied, still, how the boundary between Magnéli phase and TiO_2 formed during synthesis of the subject phases behaves has not been demonstrated, yet. A phase diagram of Ti-O is given below:
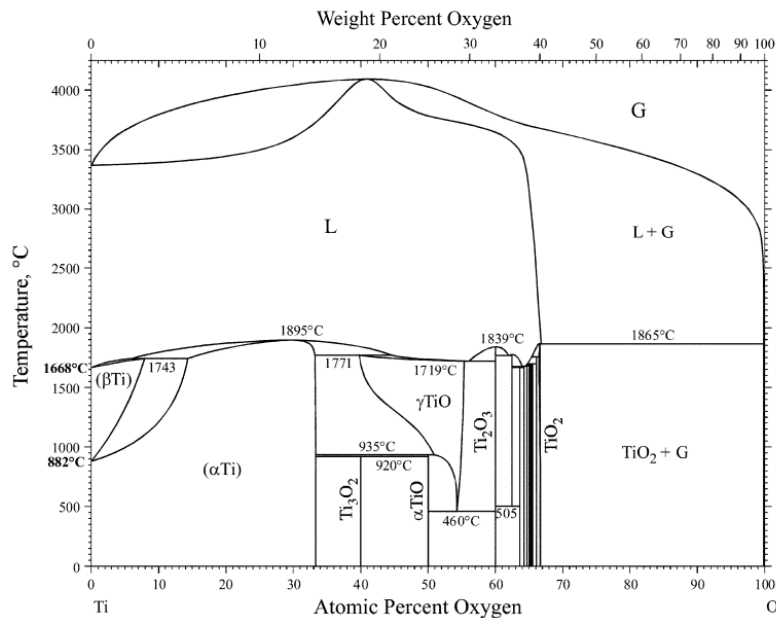
Figure 2.1. Ti-O phase diagram [63]

6

2.3   Hydrogenation of Palladium

Supported Pd is known to be exist in PdO form which is first reduced by hydrogen to form water and metallic Pd[64–68]:

$$PdO + \ H_2 \ \rightarrow H_2O + Pd$$
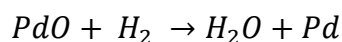
As shown by Martin et al.[65] immediately after PdO surface is exposed to hydrogen at 300K, firstly hydroxyl groups are formed, via dissociation of hydrogen on Pd atoms, which may react with another H atom to be desorbed as H_2O. As more oxide is reduced, more sites for H-dissociation becomes available which result in acceleration of the reduction reaction. Furthermore, dissociated hydrogen atoms diffuse into the interstitial sites of Pd structure to form palladium hydride[64,66,67]:

$$H_2 \xrightarrow{Pd} 2H$$

$$Pd + xH \ \rightarrow PdHx$$
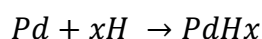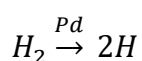
Two hydride phases of palladium are α and β which are distinguished with respect to their hydrogen content. In particular, α phase contains less hydrogen than β, thus α phase is only possible to be formed on surface while, β needs bulk palladium structure[67]. Due to unstable nature of β hydride phase, it is easily dissociated as temperature increase[66]:

$$\beta - PdH \ \rightarrow Pd + \ H_2$$
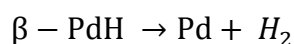
The entire process outlined above is tracked by many in literature via Temperature Programmed Reduction (TPR) analyses, in which the supported Pd sample is placed in an oven where the temperature is increased at a predetermined rate while sample is under hydrogen flow.

Although TPR is a prevailing analysis in supported Pd literature, Chou et al.[67], carried out a rather rare TPR study on not supported Pd but pure PdO powder synthesized by calcination of alkalized $Pd(NO_3)_2$ precipitates. As-prepared powder is reduced, exhibiting two distinct TPR peaks at 280K and 360K, corresponding to

hydrogen uptake and release, respectively. They attributed the first hydrogen uptake peak to the reduction of oxidized palladium and the following desorption peak to the dissociation of $\beta - PdH$. They also concluded that calcination temperature has an effect on PdO reduction temperature in which as the calcination temperature increased, reduction peak temperature is also increased due to penetration of oxygen to inner structure of palladium. However, even when the powder was calcined at a temperature as high as 773 K, PdO reduction was completed around 300K. Even though the behaviour of Pd might be slightly different when supported, Chou et al.'s work is important in sense that they point out that PdH formation requires a reduced bulk Pd and hydride dissociation TPR peak only follows the complete reduction of PdO peak.

In Table 2.1, some of the TPR studies on supported Pd are listed and classified with respect to parameters such as; catalyst pre-treatment processes, PdH decomposition peak temperature, additional observed peak temperatures and the assignment of these peaks. As seen in Table 2.1, the peaks other than PdH decomposition, can be categorized into two temperature ranges as 273-310K and above 400K and reviewed works attribute these hydrogen uptakes to the reduction of PdO[69–71] and reduction of TiO_2[72] or reduction of adsorbed oxygen[73], respectively. Notably, in all papers, PdH dissociation peak is reported in 300-400K range. Nonetheless, in supported Pd literature several publications report an additional hydrogen uptake peak in TPR profile which is consecutive to the PdH dissociation peak. Frequently this additional peak is attributed to bulk and dispersed PdO reduction overlooking the possibility of the hydrogen uptake for the reduction of the support. Consequently, they claim to form and decompose the hydride species prior to complete reduction of PdO. This work aims to present and analyse the TPR profile of supported Pd/TiO_2 catalysts through a quantitative analysis in order to differentiate PdO and surface TiO_2 related reduction processes at low and moderate temperatures.

Table 2.1 Reported TPR Peak Temperatures for Titania Supported Pd Catalysts

Pd wt %	Pd Precursor and Pretreatment Conditions	PdH Dissociation Temperature (K)	Additional Peak Temperature (K)	Interpretation Offered by the Authors	Ref.
2	Pd Acetate Calcined in O_2 873K	368	278	Reduction of PdO	(Ozkan, Kumthekar and Karakas 1998)
3	$PdCl_2$ Calcined in air at 773K	300-400	420	Reduction of TiO_2	(Shen et al. 2001)
1	$Pd(NO_3)_2$, Calcined at 673K	~340	273	PdO Reduction	(Zhang, Li and He 2014)
1	$PdCl_2$ Heated to 393K for 4 hour	331	493	Reduction of adsorbed oxygen	(Huang et al. 2013)
2	$Pd(NO_3)_2$, Calcined in air at 873K	323-333	<303	PdO Reduction	(Lin et al. 2004)

2.4 Dispersion & Particle Size Effect in Catalysis

The catalytic activity has proven to be affected by particle size of active species and a lot of efforts were dedicated to reveal the principles behind. It was explained by Che & Bennett in 1989[74] that dispersion is a key feature that affects the particle size since as the amount of metal sites available on surface is increased, they are prone to come together which leads to agglomeration and decrease of metal-support interaction. Later on, pioneer work of Haruta et al.[75,76] on CO oxidation on Au-titania catalyst was reported that as gold particle size increased TOF showed an increase up to 3nm from which decreased after further increase of particle size. In this work same effect was observed on Pd supported catalyst, also and it is to be discussed in subsequent sections.

In 2007 Al-Mazroai et al.[77] studied methanol reforming via irradiation on Pd/titania which showed the highest reforming rate at 0.5%Pd/titania and decreased upon increase of Pd content. The behaviour was explained by the agglomeration of Pd particles which forms a cover layer that prevent activation of necessary sites with irradiation. Similarly, Li et al.[78] showed photo-removal efficiency of propylene on Pd supported titania is increased as Pd loading increased from 0.2% to 1% and decreased upon further addition of Pd due to Pd acting as a recombination promoter at higher loadings. In addition to that, Wang et al. [79] developed a synthesis method by reducing the titania prior to Pd deposition to create better dispersed metal structure and reported that catalyst with higher dispersion showed improved catalytic activity for formaldehyde oxidation.

2.5   2D Materials

Clear and unambiguous definition of graphene by Novoselov&Geim in 2005 led to emergence of 2D material studies as a feracious topic in nanoscience[80]. In short notice, monolayer materials received a great deal of attraction by virtue of being on the common ground of many disciplines that study chemical, electronic, magnetic and optical properties of materials. In such materials the behaviours were found to be dissimilar to the ones observed with bulk structure due to changes in electronic properties and edge effects arise from decreased particle size and loss in symmetry or advanced light absorption capacity due to quantum size effect[81]. Motivated by all these advancements in single layer nanomaterials the efforts were dedicated to combine 2D structures with other class of materials which introduced hybrid nanostructures[82]. Metal oxides decorated with almost-single-layer metal films and metal particles stands out among these hybrid structures. The interaction of 2D metals on oxide surfaces may account for distinct enhancements in transition metal oxides, like titanium dioxide.

2.6   Hydrogen Spillover

Noble metal's ability to dissociate hydrogen molecules to its atoms and migration of dissociated atoms to support surface was first discussed by S. Khoobiar [83]. After that, there were many other reports focusing on this particular issue to clarify the principles of the phenomenon which later on developed into the birth of the name spillover[84–86]. By Connor and Falconer[87] spillover was explained as transportation of dissociated atoms by noble metals from metal surface to interface between metal and support. Later on, many papers were published on the subject to explain the effect of particle size of metal and interface area between metal and support on the spillover. Cies et al.[88] showed while the small particles (<3nm in size) are the main source of spillover; the large particles do not contribute to spillover at all. In 2013, Wu et al.[89] studied the Au-metal oxide interface in detail to realise interface activity is linearly proportional to the perimeter of the interface. This discovery gives a rise to many opportunities, since through the control of metal-support interface, spillover rate and any other reaction rate that take place through spillover can be optimised. Spillover was also suggested to take place in Pd/titania systems[90,91].

2.7   Reverse Oxygen Spillover

As put forward neatly by H. Lin[92] possibility of oxygen reverse spillover from support to noble metal was overlooked. Only recently, oxygen species from CeO_2 support were observed to migrate onto noble metal surface[93] and Pd/ceria system was proven to be working in accordance to this principle by Kaya et al. and Efstathiou et al.[94,95]. However, to the best of author's knowledge oxygen reverse spillover was not suggested in any earlier work in literature for Pd/TiO_2 system.

11

2.8   Fundamentals of Electron Spin Resonance Spectroscopy (ESR)

Electron Paramagnetic Resonance (EPR) or Electron Spin Resonance (ESR) Spectroscopy is a technique that is used to monitor paramagnetic centres in the samples. It has several applications such as catalysis research, surface science, biotechnology, pharmaceutical industry. The principles of ESR spectroscopy can be explained by quantum theory. Since paramagnetic centres experience Zeeman Splitting when placed in an external magnetic field, the ESR signal can be produced by the absorption of microwave irradiation at the resonant magnetic field value[96]. Quality of ESR signal intensity is determined by the factors: Maxwell-Boltzmann population distribution and spin-lattice relaxation[97].

$$\frac{N_{upper}}{N_{lower}} = e^{\left(\frac{-h\nu}{kT}\right)} \qquad \text{Equation 1}$$

Equation 1 shows the Maxwell-Boltzmann distribution while N_{upper} and N_{lower} represent the number of spins in upper and lower energy states formed by Zeeman Splitting, $h\nu$ represent the microwave energy, k is Boltzmann Factor and T is temperature. Maxwell-Boltzmann distribution is related to temperature, such that as temperature decrease population distribution between upper and lower energy increase[98]. Since ESR signal is produced by absorption of microwave while spins are excited to upper state from lower; a better signal is detected when the population excess in lower state was satisfied. This is the main reason that many ESR studies in literature was performed at cryogenic temperatures.

The second factor that effects ESR signal intensity is spin-lattice relaxation rate. The excited species in upper state dissipate its energy to the lattice through thermal motion of molecules while returning to lower energy state which is called relaxation[99]. The rate of spin-lattice relaxation is determined by T_1, where smaller T_1 means rapid relaxation. Maxwell-Boltzmann factor or i.e., microwave induced transitions, are in competition with relaxation as the former tries to decrease population difference while latter tries to increase that. Hence to get a high intensity

signal these two processes should be balanced[97]. In fact, the relationship between signal intensity, applied power and T_1 can be summarised by the equation below[97]:

$$I \propto \frac{\sqrt{P}}{(1 + \frac{P}{P_{1/2}})^{b/2}}$$

where; I is the ESR signal intensity,

P is applied power,

$P_{1/2}$ is the microwave power when $\frac{1}{(1+(\frac{g\,\mu_B}{h})^2 B_1^2 T_1 T_2)}$ is equal to ½,

b is the line shape factor of the respective signal.

If relaxation rate is not fast enough to work against microwave induced transitions, saturation phenomena occur at which signal becomes too broad to be detected[100]. The saturation phenomena can be used to deduce an indirect prediction about T_1 of samples. The experiment that makes the prediction possible is called saturation-recovery experiment at which microwave power is changed while keeping all the other parameters constant to find the power at which saturation phenomena starts[101]. This helps to predict T_1 roughly, relative in different conditions or samples: samples experiencing saturation at a lower microwave power supposed to have higher T_1 values.

Relaxation rate is associated with the fluctuations of external magnetic field induced by thermal motion of molecules[102]. Dependency of T_1 to the characteristic correlation time of fluctuations was summarised by Levitt (2008): for small molecules, like titania, T_1 decreases with decreasing correlation time, in other words slower molecular motion. Hence cryogenic temperature is also preferred to decrease molecular motion.

2.9   Catalytic CO Oxidation Reaction

CO oxidation is one of the prominent reactions to use when it comes to evaluate the performance of catalyst under investigation due to process' simplicity, availability and economical reasonability while being studied in more than 5000 papers since 1995[103]. By Meng et al. [104] the reaction mechanism on Pd/oxide support was explained as CO is chemisorbed on the surface of PdO while an oxygen atom is liberated on oxygen vacancies of support surface then a reaction between the two takes place. Later on, different oxide-based supports were examined by Xu et al.[105] for catalytic activity for CO oxidation reaction which revealed TiO_2 is the second most active support following CeO_2 in accordance with their oxygen storage capacity and reducibility. In 2017, Bratan et al.[106] showed on Pd/TiO_2 CO oxidation reaction starts around 60^oC then increases with temperature and reaches almost 100% conversion at 200^oC.   Chen et al.[107] studied Pd/TiO_2 for CO oxidation also to report that 100% conversion was reached at 90^0C with 1%(v/v) CO in dry air at a flow rate of 20 ml/min. Kolobov et al.[108] approached the problem about how the amount of Pd loaded on titania changes the catalytic activity to realise reaction rate increases with increasing Pd content both in dark and under UV illumination when samples with 0.05% to $2\%Pd/TiO_2$ was investigated. Same conclusion was arrived by Selishchev et al.[109] when Pd content range was increased to 0-4% Pd/TiO_2 while UV irradiated samples reported to show higher conversion. Wang et al.[110] studied the Pd size effect on CO conversion to conclude smaller sizes gives a higher reactivity and 2D Pd particles showed high CO conversion at room temperature which otherwise cannot be achieved.

14

CHAPTER 3

MATERIALS AND METHODS

3.1 Materials

Titanium dioxide powder used in this work is commercially available P25 (Degussa, 85% Anatase, 15% Rutile). Palladium precursor used in the synthesis of Pd/TiO$_2$ is Palladium(II)nitrate (Pd(NO$_3$)$_2$, 99.9%, Alfa Aesar (12-15wt% Pd)). Hydrogen gas used in TPR experiments is 10% H$_2$ in Ar (Linde) and helium gas is pure He (Linde). Hydrogen gas used in ESR and NMR experiments is pure H$_2$ (99%, Linde). Carbon monoxide gas used in CO oxidation reaction is CO (99%, Oksan) and oxygen source is air introduced to system by a compressor.

3.2 Synthesis Methods

Pd/TiO$_2$ was synthesised starting with TiO$_2$ powder and palladium(II)nitrate solution. Incipient wetness technique was used to incorporate Pd on titania. To synthesize around 4 g of catalyst, respective amount of (Pd(NO$_3$)$_2$ solution was mixed with 5mL of deionized water, then respective amount of TiO$_2$ powder was added to the solution. The mixture was left under ambient condition overnight to dry and placed in an oven at 120°C for 30 minutes. Dried paste was ground to powder later on. Pd loading on each sample was checked with inductively coupled plasma-optical emission spectrometry (ICP-OES). A sample calculation on how the amount of Pd loading on titania was calculated is given in Appendix A.

1:1 (wt Na/ wt Pd) Na promoted 1% (wt Pd/ wt titania) and 5% (wt Pd/ wt titania) Pd/TiO$_2$ samples were prepared starting from Pd/TiO$_2$ samples which were

explained earlier in this section and NaNO$_3$ salt (Merck, FCC crystal extra pure). To synthesize Na-Pd/TiO$_2$, 0.4 grams of Pd/TiO$_2$ samples was mixed with appropriate amount of NaNO$_3$ dissolved in distilled water. The mixture was dried at room temperature for a day which was then later dried at 120°C for 30 minutes in an oven.

3.3   Characterization Methods

Samples were characterised with X-ray diffraction (XRD) crystallography, Raman spectroscopy and high-resolution (HR) and high-contrast (HC) transmission electron microscopy (TEM) techniques.

3.3.1   X-ray Diffraction (XRD) Crystallography

Bare TiO$_2$ and 1%Pd/TiO$_2$ sample were subjected to powder X-Ray Diffraction Crystallography Analyses. The equipment used was Rigaku Miniflex X-Ray Diffractometer equipped with Cu X-ray source and scan was done with 1deg/min speed in the range of 10-80$^{\mathrm{o}}$.

3.3.2   Dispersive Raman Spectroscopy

Dispersive Raman Spectra of pure and 1%Pd/TiO$_2$ were collected with Bruker IFS 66/S FRA 106/S Hyperion 1000 Raman scope II, using 532 nm laser source.

3.3.3   Thermogravimetric Analysis

5%Pd/TiO$_2$ sample was subjected to Thermogravimetric Analysis on a Shimadzu DTG-60H equipment with parameters: Tmax=600$^{\mathrm{o}}$C, rate=10$^{\mathrm{o}}$C/min.

3.3.4 HR & HC-TEM Analysis

HR-TEM and HC-TEM images of all the prepared samples were obtained by Jeol JEM 2100F HRTEM (200kV) and by FEI Tecnai G2 Spirit BioTwin (20-120kV) equipment, respectively.

3.4 TPx Analysis

Temperature Programmed Reduction (TPR) analyses were performed on Micrometrics ChemiSorb 2750 equipment. The sample to be analysed was placed in a quartz U-tube shaped reactor between two layers of glass wool to prevent powder from being carried by the gas flow. Prior to measurement, sample was swept with He gas for around 20 minutes until the baseline of the thermal conductivity detector was stabilised. Then 10% H_2 in Ar gas was supplied with a volumetric flow rate of 25 sccm. Baseline of TCD Signal was stabilised again after 20 minutes, then oven heating was started with 5K/min ramp rate to a maximum temperature of 1000K. During the analysis TCD Signal and temperature inside the reactor was recorded at a function of time during heating and cooling.

For cryo-temperature TPR analyses, the reactor was placed in a Dewar filled with liquid nitrogen. When the temperature in the reactor decreased to 200K, hydrogen gas supplied and TCD signal started to be recorded. When nitrogen fully evaporates and room temperature was reached, same procedure with regular TPR analysis was conducted.

Temperature programmed oxidation (TPO) analysis was conducted for 5%Pd/TiO$_2$ sample. For the analysis sample was heated to a maximum temperature of 600°C with 10°C/min heating rate under 25 sccm O$_2$ (2% in He) flow. Cryo-temperature procedure was used same as the one described for cryo-temperature TPR analysis in the previous paragraph.

Photo desorption TPR analysis was performed for 1%Pd/titania samples. As the irradiation source a UVP Blak-Ray B-100AP High Intensity UV lamp at 365 nm wavelength was used. Photo desorption TPR analysis procedure explained in detail by Odabasi[111] was followed. In particular, the sample was placed inside the TPR reactor. The sample was illuminated with UV irradiation under He flow at ambient temperature. Irradiation treatment was conducted for two hours. At the end of irradiation H_2 gas was supplied to reactor and temperature ramp was performed with 5K/min rate and a maximum temperature of 1000K, same procedure as the regular TPR analysis was run.

3.5 Electron Spin Resonance (ESR) or Electron Paramagnetic Resonance (EPR) Analysis

For ESR Analyses a benchtop Bruker MicroESR connected to a manifold was used. MicroESR is a continuous wave (CW) ESR equipment working at X-band frequency. The manifold has the ability to supply 10^{-6} Torr of vacuum with the help of turbo molecular pump (VarianTurbo V70D) as well as supply H_2 gas at controllable pressures. Properties of manifold was explained in detail in a research paper of Uner group[112] and a representative schematic of the system is given in Figure 3.1.
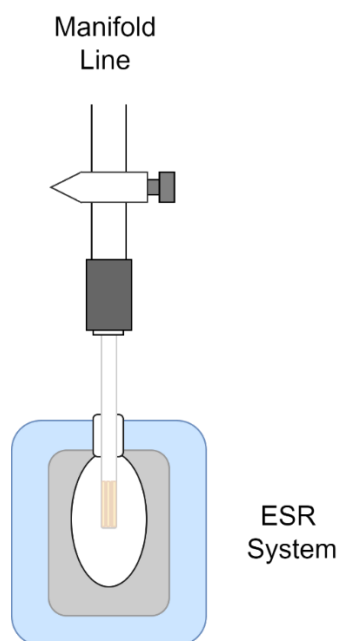
Figure 3.1. Manifold coupled ESR system

For 0.5% and 10%Pd/TiO$_2$ and pure TiO$_2$ ESR measurements, around 0.1 grams of sample was placed in the ESR tube connected to manifold. The tube was fully evacuated overnight. After the evacuation, 100 Torr (~0.13 bar) hydrogen was supplied at room temperature for half an hour. Then, the gas was evacuated again for ten minutes. The procedure was repeated for four times. Finally, mild pressure and temperature hydrogen treated sample was left evacuated overnight. Throughout the experiment ESR spectrum was recorded with 50 mW microwave power and 100 scans.

Saturation-recovery CW-ESR experiment at room temperature was conducted with a standard sample, Mn(II) impurity in plasticine. Spectra were recorded by changing microwave power between all the available values in the machine for air exposed sample at atmospheric pressure and sample at vacuum condition. Same procedure was repeated for 0.5%Pd/TiO$_2$ sample in vacuum.

3.6   Nuclear Magnetic Resonance (NMR) Analysis

^{1}H pulse NMR scans and spin-lattice and spin-spin relaxation measurements were conducted *in-operando* at room temperature on a Magritek Spinsolve NMR Spectrometer (43 MHz) connected to a manifold system same as the one described for ESR analysis. The experiments were conducted using 1% and 5%Pd/TiO$_2$. Around 300mg of sample was placed in the NMR tube and the atmosphere was controlled with the manifold system. Prior to measurement the system was evacuated overnight and treated with 100 Torr H$_2$ at room temperature for 10-minute intervals and evacuation in between for 4 times. Then, for pressure dependent experiments H$_2$ pressure changing from 20 Torr to 300 Torr supplied with 30 minutes time intervals. Spin-lattice relaxation time measurements were done by inversion recovery technique in which delay time was swept from 0.02 ms to 30 ms with a repetition time of 150 ms at 10 steps and spin-spin relaxation measurements were done by T$_2$ decay experiments with echo time determined as 405 us and repetition time as 100 ms with 7 steps. For time dependent experiments, samples were exposed to 100 or 300 Torr H$_2$ atmosphere while ^{1}H pulse, inversion-recovery and T$_2$ decay NMR experiments were done *in-operando*.

Synthesized Na-Pd/TiO$_2$ samples were also subjected to NMR analyses, for that samples were placed in the NMR tube connected to manifold and after the system is evacuated 100 Torr for 1%Na-Pd/TiO$_2$ and 300 Torr for 5%Pd/TiO$_2$ hydrogen pressures was supplied to meet the conditions of 1%Pd/TiO$_2$ and 5% Pd/TiO$_2$ NMR experiments. Then ^{1}H pulse NMR spectrum were recorded.

3.7   Solid UV-Visible Spectroscopy

Total reflectance spectroscopy of bare TiO$_2$ and 0.5%, 1%, 2% and 10%Pd/TiO$_2$ samples which were reduced at room temperature and low pressure H$_2$ atmosphere were obtained by solid state UV-Visible Spectroscopy. The samples were prepared by mixing around 0.08 grams of catalyst with 4 grams barium sulphate powder.

3.8 CO Oxidation Reaction Tests

CO oxidation reaction on Pd/TiO_2 catalyst was performed in a glass reactor (1 cm diameter) at which 0.1-0.5 gram of catalyst was placed. At a mixing chamber, air supplied by a pump and CO gas were mixed. CO gas flow rate was controlled by MKS mass flow controller calibrated as 200 sccm N_2 and MKS Type 247 4-channel readout. At the exit of mixing chamber gas flow was divided to two portions by a T-fitting with one end exhaust to atmosphere and at the second end flow rate was controlled by a valve. By the valve gas inlet to the reactor was changed between 20-490 ml/min. CO and CO_2 concentration at the reactor outlet was analysed by a CO & CO_2 detector equipped with CO sensor (maximum range 3% with 10ppm resolution, Gascard NG/Edinburg Instruments) and CO_2 sensor (maximum range 10% with 0.01% resolution, Gascard NG/Edinburg Instruments). A bypass line between control valve and gas analyser inlet was set. A hot plate heater was placed below glass reactor and UV lamp placed 5 cm above the reactor was used for irradiated reaction test. Inlet gas was allowed to enter first to the bypass system for 30 minutes and to reactor line before the heater set to temperature desired for thermal reaction tests. Thermocouple, placed next to the reactor on the hot plate, was reading the actual temperature values. For experiments in dark, reactor was covered with a box with reflective walls inside to satisfy dark reaction condition. Similarly, for irradiated tests, after 30-minute sweep of system by gas, UV lamp was turned on while CO and CO_2 concentration was recorded every second. Schematic drawing of the setup is given below:

21
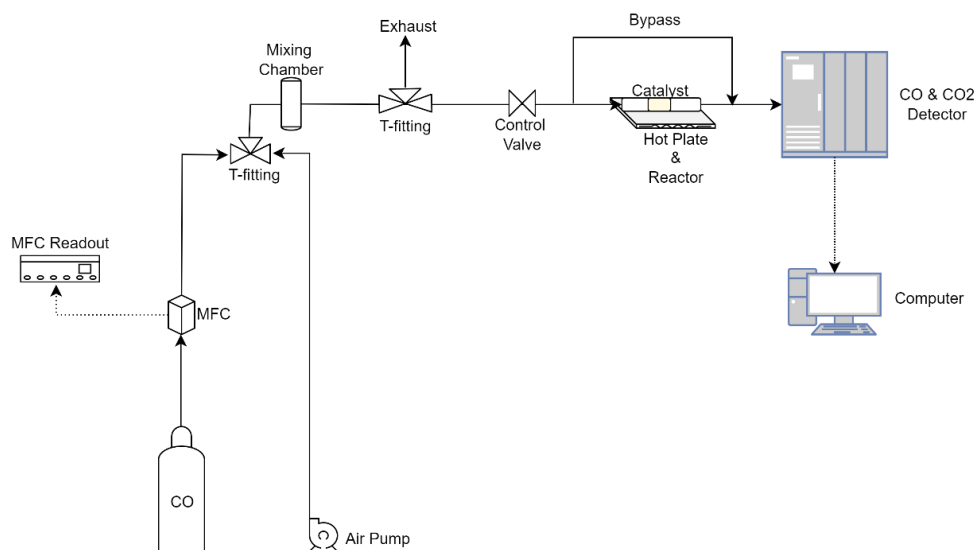
Figure 3.2. CO oxidation setup
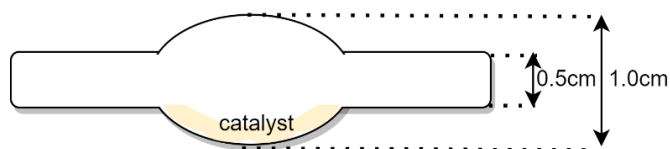
Figure 3.3. CO oxidation reactor drawing

Reactor was not fully filled with catalyst such that an empty place was left on the catalyst surface that allows mixing of gas phase and well mixed condition leads to CSTR approximation for this particular reactor.

In order to find optimum reaction conditions; first reaction was run at different reactor inlet flow rates (370 ml/min (CO concentration ~ 16000 ppm), 60 ml/min (CO concentration ~ 1100 ppm) and 20 ml/min (CO concentration ~ 1100 ppm)) on 0.1 gram 0.5%Pd/TiO$_2$ catalyst. Then to understand whether mass transfer limitations occur reaction was run at different catalyst amount at different reactor inlet flow rates: 0.2-0.3-0.5 grams 0.5%Pd/TiO$_2$ at 20 ml/min and 0.2-0.4 grams 0.5%Pd/TiO$_2$ at 180 ml/min (for all the listed reaction runs here a gas mixture with CO concentration ~ 1100 ppm was used).

To reveal any heat transfer limitations existing in the system temperature dependent dark experiments were run with 0.4 gram 0.5%Pd/TiO$_2$ catalyst at 180 ml/min flow rate of gas mixture with ~1100 ppm CO concentration, then cooling behaviour was also observed with the same flow conditions by natural cooling.

Temperature dependent reaction tests were run on 0.2 gram 0.5,2 and 10% Pd/TiO$_2$ catalyst at 20 ml/min and on 0.4 gram 0.52 and 10% Pd/TiO$_2$ at 180 ml/min reactor flow rates (CO concentration ~ 1100 ppm) while temperature was increased from room temperature to 100,200 and 300°C with 20-minute steps under dark or UV irradiated conditions.

Oscillatory kinetic behaviour was analysed with high CO concentration reaction gas mixtures on 0.1 gram 0.5%Pd/TiO$_2$ catalyst under dark conditions and at 200°C with different reactor inlet gas flow rates: 165, 370 and 490 ml/min with 17000, 16000 and 23000 ppm CO inlet concentrations, respectively.

CHAPTER 4

RESULTS

In this section, characterization, Temperature Programmed Reduction, Electron Spin Resonance, Nuclear Magnetic Resonance and CO oxidation reaction tests results are presented.

4.1   Characterization

4.1.1   XRD Results
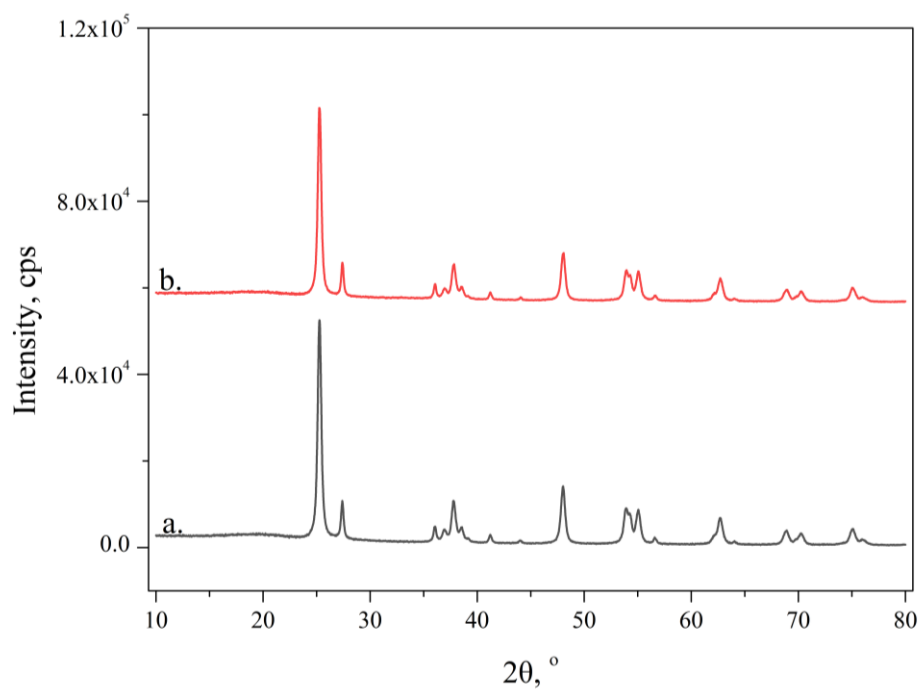
Figure 4.1. XRD patterns of a) TiO_2 and b) 1%Pd/TiO_2

X-ray Diffraction technique was used to analyze crystal structure of titania. As seen in Figure 4.1, XRD patterns of pure and 1%Pd/TiO$_2$ affirm the presence of both anatase (2θ =25.25^o) and rutile phase (2θ=27.39^o)[113–117]. The reason for not detecting Pd crystal phase is due to Pd amount being outside of detection limit of XRD.

4.1.2   Raman Results
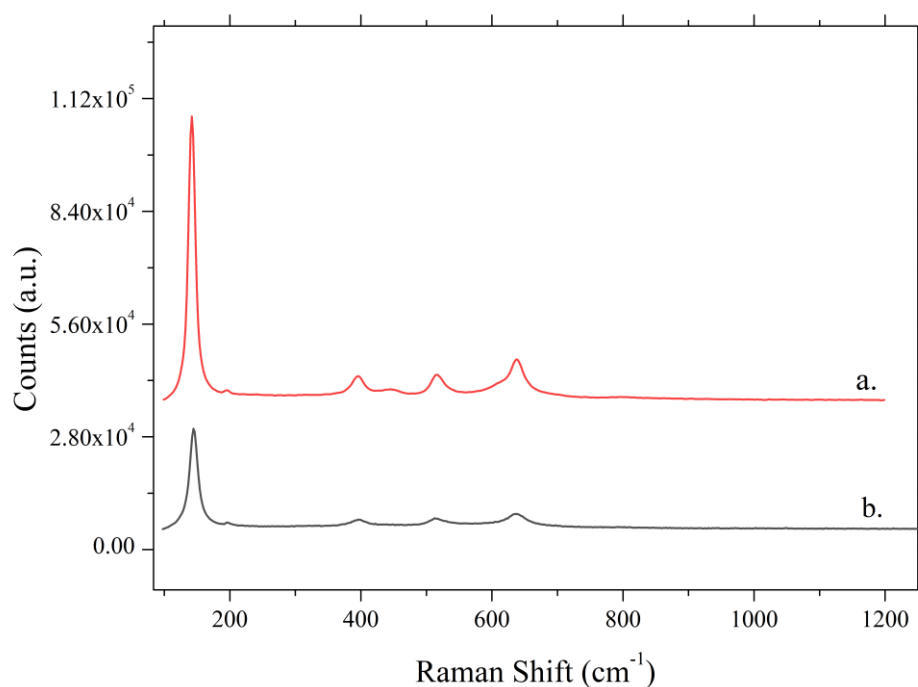
Figure 4.2. Raman shifts of a) TiO$_2$ and b) 1%Pd/TiO$_2$

As seen in Figure 4.2, both TiO$_2$ and 1%Pd/TiO$_2$ exhibit major peaks at 142, 198, 397, 515, 635 cm^{-1} which are known to correspond anatase phase and minor peaks at 441 and 610 cm^{-1} denotes rutile phase[117–121].

4.1.3 Thermogravimetric Analysis and Temperature Programmed Oxidation Results

Thermogravimetric analysis (TGA) and temperature programmed oxidation (TPO) analysis were conducted for 5%Pd/TiO$_2$. Derivative weight loss calculated from TGA profile and TPO results are compared in the figure given below:
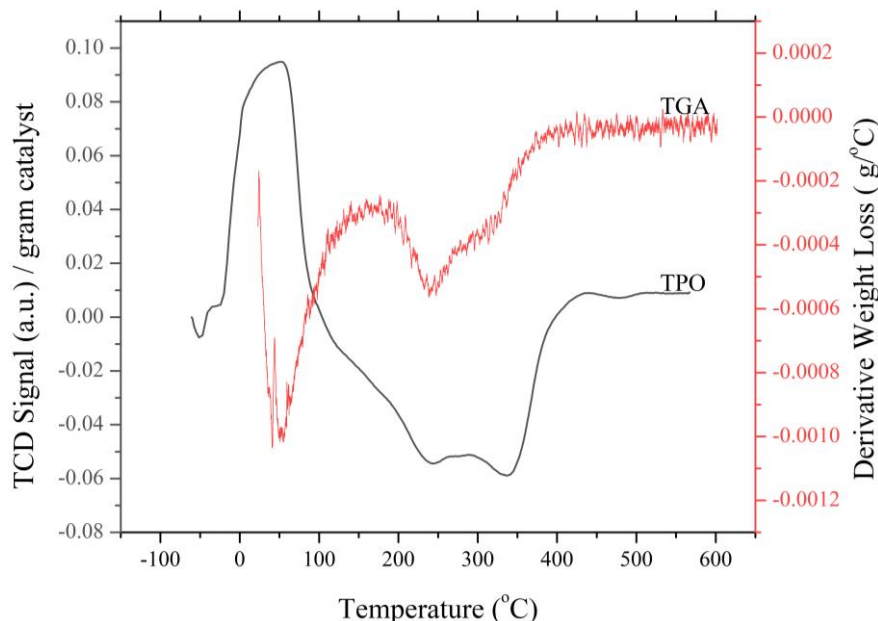
Figure 4.3. TGA and TPO profile of 5%Pd/TiO$_2$

In the TGA profile of 5%Pd/TiO$_2$ a three-step weight loss of around 5% was detected while in the TPO profile one oxygen uptake peak followed by an oxygen release peak was observed. The first weight loss event (corresponding to ~3%) detected by TGA is located at 50°C and attributed to nitrate decomposition. Bulk Pd(NO$_3$)$_2$ decomposition is expected to take place around 240°C in air[122]. However, supported thin layers of metal nitrates are shown to be decomposed at lower temperatures (50-150°C) than bulk ones, justifying results reported here[123]. The first oxygen uptake peak of TPO starts around -50°C and it is attributed to adsorption of oxygen at low temperature. The second weight loss (~1.5%) event takes place in two-steps which peak at 240°C and 315°C coincide with oxygen release peaks observed in TPO, attributed to oxygen release from the sample.

4.2   Titania

At the first portion of this work, reduction principles of pure titania surface was analysed with Temperature Programmed Reduction (TPR) analysis under hydrogen flow while paying attention to events taking place during heating and cooling cycles.

4.2.1   TPR Heating Analysis of Pure Titania

Around 50 mg of pure titania was subjected to TPR analysis while sample was heated to 1000K from room temperature with 5K/min heating rate:
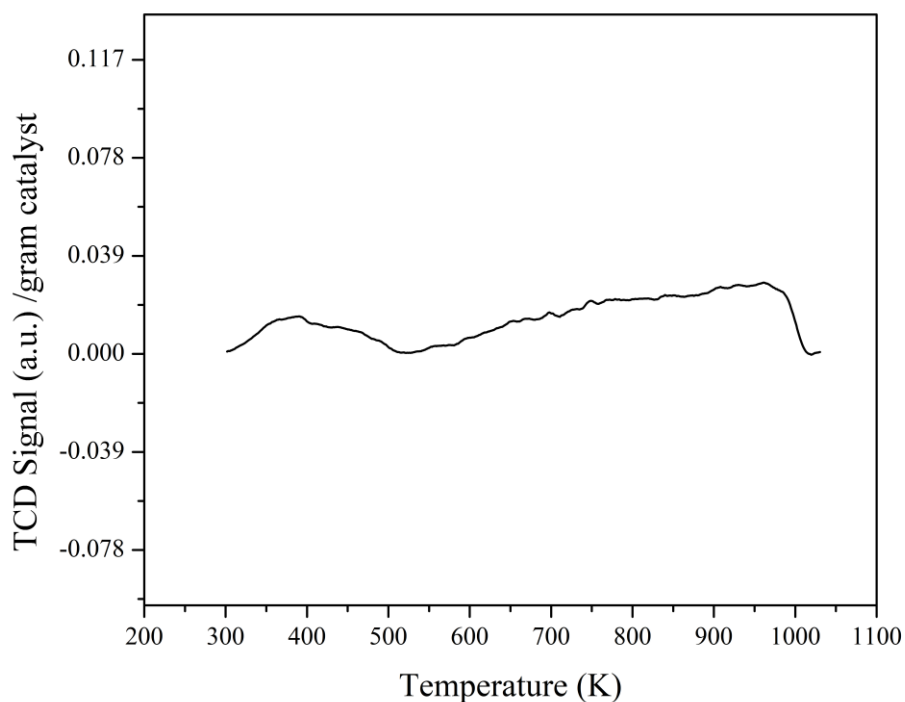
Figure 4.4. H_2-TPR profile of pure TiO_2

For pure titania two hydrogen uptake TPR peaks were observed at 390K and 970K while 1st one being very indistinct, 2nd one is higher in intensity and broadness. The 2nd peak is attributed to the surface reduction of TiO_2 by hydrogen and in fact, the

28

position and intensity is in accordance with literature results[124–126]. H_2 consumed for each TPR peak were quantified with respect to Ag_2O calibration. The details of quantitative analysis are given in Appendix F. By this analysis moles of hydrogen consumed per moles of sample was found as 0.0185 which corresponds to 0.93% of the sample was reduced.

4.2.2 TPR Cooling Analysis of Pure Titania
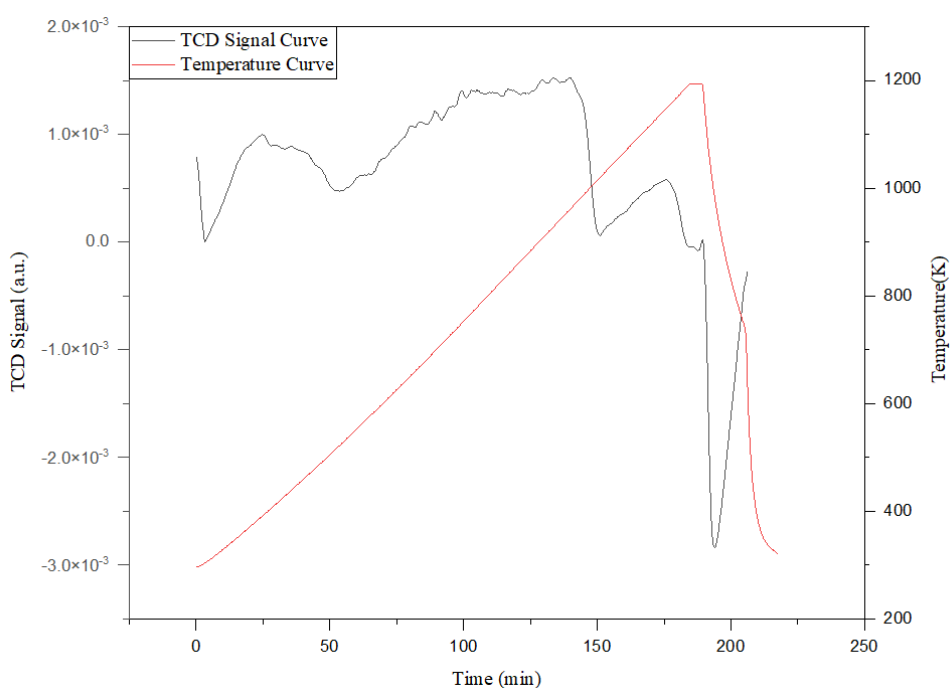
Figure 4.5. TPR cooling profile of titania

TPR profile obtained during heating and cooling cycles for pure TiO_2 is given in Figure 4.5. As seen, the analysis yielded a negative peak (hydrogen desorption) in the cooling part. The negative peak appeared during cooling was centred at 950K and quantitative analysis yielded a hydrogen desorption amount of 7.63×10^{-3} mol H_2/mol of titania. In order to reveal the origin of the negative peak and principles behind the phenomena, control experiments were done by changing the maximum temperature reached during the heating part of the TPR and results are given in Figure 4.6:

29
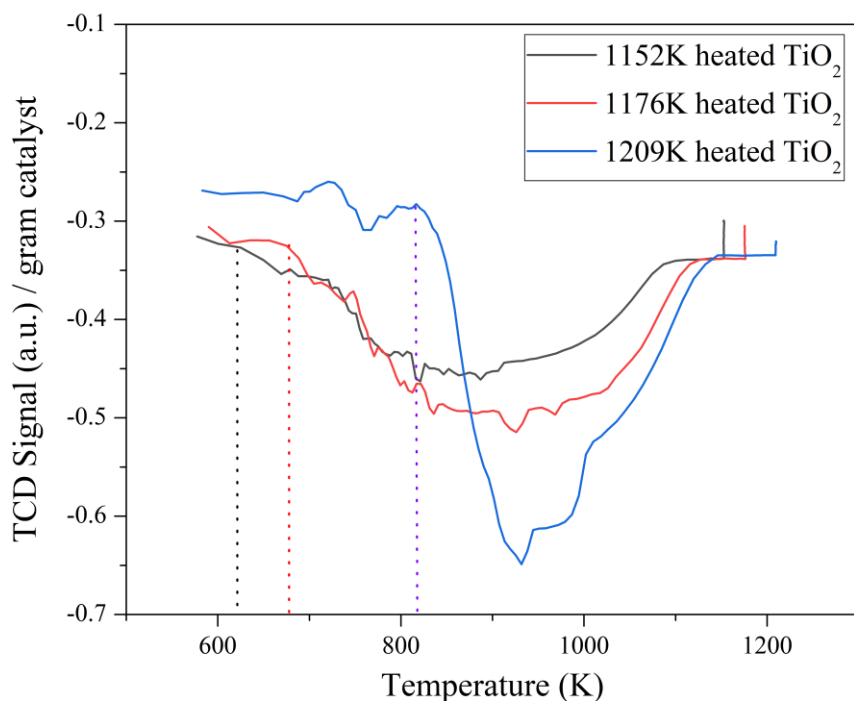
Figure 4.6. Tmax control experiment TPR profiles

As seen by the profiles in Figure 4.6, the area of the negative peak, consequently the amount of hydrogen desorbed was increased with the increasing Tmax during the TPR heating cycle. This indicates that the events taking place at the cooling cycle highly depended on the events at heating part. Additionally, no negative peaks were recorded after heating below 670K and addition of Pd on titania showed no appreciable effect on the hydrogen desorption peak.

30
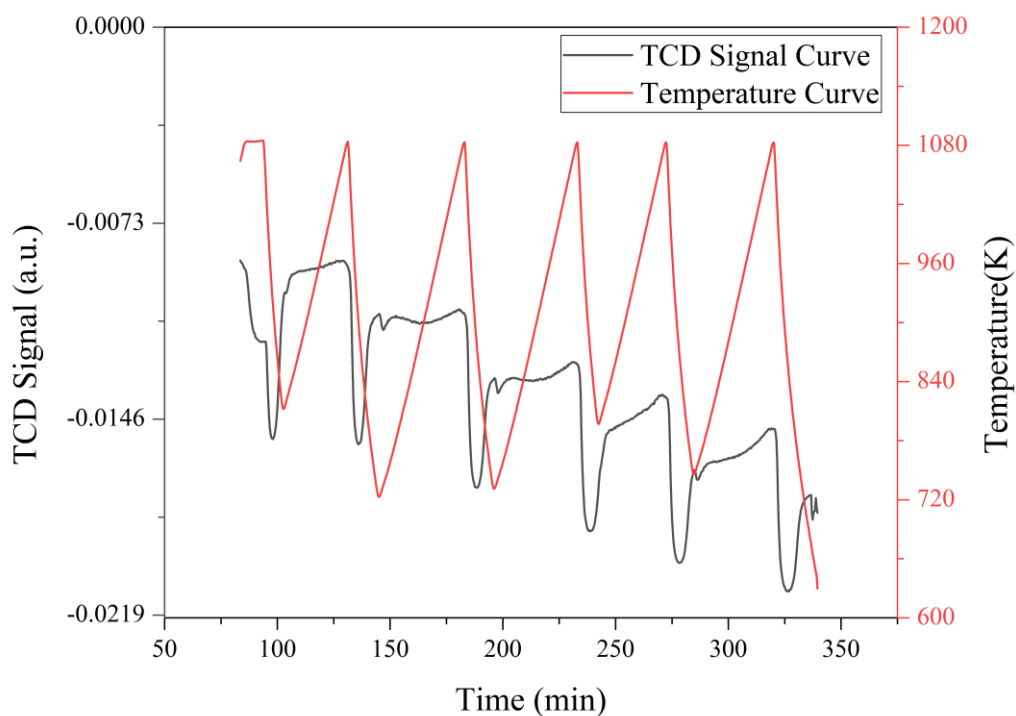
Figure 4.7. Reproducibility control for hydrogen desorption peak

Reproducibility of the negative peak in the cooling cycle was examined with repetitive heating and cooling TPR experiments in which the sample was firstly heated to 1100K and cooled back to 750K and heated again while the TCD signal was kept recorded. This procedure was repeated six times and the respective results are presented in Figure 4.7. This experiment proved that the process is reversible, hence can be reproduced many times almost identically.

In order to reveal the origin of the negative peak, possible phase changes of titania structure were examined with XRD analysis. Titania samples non treated and H_2-TPR treated until 450K and 1150K was subjected to XRD:
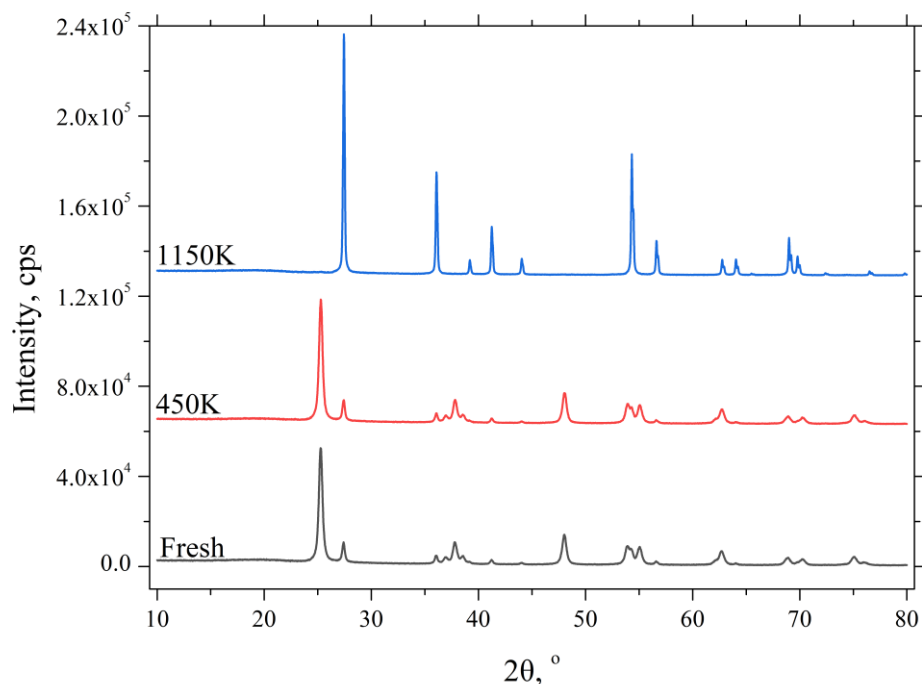
Figure 4.8. XRD analysis of H_2-TPR treated samples up to indicated temperatures

As seen in figure above, fresh sample and sample heated to 450K shows anatase dominant character with high intensity $2\theta = 25.25^o$ peaks while sample heated to 1150K shows rutile dominant character with $2\theta = 27.39^o$ peak being high in intensity. This indicates that a phase change from anatase to rutile occurs when sample is heated to 1150K. Hence it is suggested here that phase boundary between two possible phases coexisting on titania structure can be adsorbing and accommodating hydrogen during heating and releasing upon cooling.

To test this hypothesis, a thermodynamic analysis was carried out for the following suggested reaction of Magnéli phase formation:

$$n\,TiO_2 + H_2 \leftrightarrow Ti_xO_{2n-1} + H_2O$$
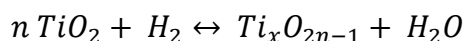
Since the phase change from anatase to rutile doesn't involve any H_2 related process, Magnéli phase formation that consumes hydrogen gas is used to analyse hydrogen desorption peak. The reason for not detecting any Magnéli phase with XRD analysis

may be due to these phases too low in concentration, thus out of detection range of XRD equipment.

For the analysis following thermodynamic properties of reactants and products used to find standard enthalpy and Gibbs free energy of reaction and equilibrium constant from which equilibrium conversion at a respective temperature can be found:

Table 4.1 Thermodynamic Properties of Reactant and Products

Species	ΔH_f^0 (kJ/mol)	ΔG_f^0 (kJ/mol)	Reference
H_2O	-241.8	-228.1	(Cox et. al, 1984)[127]
TiO_2 (anatase)	-944.7	-889.4	(Glasser,2009)[128]
$Ti_{11}O_{21}$	-9998.8	-9458.6	(Glasser,2009)[128]

In particular equilibrium conversion was found by the following analysis:

$$\Delta H_{reaction}^0 = \sum \Delta H_{f,products}^0 - \Delta H_{f,reactants}^0$$

By assuming heat capacity independent of temperature:

$$\Delta H_{reaction}^0 = \Delta H_{reaction}^0(298K)$$

$$\Delta G_{reaction}^0 = \sum \Delta G_{f,products}^0 - \Delta G_{f,reactants}^0$$

$$K_{eq}(298K) = \exp\left(\frac{-\Delta G_{reaction}^0}{R*298K}\right)$$

By Van't Hoff Equation:

$$\ln\left(\frac{K(T)}{K(298K)}\right) = \frac{-\Delta H_{reaction}^0(T)}{R}\left(\frac{1}{T} - \frac{1}{298K}\right)$$

Rearranging:

$$K(T) = K(298K)\exp\left(\frac{-\Delta H_{reaction}^0(T)}{R}\left(\frac{1}{T} - \frac{1}{298K}\right)\right)$$

Reaction is 1st order in both directions for $H_2(g)$ and $H_2O(g)$ and TiO_2 and Ti_xO_{2n-1} species are solid phases:

$$K_{eq} = \frac{C_{p,eq}}{C_{r,eq}} = \frac{C_{a,0} * Xae}{C_{a,0} * (1 - Xae)}$$

$$Xae = \frac{K(T)}{1 + K(T)}$$

For TCD signal analysis, cumulative increase in signal intensity of negative peak at a given time was normalized to cumulative signal intensity of entire negative peak. Results of the thermodynamic analysis and that of TPR analysis was compared at Figure 4.9:
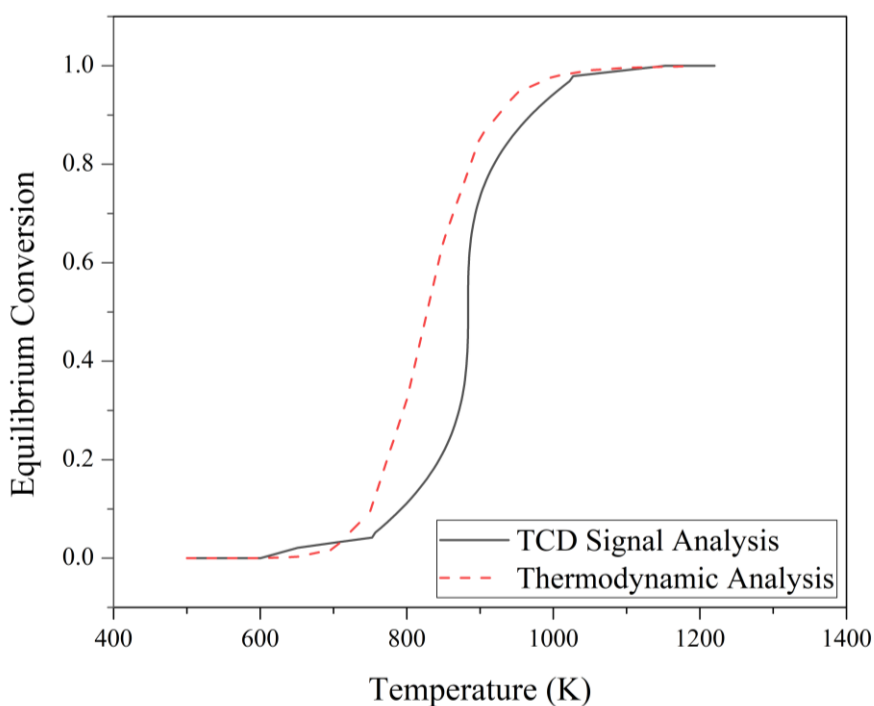
Figure 4.9. Thermodynamic vs TCD signal analyses compared

The equilibrium conversion vs temperature profile that was calculated by thermodynamic analysis of $Ti_{11}O_{23}$ formation from TiO_2 and the profile that was revealed by hydrogen desorption peak of TPR was found to be in accordance. No other Magnéli phase yielded such close results to TCD signal analysis. Hence, here

34

we claim that Magnéli phase was formed during temperature programmed reduction of anatase during heating to 1100K under hydrogen flow. Hydrogen accepts oxygen species from titania lattice of which later desorbed in hydrogen gas form during consequent temperature decrease. Previously, Mao et al. [129] showed the boundary between anatase and rutile acts as a H-binding site during transition from one to another, similar to the results reported here. In order to test if in fact the phase boundary formed during transformation from anatase to rutile is the source of the negative peak observed here, phase change data is used. Phase fraction data reported by Low et al.[130] is given for anatase to rutile transformation in air atmosphere as a function of temperature which was deduced by XRD analysis. The data presented in Low et al.'s work was reproduced and compared to TCD analysis results of this work:
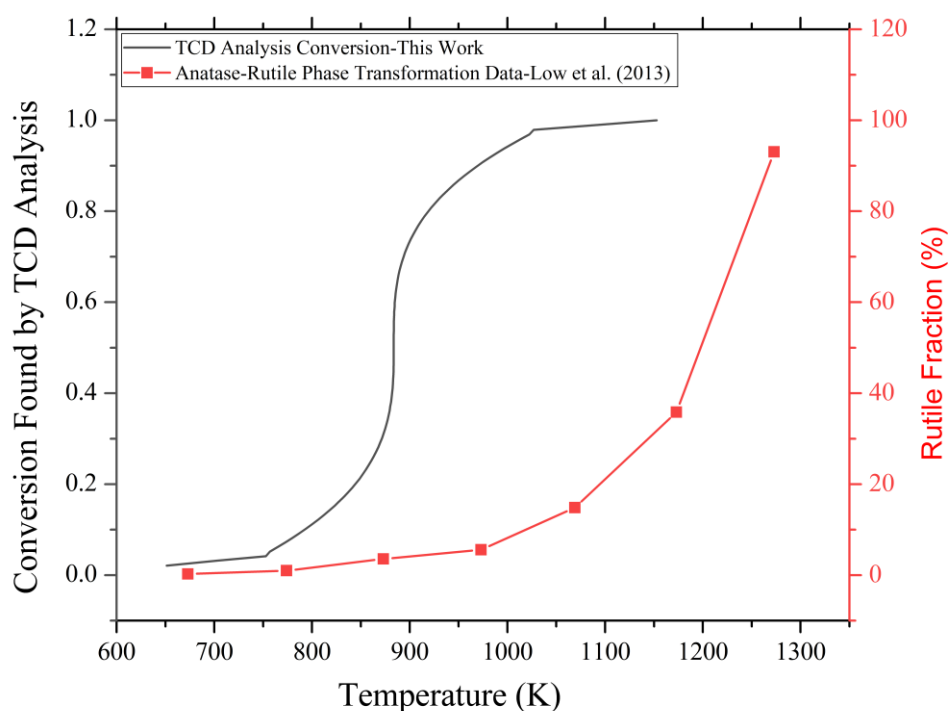
Figure 4.10. TCD analysis results compared to literature reports for anatase to rutile transformation

As seen in figure above, the behaviour followed by hydrogen desorption during cooling cycle of H_2-TPR analysis in our study is not in full agreement with anatase-rutile phase change behaviour reported by Low et al. However, accurate temperature measurements during these phase transitions are not trivial and results should be interpreted with caution. Hence, it is tentatively concluded that phase boundary formed between anatase and rutile phases is not the source of H adsorption and desorption behaviour observed by TPR analysis. On the contrary, behaviour shown in Figure 4.9 is in a better agreement, such that Magnéli phase and anatase or rutile boundary was found to be able to accommodate hydrogen during heating under H_2 flow and releasing when temperature is decreased.

4.3   Pd/Titania

For the second part of this work effect of Pd addition on titania surface and changes in structure and reducibility was investigated with TEM, TPR, ESR and NMR studies.

4.3.1 TPR Analysis of Pd/TiO$_2$
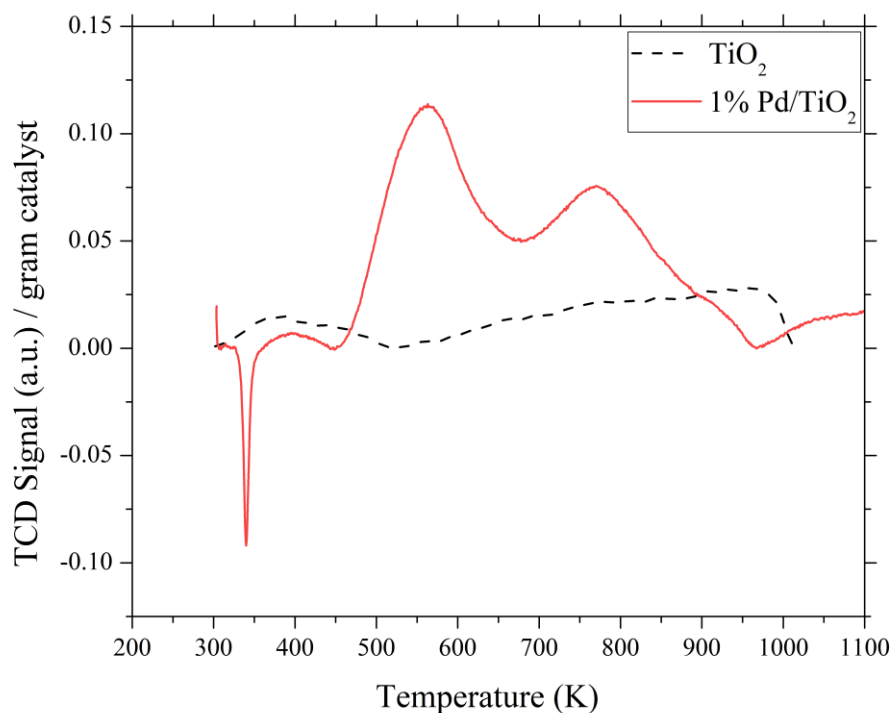
Figure 4.11. TPR profiles of TiO$_2$ and 1%Pd/TiO$_2$

TPR profiles of pure titania and 1%Pd/TiO$_2$ was recorded with 5K/min temperature ramp with a maximum temperature of 1100K under hydrogen flow and comparison of profiles is given in Figure 4.11. As shown, after incorporation of Pd on titania surface its reducibility is increased significantly. For pure titania two hydrogen uptake peaks were observed at 390K and 970K while for Pd supported titania there are 3 major peaks detected: one hydrogen desorption peak at 340K and two uptake peaks at 600K and 800K. The additional negative peak observed at 340K for 1%Pd/TiO$_2$ corresponds to decomposition of hydride palladium phase while other two peaks correspond to TiO$_2$ reduction at 600K and 800K. Shift in reduction temperature to lower values, in this case from 970K to 600K and 800K, for 1%Pd/TiO$_2$ is an accepted effect of Pd on TiO$_2$[131,132].

H_2 consumed for each sample were quantified with respect to Ag_2O calibration. As summarised in Table 4.2, amount of Ti reduced was increased more than 4 times after introduction of Pd onto the sample. Pd incorporation cause some of the reduction take place more readily than pure TiO_2 due to the ability of Pd to dissociate hydrogen gas into its atoms. Thus, the reduction peak observed at TPR profile of TiO_2 is shifted to lower temperatures, in addition to that a higher number of surface species was reduced via using Pd acting as a reduction promoter.

Table 4.2 Quantitative Analysis for Pure and 1%Pd/TiO_2 TPR Peaks

Sample	Hydrogen (mol) consumed / titania (mol)	Reduced amount (%)
TiO_2	0.0185	0.93%
1%Pd/TiO_2	0.0914	4.57%

The use of noble metals as reduction promoters were previously reported in literature[133–135]. Pd was also shown to be an effective reduction promoter for Co: in particular Jacobs et al.[136] has proven that reduction temperature of Co-oxide decreases with use of Pd as a reduction promoter while Romero et al.[137] also concluded same results for Pd thin layer deposited on Co surface of which are able to decrease the reduction temperature as low as ambient. The behaviour at room temperature was analysed by cryogenic temperature H_2-TPR in this work:
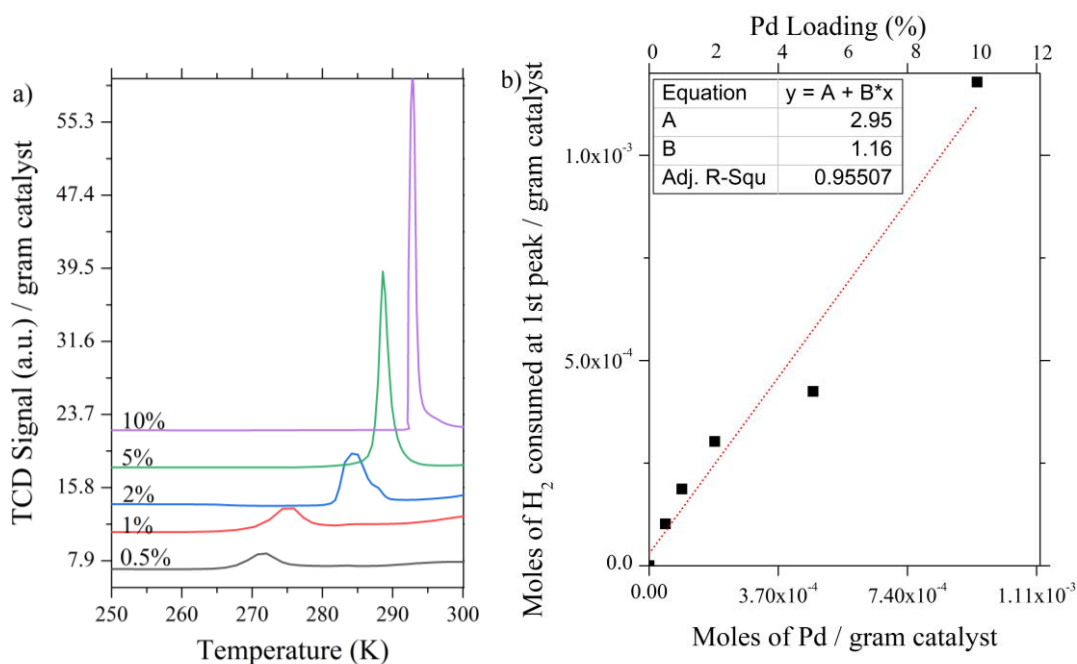
Figure 4.12. a) TPR profiles of x%Pd/TiO$_2$ between 250-300K b) H$_2$ consumed in PdO TPR peak / gram catalyst vs moles of Pd / gram catalyst graph

Cryo-temperature TPR experiments were performed by cooling Pd/TiO$_2$ samples in the TPR tube to a temperature as low as 200K which were then heated up to 1000K under hydrogen flow while temperature inside reactor and TCD signal were kept recorded. This way, before room temperature was reached each sample reduced showing two TPR peaks: one around 290K and the second one around 300K (Figure 4.12.a). Peaks in TPR profiles were fitted and quantitative analysis of each was carried out according to Ag$_2$O calibration explained in detail in Appendix F. For example, quantitative analysis for 1% Pd/TiO$_2$ revealed at the 1st sharp peak (280K) a H$_2$ uptake of 5.58×10^{-6} moles was taken place (Table F.1). Additionally, at hydride decomposition peak (Figure 4.13.a) 4.79×10^{-7} moles H$_2$ was released which means that this much of H$_2$ was used previously to form PdH$_{0.19}$ phase. On the other hand, Pd amount that 1%Pd/TiO$_2$ TPR sample contains is 5.14×10^{-6} moles. This number means that it takes 5.14×10^{-6} moles of H$_2$ to reduce all the PdO species present in the sample. As can be seen, the amount of H$_2$ needed to reduce all PdO species and form the hydride phase predicted by decomposition peak is present in the TPR peak at

39

280K. Consequently, it can be concluded that peaks around 290K can be assigned as PdO reduction peak. The same analysis procedure was applied for all Pd/TiO$_2$ samples and H$_2$ amount consumed at PdO reduction peak in moles per gram catalyst was plotted as a function of moles of Pd per catalyst gram. The plot is seen Figure 4.12.b, where it shows a linear behaviour with respect to Pd loading with a slope of 1.16. The slope indicates that there is a 1/1 ratio between H$_2$ used and PdO present in the sample which supports the PdO reduction process assignment to the peak. The slope being slightly higher than 1 indicates both PdO reduction and hydride formation takes place at this temperature.
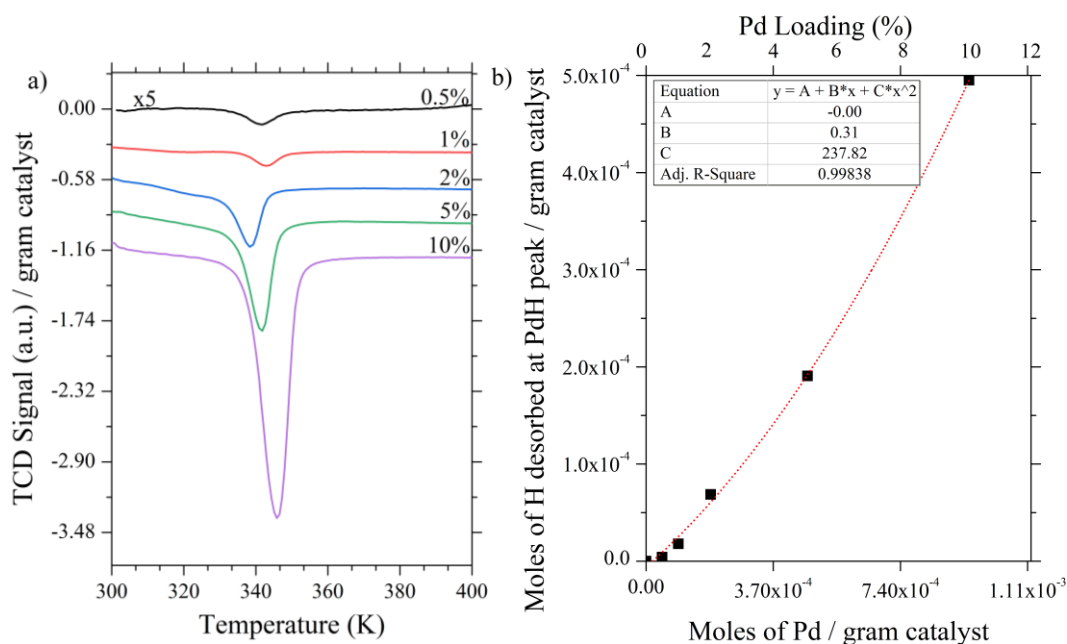
Figure 4.13. a) TPR profiles of x%Pd/TiO$_2$ in the range of 300-400K b) H desorbed on PdH TPR peak / gram catalyst vs moles Pd / gram catalyst

TPR profiles of Pd/TiO$_2$ samples around 340K are given in Figure 4.13 showing PdH decomposition peaks. Quantitative analysis of these peaks showed that moles of H desorbed at PdH decomposition peak shows a quadratic behavior with the moles of Pd present in the sample per gram catalyst. By quantitative analysis of each decomposition peak (explained in detail in Appendix F), H/Pd ratio for each sample was calculated and given in Table 4.3. Since the calculated values corresponds to

40

bulk $\beta - Pd$ phase, the amount of Pd which can form $\beta - PdH$ was calculated by the following analysis:

$$Pd \text{ amount that can give rise to } \beta PdH(\%)$$
$$= \frac{H}{Pd} \text{ for PdH peak} * \frac{1 \text{ mol } Pd}{0.53 \text{ mol } H} (\text{for } \beta PdH) * 100$$

$$Rest \text{ of } Pd (\%) = 100 - Pd \text{ amount that can give rise to } \beta PdH(\%)$$

The percentages of amount Pd that can give rise to $\beta - PdH$ and rest of Pd particles for each sample is given in Table 4.3.

Table 4.3 Pd That Can Give Rise to $\beta - PdH$ and Rest of Pd Amount (%) Calculation Results

Pd loading (%)	H/Pd for PdH peak	Pd amount that can give rise to βPdH (%)	Rest of Pd (%)
0.5	0.09	17	83
1	0.19	36	64
2	0.37	69	31
5	0.41	77	23
10	0.53	99	1

$\beta - PdH$ phase is associated with bulk Pd structure which is in 3D from. Consequently, a co-existence of 2D and 3D Pd structures at low Pd loaded samples is revealed while low Pd loaded samples have 2D dominant character and high loaded ones have 3D dominant. In order to validate phase related evidence revealed by quantitative analysis of PdH TPR peak, HR-TEM and HC-TEM images were examined in detail:
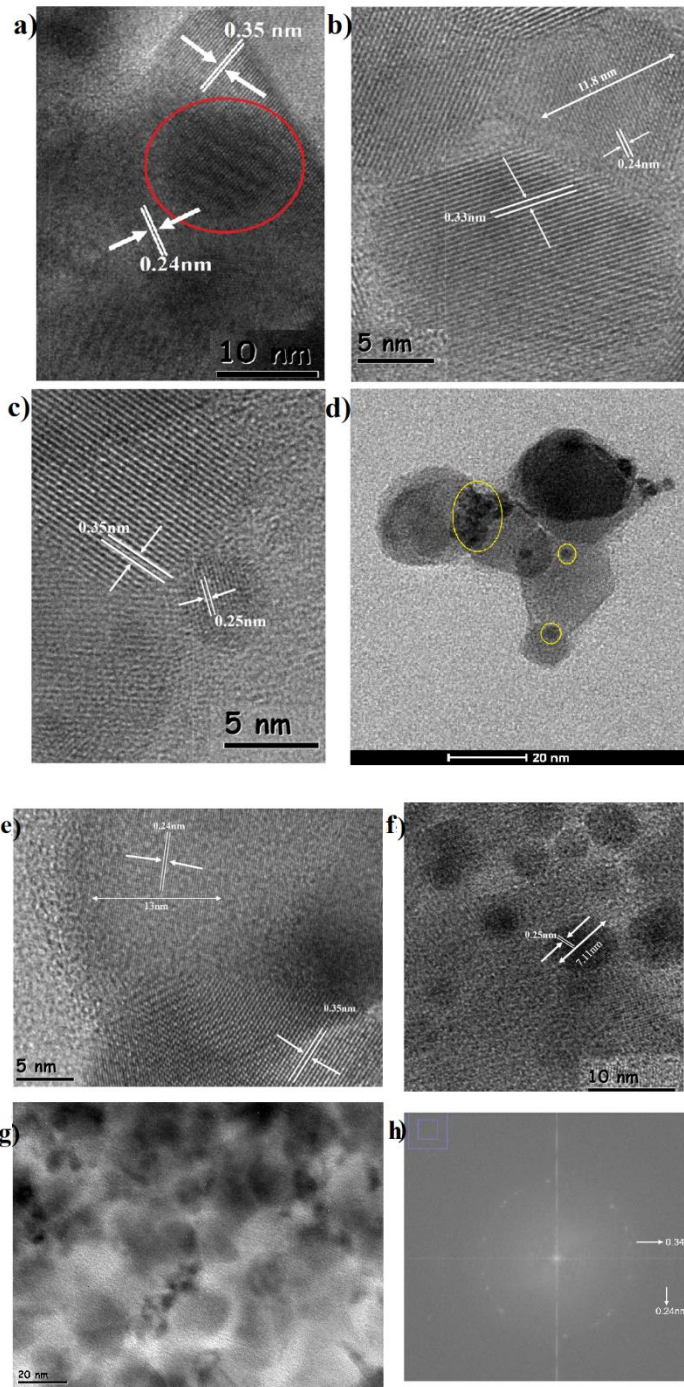
Figure 4.14. HR and HC TEM images for fresh a) 0.5% b) 0.5% c) 1% d) 10%; e) 0.5% f) 2% g) 5% after hydrogen exposure at RT h) FFT of figure g; Red circle indicates Moiré fringe and yellow ones Pd metals

HRTEM images of fresh 0.5, 1%Pd/TiO$_2$ and HCTEM images of 10%Pd/TiO$_2$ are given in Figure 4.14a-d and HRTEM images of room temperature and low pressure (around 100 Torrs) H$_2$ exposed 0.5, 2 and 5% Pd/TiO$_2$ and FFT of HRTEM image of 5% is given in Figure 4.14.e-h. HRTEM images of both fresh and hydrogen exposed, low Pd loaded samples show characteristic lattice fringes of Pd at 0.25nm and that of titania at 0.35nm[138–142]. Pd particles showed the highest Pd dispersion at 2%Pd/TiO$_2$. At loadings below 2%, Moiré patterns are detected and indicated in red circle, that proves the close interaction between metal and support. Since in close proximity of Moiré patterns characteristic lattice fringes of Pd and titania detected, this indicates Moiré fringes were formed from interaction of these two species. For 0.5% and 1% samples Pd particle size detected to be reached a value around 15 nm. Particle sizes that are unexpectedly large for Pd correspond to formation of atomically thin 2-dimensional layers of metal[143,144]. These large metal particles found as patch-like structures on support surface. For 1% sample, in addition to 2D particles, 3D particles were also observed to co-exist (evidenced by particle with contrast in Figure 4.14.c) Although, metal is observed to be well-dispersed at low loadings, agglomeration of Pd starts with further increase of loading. As seen in Figure 4.14.a and g, at 5 and 10% Pd loading, the particles are squeezed into smaller regions and it was not possible to observe lattice fringes while Moiré patterns were also lost. For 5% and 10% individual Pd metals are hard to be distinguished but existence is proved by FFT image (Figure 4.14.h).
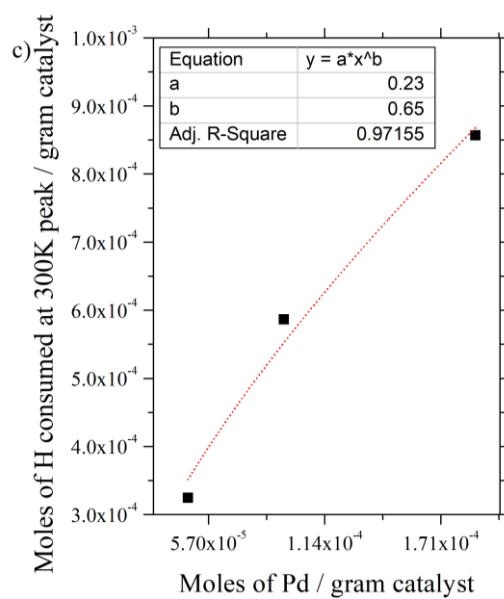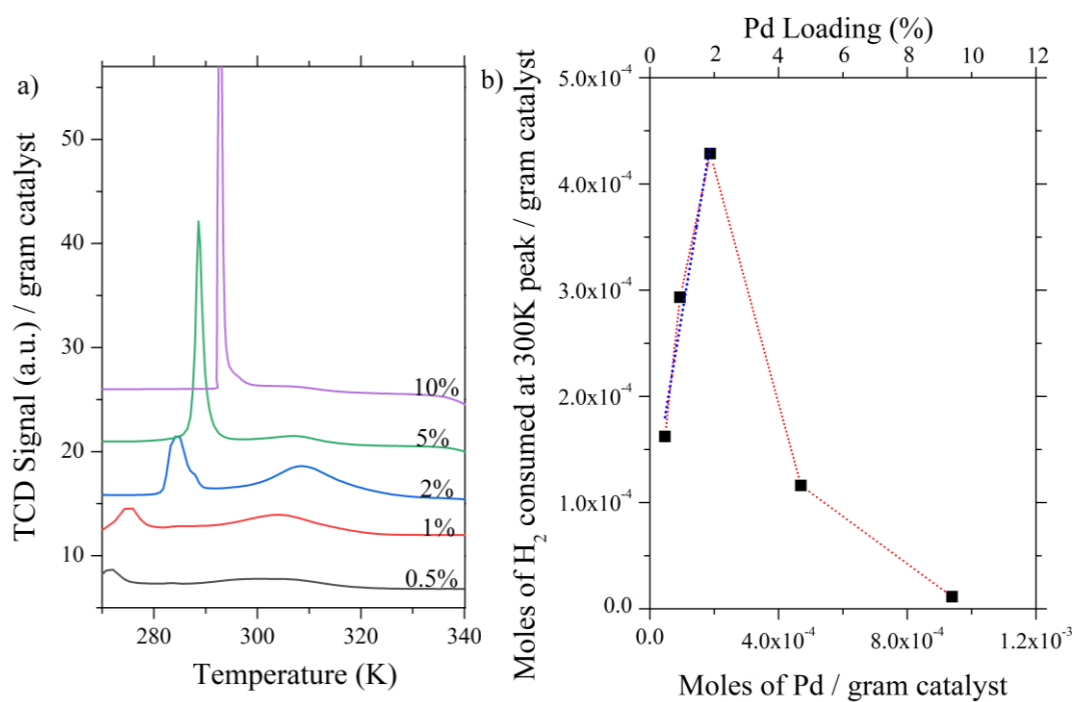
Figure 4.15. a) TPR profiles of x%Pd/TiO$_2$ between 270-340K b) H$_2$ consumed on 300K TPR peak / gram catalyst vs mol Pd/ gram catalyst graph c) H consumed on 300K TPR peak / gram catalyst vs mol Pd/ gram catalyst curve fitting for 0.5-2% Pd/TiO$_2$

Since reduction of PdO species and decomposition of hydride phase completed at 290K and 340K peaks, the rest of the TPR peaks were assigned to reduction of the titania support. In Figure 4.15.a given the TPR profiles of samples in the range of 270-340K. In this range a peak was detected around 300K. When the quantitative analysis of this peak per Pd amount in samples was conducted, it showed not a linear relation to Pd loading, as Pd loading increased, moles of H_2 consumed at 300K peak is increased between 0.5-2% which is then decreased with further increase in Pd loading (Figure 4.15.b). Hence, it was assigned to support surface reduction by the H_2 dissociated by noble metal through spillover process. Additionally, TiO_2 (P25) has a BET surface area of 50 m^2/g and it was previously shown that on an oxide surface can accommodate 10^{15} sites/cm^2[145]. When the proper calculation was carried out, it was estimated that surface oxygen species account for 6.63% of the entire species available in TiO_2. On the other hand, quantitative analysis revealed, the reduction of 6.67% TiO_2 to Ti_2O_3 species was completed at 2nd and 3rd TPR peaks at 300K and 595K for 1%Pd/TiO_2 (Figure 4.16.a). Consequently, approximately 70% of the titania surface was reduced at room temperature, while the rest of the surface reduction was completed at 595K. The behavior in Figure 4.15.b indicates that surface reduction of support through the promotion of Pd is highly depend on the Pd loading. As disclosed by TEM images, 2% shows the highest dispersion and patches of atomically thin Pd particles are only detected for loadings lower than 2%. Hence, the thin nature of the Pd on the surface account for accelerated reduction of support. As Pd loading increased up to 2% dispersion of metal is increased while sustaining 2D nature and reaching an optimized value at 2% where interaction of

support and metal is highest, however upon further Pd addition thin nature is lost such that surface reduction of titania is lowered giving the profile indicated by Figure 4.15.b.

Similar to the results presented here, change in 2D-3D character of metals due to agglomeration when loading is increased has been known for Pd and showed by Liu et al.[146] and the references presented in their paper. Similarly, Roca and Kamiya[147] were recently detected phase change from 2D to 3D taking place with AFM technique when the amount of InAs was increased from 0.6ML to 0.8 ML on GaAs support. Correspondingly, in this work, Pd phase was found to be changed from 2D to 3D by quantitative TPR analyses when Pd amount increased gradually. Figure 4.15.b when moles H_2 consumed vs moles of Pd curve of low loaded samples (0.5, 1 and 2%), i.e. 2D samples, fitted to a straight line shown in blue in the respective figure, a slope of 1.4 is yielded. This slope is equal to H_2 consumed per Pd ratio. Since one H_2 can capture one O atom from titania surface during reduction, it can be concluded that moles of titania reduced per moles of Pd is equal to 1.4. Consequently, it can be concluded that 2D Pd metals can reduce titania surface that is almost equal to their amount. On the other hand, in Figure 4.15.c same 2D samples' moles of H consumed for room temperature surface reduction of titania vs moles of Pd curve is fitted to a function with equation $y=a*x^b$. The parameter b was estimated as 0.65 with this analysis which is almost equal to 2/3. Hence the following analysis can be carried out:

$$300K \; TPR \; peak \; hydrogen \; consumpiton \; in \; moles \; = a * (moles \; of \; Pd)^{\frac{2}{3}}$$

Assuming moles of Pd is linearly correlated with volume of Pd particles and surface reduction at 300K takes place through hydrogen spillover mechanism:

$$moles \; of \; H \; diffused \; to \; titania \; sites \; at \; room \; temperature$$
$$= a * (volume \; of \; Pd)^{\frac{2}{3}} = a * \left(\frac{4}{3}.\pi.r_{Pd}^3\right)^{\frac{2}{3}} = a' * r_{Pd}^2$$

This equality indicates that spillover hydrogen amount is related to radius of Pd metals on titania surface by the square of it which corresponds to Pd surface area since metal is shown to be 2D for low loaded samples. Then it can be concluded that Pd exchanges H and O atoms with titania surface all through it surface area for 0.5-2%Pd/Titania. On the other hand, for 5-10% behaviour changes and no meaningful explanation can be deduced for 3D particles except they transport H atoms to titania surface with an area smaller than their surface area. This indicates that, the interface between metal and support is decreased for 3D particles as well as their interaction and atomic transfer capability.
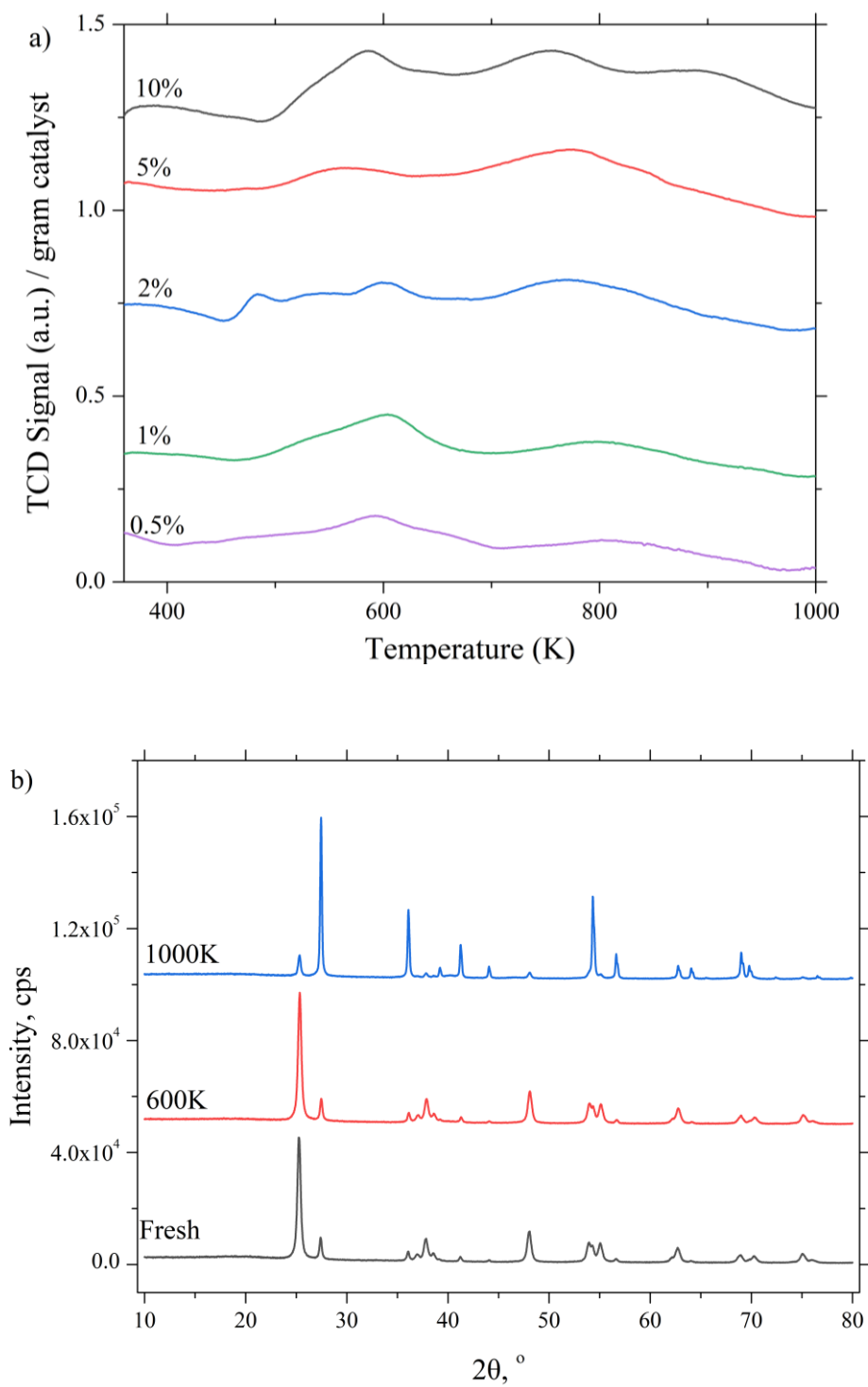
Figure 4.16. a) TPR profiles of x%Pd/TiO$_2$ between 400-1000K b) XRD results for hydrogen treated 1%Pd/TiO$_2$ at different temperature

The rest of the TPR profiles are given in Figure 4.16.a in the range of 400-1000K. These peaks showed no particular change with respect to Pd amount. X-ray Diffraction technique was used analyse changes in crystal structure of titania introduced during TPR experiments. To understand the structural changes induced during formation of each TPR peak, samples which were reduced at different thermal conditions were analysed by XRD given in Figure 4.16.b. Fresh 1%Pd/TiO$_2$ sample, as well as samples which were hydrogenated while being heated to 600K and 1000K were used to analyse the TPR peak in the range of 500-600K and the peak above 600K, respectively. XRD patterns of fresh and upto-600K-heated samples affirm the presence of both anatase (2θ =25.25°) and rutile phase (2θ=27.39°) [113,115,116,141]. Although there is a small change in respective intensities of these two peaks, no significant phase change takes place between these two temperatures. On the other hand, upon thermal hydrogen reduction up to 1000K, characteristic rutile peak becomes sharper while anatase peak is no further detected. This indicate that heating to 1000K lead to phase transformation from anatase to rutile. In addition to anatase to rutile transformation, face-centred cubic phase of Pd formed on 1000K sample evident by XRD peaks at 2θ=40.25° and 2θ=46.70° [141,148–150]. Hence TPR peaks in the 500-600K range belong to surface reduction of titania without a significant phase change while the ones above 600K are accompanied by a phase change.
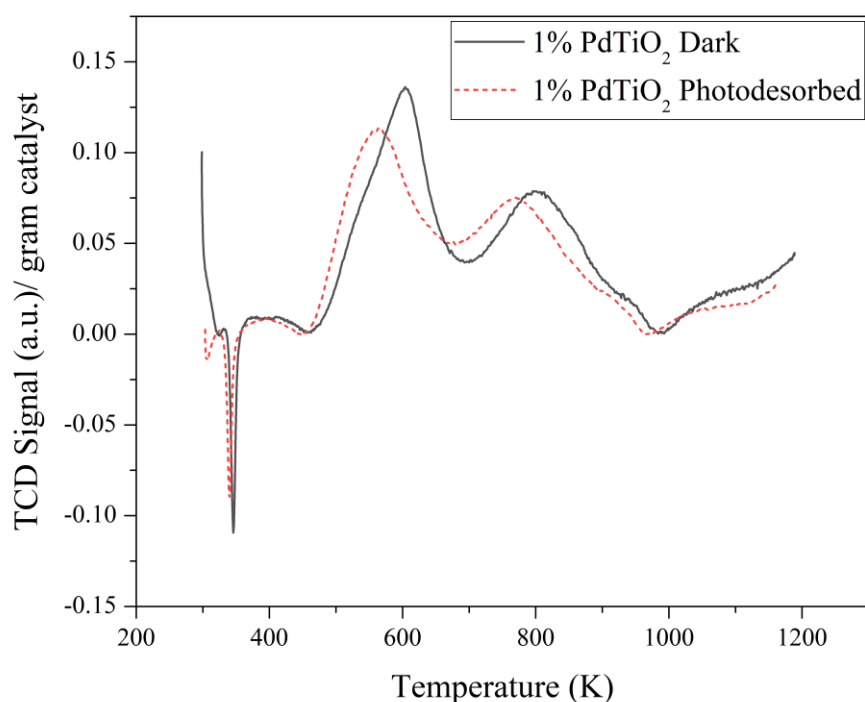
Figure 4.17. TPR profiles of 1%Pd-TiO$_2$ dark and photo desorbed

Similarities of UV treatment and hydrogen treatment were analysed by photo desorption TPR analysis and resulting profiles are presented in Figure 4.17. UV treatment (photo desorption) was done by illuminating the sample inside TPR reactor with UV irradiation under flow of He gas for two hours at room temperature. After that sample was exposed to a regular TPR experiment. The amount of reduction achieved by photo desorption were compared with non-treated sample via quantitative analyses of TPR profiles. Decrease in total H$_2$ consumption after UV treatment was found as 0.45% (Table 4.4). This suggests that some of the surface species were already reduced by the electrons exited upon UV illumination and hence UV exposure can cause hydrogen reduction equivalent effects.

Table 4.4 Quantitative TPR Analysis for Photo Desorbed and Fresh Pd/Titania

Sample	Treatment	Reduced amount (%)
1%Pd/TiO$_2$	Untreated	4.57%
1%Pd/TiO$_2$	Photo desorbed	4.12%

4.3.2 ESR Analysis of Pd/TiO$_2$
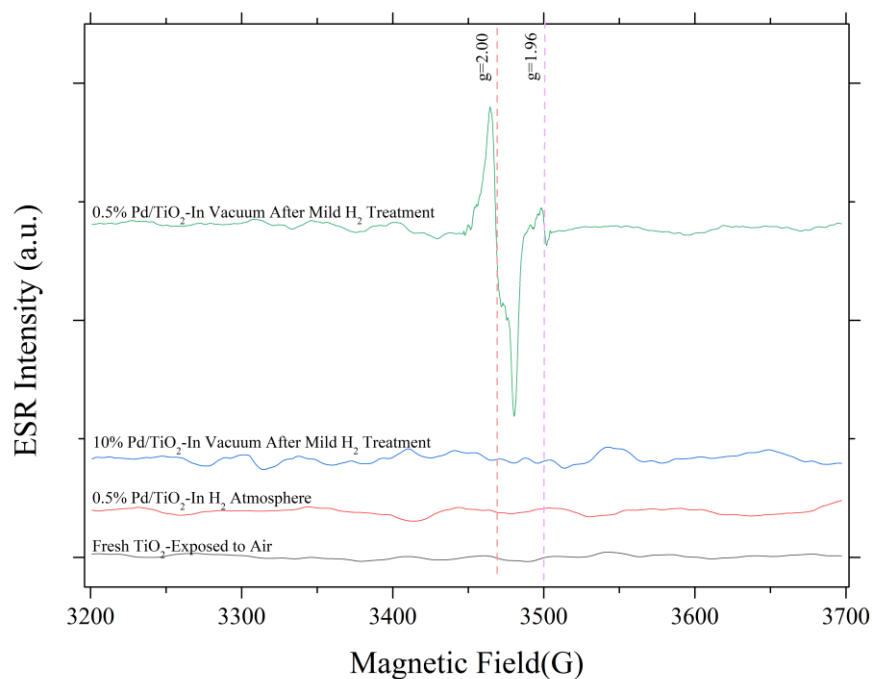
Figure 4.18. ESR spectra

Fresh and 0.5% and 10% Pd loaded titania samples were analyzed *in-situ* with ESR in air atmosphere, under low hydrogen pressure (~0.13 bar) and at vacuum condition following low pressure hydrogen treatment. All the samples were treated at room

temperature, as well as all the ESR scans were done at room temperature. As shown in Figure 4.18, only $0.5\%Pd/TiO_2$ after hydrogen treatment showed paramagnetic behavior with two signals at 3500 G and 3450 G. ESR profile was simulated using the code presented in Appendix H and the resulting simulation is given in Figure 4.19:
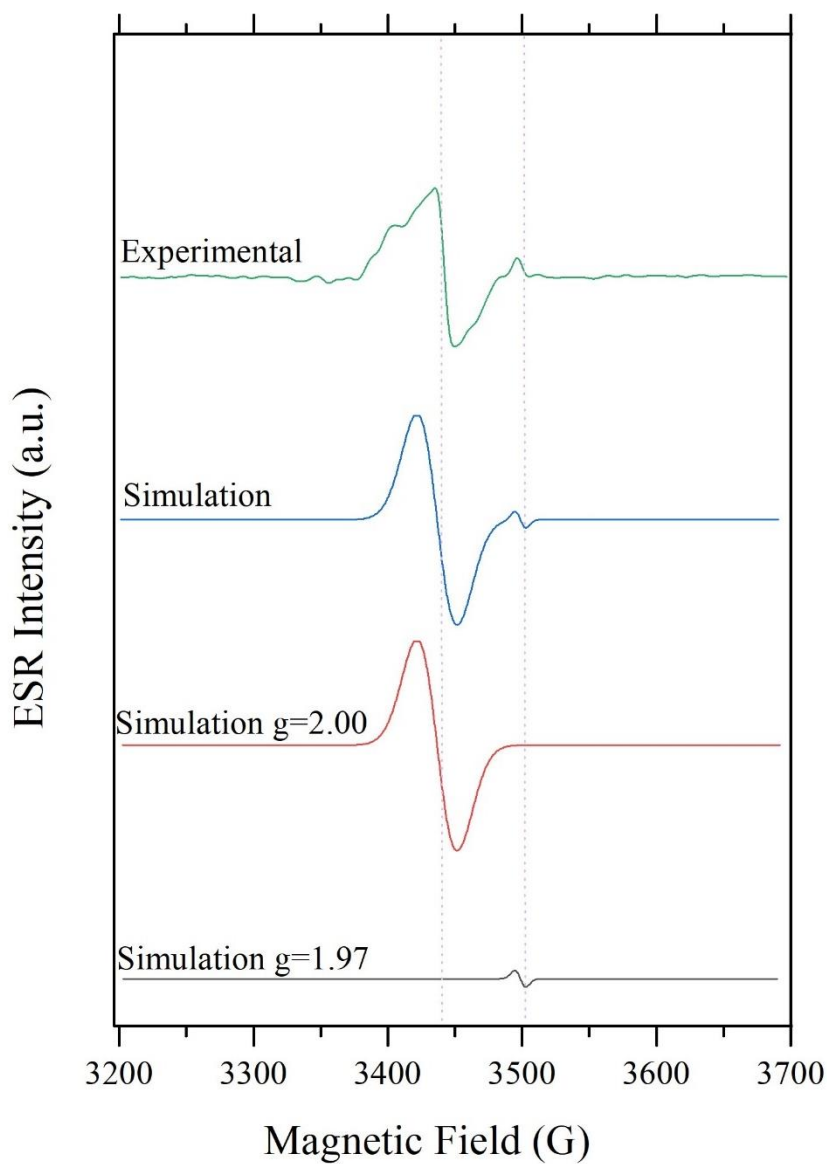
Figure 4.19. Experimental ESR spectrum of 0.5%Pd/TiO$_2$ and simulated ESR signals

The signal with a g value smaller than 2.00 (g=1.97) is emanating from Ti^{+3} species and can be attributed to localized electrons trapped in titania lattice and consistent with the reports of similar studies in the literature [151–155]. On the other hand, the signal with a g value of 2.00 is attributed to oxygen vacancies[13,156–158].

Although mild pressure and temperature hydrogen treated 0.5%Pd/TiO$_2$ showed paramagnetic behavior, this was not the case for pure titania. It was not possible to obtain any signal for pure titania in any condition. Hence, it is proven that Pd incorporation is responsible for reduction of titania surface at room temperature via mild pressure hydrogen treatment. However, contrary to 0.5% sample, 10% Pd loaded sample was also ESR silent in all the used experimental procedures. Hence, in accordance with TEM and TPR experimental results, once again only at low Pd loadings, at the amount that leads to the formation of thin Pd layer, relation between Pd-titania leads to the reduction of support.

The same spectra obtained in this work was previously detected by other researchers using UV treatment[14,158,159] or high temperature/pressure hydrogen treatment (namely black titania production)·[40,160–162]. As a result, equivalent of black titania can be obtained at mild hydrogen pressure and ambient temperature by the use of Pd as a reduction promoter. The spectrum is also in accordance with the previously reported spectra in literature which were measured at cryogenic temperatures[157,158,163].
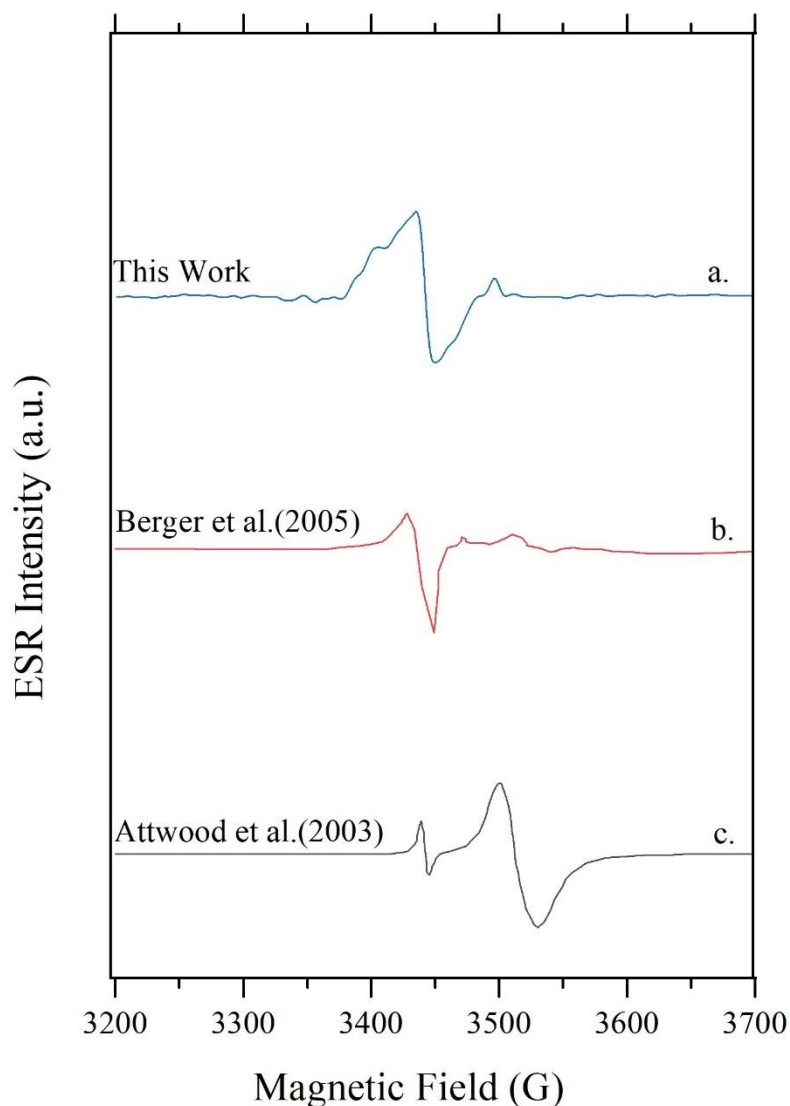
Figure 4.20. Comparison of ESR spectrum obtained in this work to literature results reproduced from b) ref. [158] and c) ref. [157]

ESR signal obtained from mild-pressure and temperature hydrogen treated 0.5%Pd/TiO_2 and recorded under vacuum condition and room temperature was resembling the spectra obtained at cryogenic temperatures as low as 90K on UV irradiated or high-pressure hydrogen treated titania which is named as 'black titania'.

In Figure 4.20 given two sample data from literature. First spectrum was reported by Berger et al.[158] when anatase titania was treated with UV irradiation and ESR scan was done at 90K. The spectrum shows two signals of which g=2.00 was assigned as oxygen vacancy and g=1.95 was assigned as rising from Ti^{+3} species. The second spectrum is taken from Attwood et al.[157]. As reported, following a hydrogen reduction at 873K g=2.003 and g=1.962 signals was obtained at 100K. As a result, it can be concluded that at room temperature and vacuum condition, similar spectra to the ones that obtained at extreme low temperatures can be produced.

The quality of an ESR signal depend on the difference in population densities in the energy levels supplied by Zeeman Splitting and modelled by Maxwell-Boltzmann Distribution. In order to maintain a high population difference between high and low energy levels a high microwave power should be used to be able to send more spins to upper state. In addition to that relaxation rate of species excited to upper energy level can be adjusted to ensure a higher number of species turn to lower state to be excited again. The adjustment of relaxation rate can be done through manipulating the correlation time of fluctuations of magnetic field experienced by spins which is induced through molecular motion of molecules. As the temperature decreases, correlation time is increased due to slower motion of molecules and spin-lattice relaxation time constant T_1 decreases. All these changes lead to a faster relaxation and hence a stronger signal with a narrower linewidth is obtained. That is why, many choose to work in cryogenic temperatures. In addition to low temperature strategy, a second way is shown to be effective in this work which is to decrease of molecular motion through decreasing the pressure on the sample. As the pressure drops, molecular motion slows down and T_1 is predicted to be decreased. The spectrum obtained from $0.5\%Pd/TiO_2$ at vacuum condition provides a proof to this hypothesis.
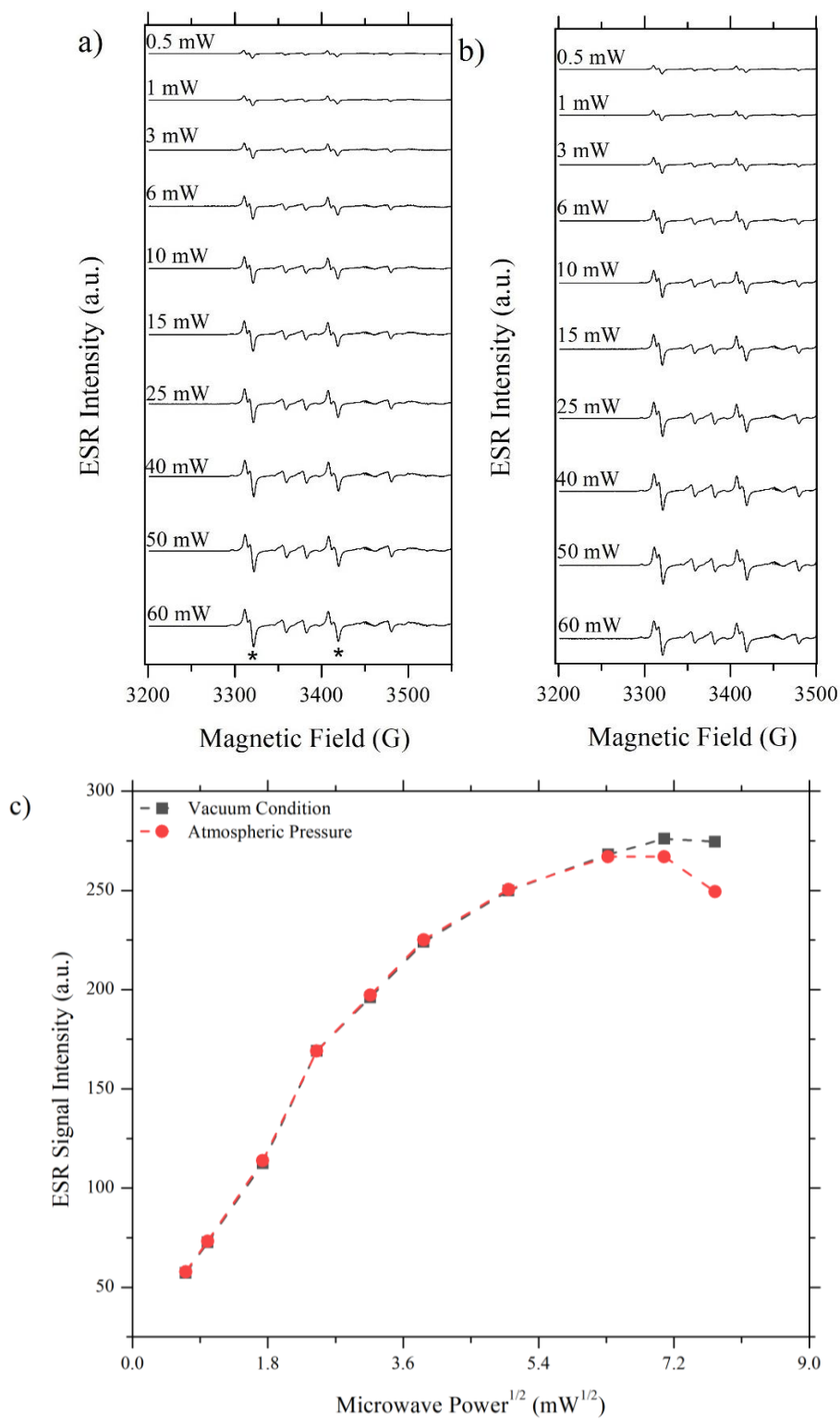
Figure 4.21. Saturation-recovery CW-ESR spectrum a) In vacuum b) On atmospheric pressure c) Microwave power vs signal intensity curve

In order to prove this hypothesis correct, a saturation recovery CW-ESR experiment was done by the standard ESR sample supplied by Bruker: Mn(II) impurity trapped in plasticine. The ESR standard sample was used since it was not possible to obtain a signal from Pd/TiO_2 sample at high pressure. Spectra recorded using all available microwave power values in a Bruker MicroESR spectrometer are given in Figure 4.21.a and b, in vacuum and at atmospheric air pressure, respectively while keeping any other experimental parameter constant. In Figure 4.21.c comparison of changes in signal intensity with respect to square root of microwave power is done for vacuum and high-pressure condition. As can be seen, the optimum signal was obtained at 50 mW ($P^{1/2}$=7.07 $mW^{1/2}$) for both atmospheres however, as microwave power increases a more significant decrease in signal intensity was detected for the sample exposed to high-pressure. As a result, it is concluded that since molecular motion is faster at high-pressure, relaxation process is slower such that it cannot effectively oppose microwave transitions to upper state, spins accumulate at higher energy level and signal saturates more easily than vacuum counter-part. This proves that decrease in pressure directly affect the relaxation rate.
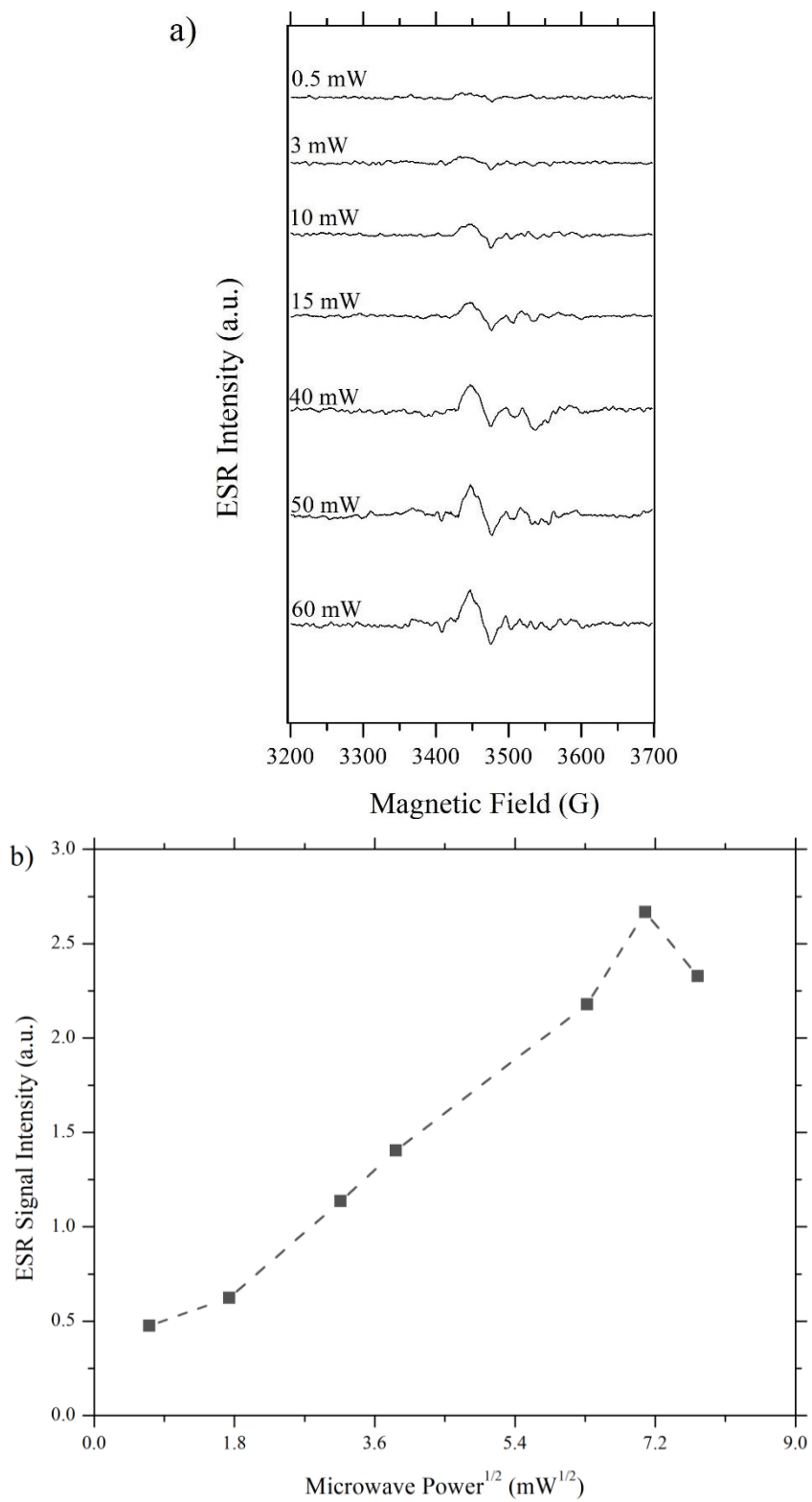
Figure 4.22. a) Saturation-recovery CW-ESR spectra of 0.5%Pd/TiO$_2$ in vacuum b) Microwave power vs signal intensity graph

In vacuum, the same saturation-recovery experimental procedure was repeated for 0.5%Pd/TiO$_2$ sample and respective results are given in Figure 4.22. Pd/titania sample exhibit the same behaviour as in Figure 4.21.c such that as microwave power is increased above 50 mW signal saturation occurs.

Ultra-high vacuum ESR experiments is performed in academic research frequently. However, the perspective of incorporating high vacuum to ESR experiments is through eliminating adsorbing species that leads to occupation of paramagnetic centres[164,165]. Nonetheless, experimental results in this work show that vacuum can serve enhancement of ESR signal through regulation of relaxation rate in addition to eliminating adsorbing species. If the signal enhancement in vacuum was only due to lack of adsorbing species, it was expected to detect a lower signal intensity at any value of microwave power at atmospheric pressure than its vacuum exposed counterpart. However, difference in signal intensity was detected for microwave powers where saturation phenomena take over. Hence, it provides a direct proof that, signal enhancement principles lie in the relation between relaxation rate supplied by fluctuations and microwave induced transitions.

4.3.3   NMR Results

4.3.3.1   Pd/TiO₂ NMR Results
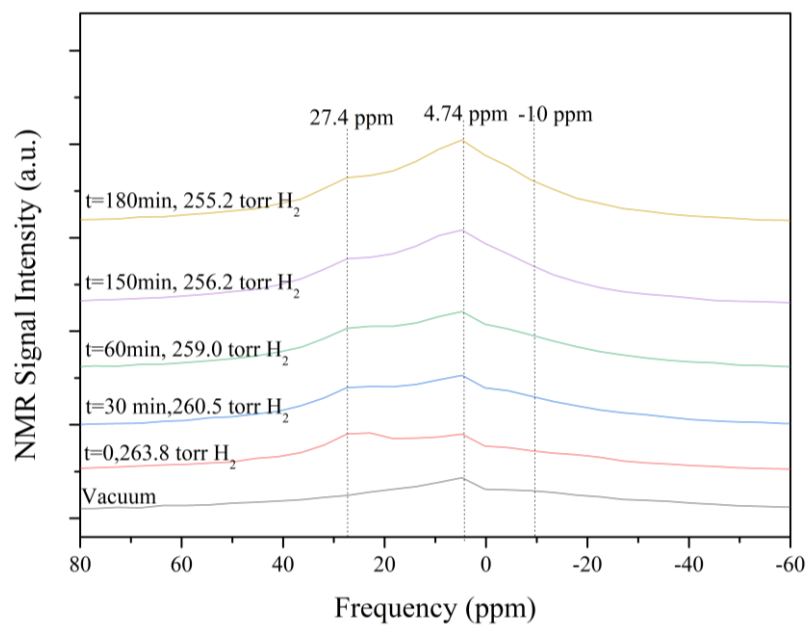
Figure 4.23. Time dependent *operando* NMR analysis for 1%Pd/TiO₂
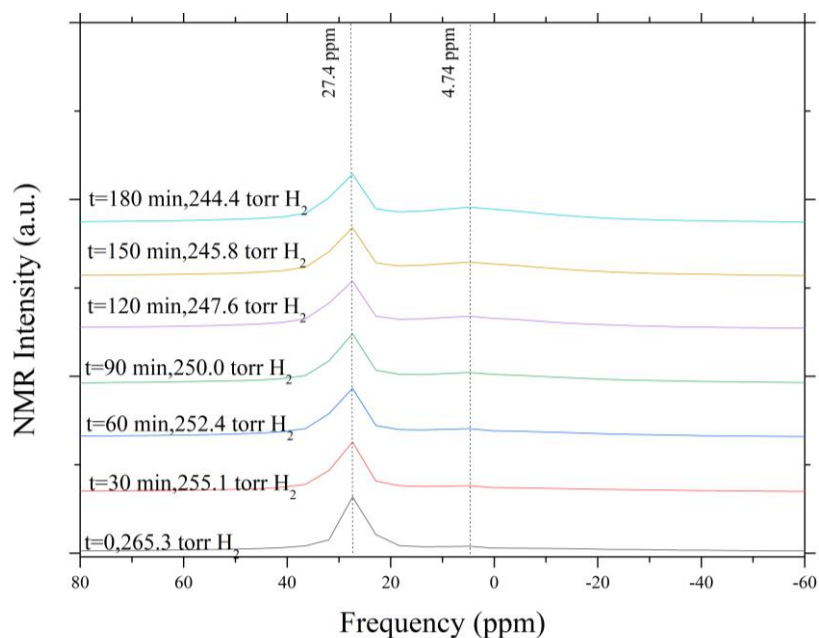
Figure 4.24. Time dependent *operando* NMR analysis for 5%Pd/TiO₂

1% and 5%Pd/TiO$_2$ samples were treated with 300 Torr H$_2$ at room temperature inside the NMR tube connected to a manifold at which the environment was controlled. Both hydrogen pressure and *operando* ^{1}H pulse NMR Spectroscopy scans were recorded throughout the time dependent experiment of 180 minutes. Two main signals at 27.4 and 4.74 ppm detected for both samples (Figure 4.23 and Figure 4.24). The signal at 27.4 ppm was assigned to PdH species while 4.74ppm signal to hydroxyl species. Observation of PdH species after room temperature exposure to H$_2$ indicate that under this condition nitrate species cannot be present. In both profiles hydroxyl signal area is found increasing with longer time, meaning that the chemical environment that leads to hydroxyl signal was increasing in amount in time.
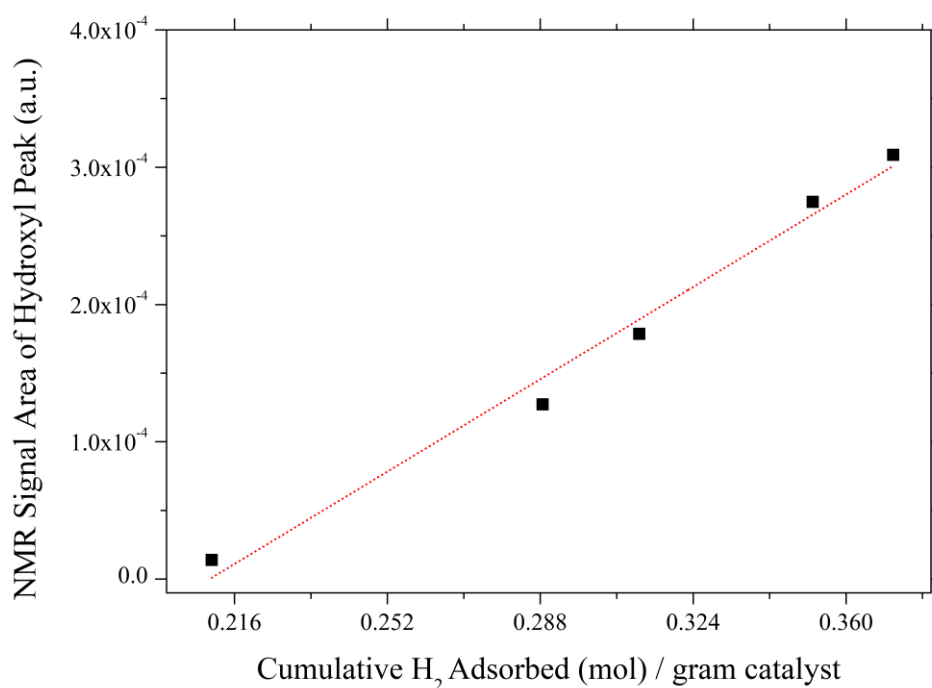
Figure 4.25. NMR signal area vs adsorbed hydrogen comparison curve

Hydroxyl species are formed by one hydrogen atom dissociated from H$_2$ gas inside the sample chamber by Pd particles and one oxygen atom captured from titania surface. Since the change in hydrogen gas pressure throughout the experiment was recorded, the moles of consumed hydrogen were calculated via chemisorption measurements. Since, the amount of hydrogen atoms adsorbed by sample is equal to

the number of hydrogen atoms that contributed to the formation of hydroxyl species, chemisorption data and NMR area of hydroxyl signals can be compared. The curve obtained for the comparison is given in Figure 4.25. This revealed that hydroxyl signal area is directly related to the cumulatively adsorbed hydrogen which indicates the hydroxyls formed can be quantified using NMR data.
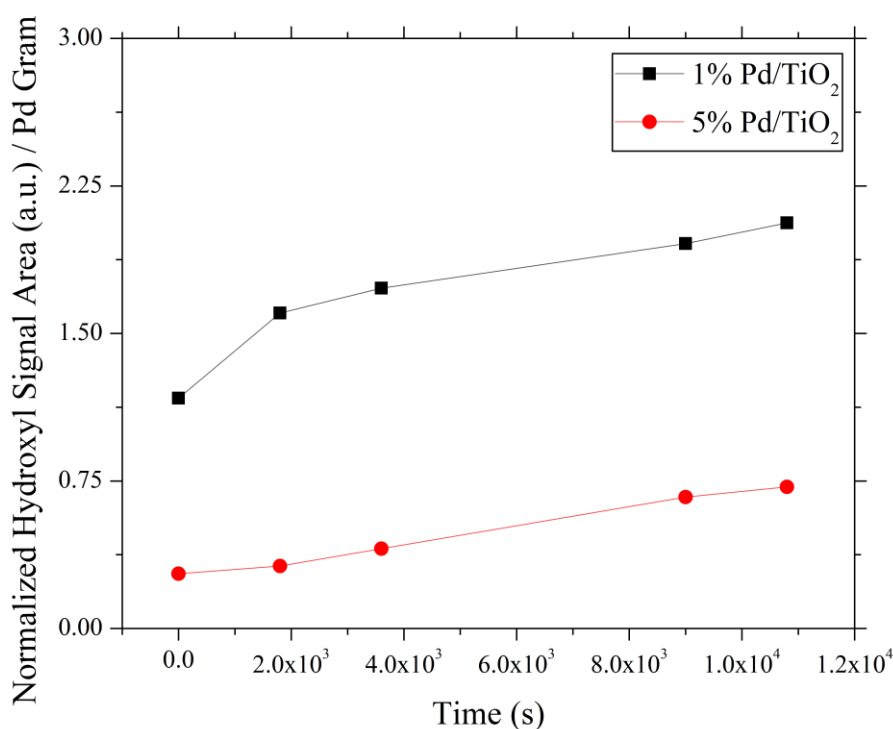
Figure 4.26. Hydroxyl signal area comparison for 1% and 5%Pd/TiO$_2$

The quantification was done by normalizing the hydroxyl signal area at any time, t with respect to the hydroxyl signal area under vacuum condition prior to hydrogen exposure and to Pd amount in the sample. As proved by Figure 4.26, amount of hydroxyl formed shows a sharper increase in 1%Pd/TiO$_2$ sample than 5% Pd/TiO$_2$ at the beginning of hydrogen exposure. This suggests that since the metal-support interface area is higher in 1% Pd/TiO$_2$ sample than 5% Pd/TiO$_2$ sample, atomic transfer between the two is enhanced. As hydrogen exposure time increase, hydroxyl production rate in the two samples starts to follow the same rate as indicated by slope

of lines being equal for t>2x10^{3}s in Figure 4.26. This behaviour suggests that the process becomes independent of Pd layer and in fact atomic hydrogen starts to diffuse through titania surface.

On the basis of hydrogen spillover and oxygen reverse spillover phenomena, oxygen or hydrogen atoms on hydroxyl species is reached to metal-support interface by following a path through Pd layer on the surface. Taken this into account, quantified NMR data can be fitted to a diffusion model to estimate the layer thickness of Pd. The model was the equations derived by J. Crank[166] for a spherical particle with concentration fixed at surface boundary (imposed by gas phase hydrogen). A sample model for a diffusion constant of D= 7x10^{-25}m^2/s is given in Figure 4.27. Keeping diffusion constant at any fixed arbitrary value in both samples, Pd layer thickness at 1% Pd/TiO$_2$ sample is always yielded to be thinner than 5% Pd/TiO$_2$ sample.
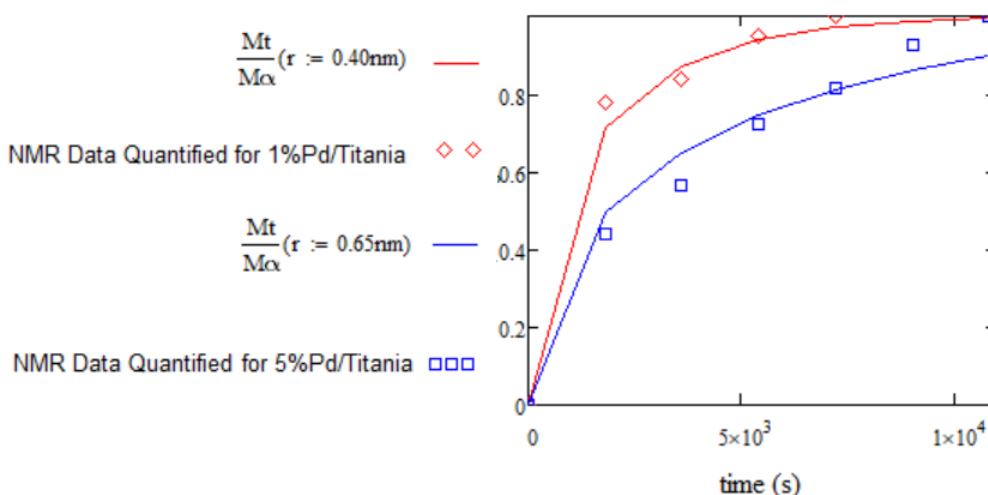
Figure 4.27. Diffusion model for quantified NMR signal

Diffusion model results correlate well with the outcomes of TEM, TPR and ESR experiments. The common result can be concluded from all these evidences is that: thin layer Pd formed at small amount of Pd on titania surface leads to an enhancement in metal-support interface. Enhanced interface leads to a more intimate relation between metal and support. This increases the atomic transfer rate between two which accounts for acceleration of titania surface reduction at mild conditions for low Pd loaded samples.

64
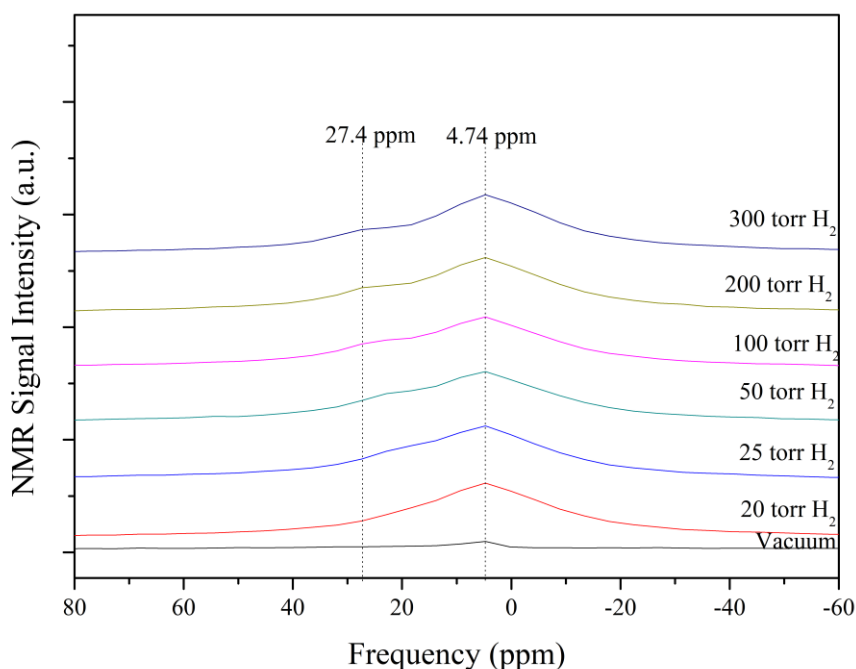
Figure 4.28. Pressure dependent *operando* NMR analysis for 1%Pd/TiO$_2$

1%Pd/TiO$_2$ that was evacuated overnight was exposed to increasing H$_2$ gas pressures between 20 Torr to 300 Torr at room temperature with 30 minutes time intervals while NMR spectra was recorded in each round. In Figure 4.28; results of pressure dependent ^{1}H pulse NMR experiment are given. Reason for not detecting PdH signal at 20 Torr hydrogen pressure is due not enough hydrogen atoms adsorbed on Pd species that is in the detection range of the spectrometer. As can be seen, with increasing hydrogen pressure, amount of PdH phase increases as well as the hydroxyls formed. These results are in accordance with time dependent experiments that oxygen atoms captured from the sample via spillover mechanism. At each round inversion-recovery experiment and T$_2$-decay experiments were also done to measure T$_1$ and T$_2$ relaxation times, respectively and results are given in Figure 4.29:
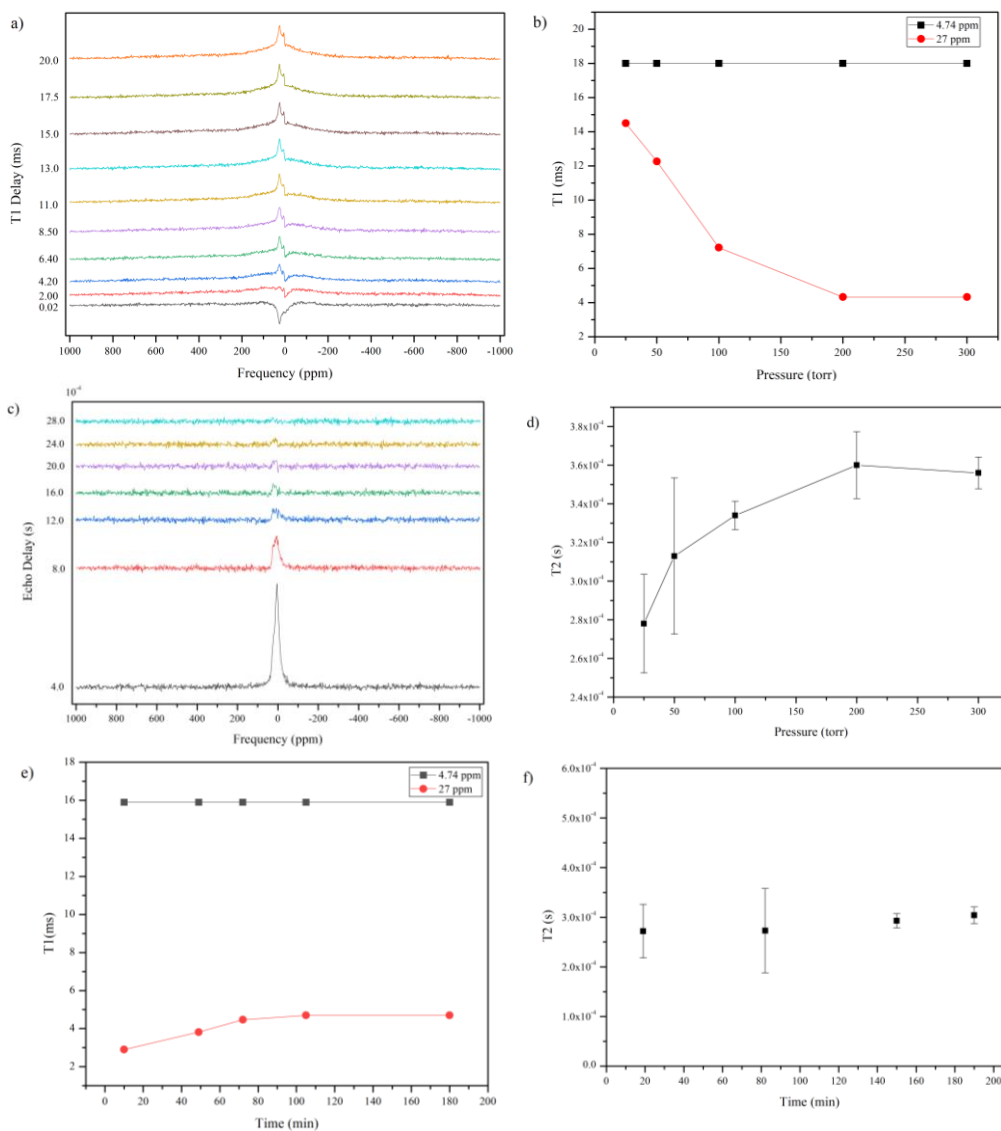
Figure 4.29. a) Inversion-recovery experimental results b) T_1 vs pressure curve c) T_2-decay experimental results d) T_2 vs pressure curve e) T_1 vs time curve f) T_2 vs time curve

66

In Figure 4.29.a and c, examples of T_1 and T_2 measurements are given while Figure 4.29.b and d show the T_1 and T_2 behavior with respect to hydrogen pressure. Spin-lattice relaxation time of 4.74 ppm signal, hydroxyl signal, showed no dependence on the pressure with a value constant at 18×10^{-3}s while 27.4 ppm, palladium hydride signal, showed a decrease in relaxation time upto 4.3×10^{-3}s with increasing pressure. Additionally, a single spin-spin relaxation time was detected and it is increased with increasing hydrogen pressure reaching a steady value of 3.5×10^{-4}s after 200 Torr.

On the other hand, Figure 4.29.e and f show the T_1 and T_2 measurement results as a function of time under 260 Torr hydrogen pressure. Similar to pressure dependent measurement, hydroxyl signal showed no change in T_1 relaxation time with respect to time while that of palladium hydride signal increased over time until reaching a steady value of 4.7×10^{-3}s after 80 minutes. This increase in T_1 time of hydride signal is due to pressure being decreased over time as more hydrogen get adsorbed on the surface decreasing the hydrogen pressure with time which is in accordance with pressure dependent measurements. Furthermore, spin-spin relaxation time was found to be independent of time with a value of 2.72×10^{-4}s.

These results indicate that these two species interact with lattice independent of each other and only palladium hydride is in relationship with gas phase hydrogen while they are correlated in terms of spin-spin interactions which is indicated by a single T_2 relaxation time. It can be concluded that although Pd-H and OH species are in close enough interaction with each other that allow themselves to exchange magnetization with each other, they are independent on energy dissipation processes. Spin-lattice relaxation time can be understood as a measure of energy dissipation ability of particular species and hence, since their lattice is different from one another, their thermal dissipation events are distinct and only that of PdH is affected by pressure, which slows down if pressure decreased.

4.3.4   Solid State UV-Visible Spectroscopy Results

Solid state UV-Visible results for bare and 0.5%, 1%, 2% and 10%Pd/TiO$_2$ samples are given in the figure below:
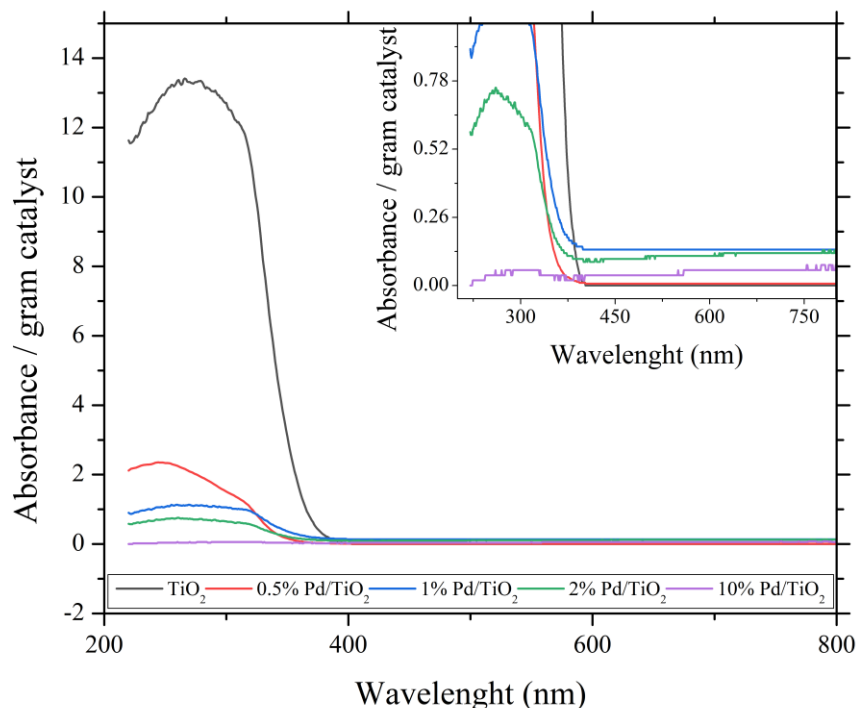
Figure 4.30. Solid state UV-Visible spectroscopy results

As seen in Figure 4.30, bare titania shows the highest UV absorbance while absorbance in UV region decreases with Pd addition with an inverse relationship with Pd loading. The decrease can be explained by Pd particles covering the surface of titania such that UV light cannot reach to full titania surface. On the other hand, as seen, there is no absorbance in visible region on bare titania was detected. However, as seen in Figure 4.30, a slight interaction in visible region for mild temperature and pressure hydrogen treated Pd/TiO$_2$ samples is possible with an inverse relation with Pd amount, except for 0.5%Pd/TiO$_2$.

4.4   CO Oxidation Results

0.1-0.5 grams of synthesized-fresh Pd/TiO_2 catalysts were subjected to catalytic tests for CO oxidation reaction at temperatures changing from room temperature to $300^{\circ}C$ under CO-air mixture flow at different rates changing in the range of 20-370 ml/min. A sample results for CO and CO_2 concentration change during reaction on $0.5\%Pd/TiO_2$ at 20 ml/min reactor inlet flow rate and $200^{\circ}C$ is given in figure below:
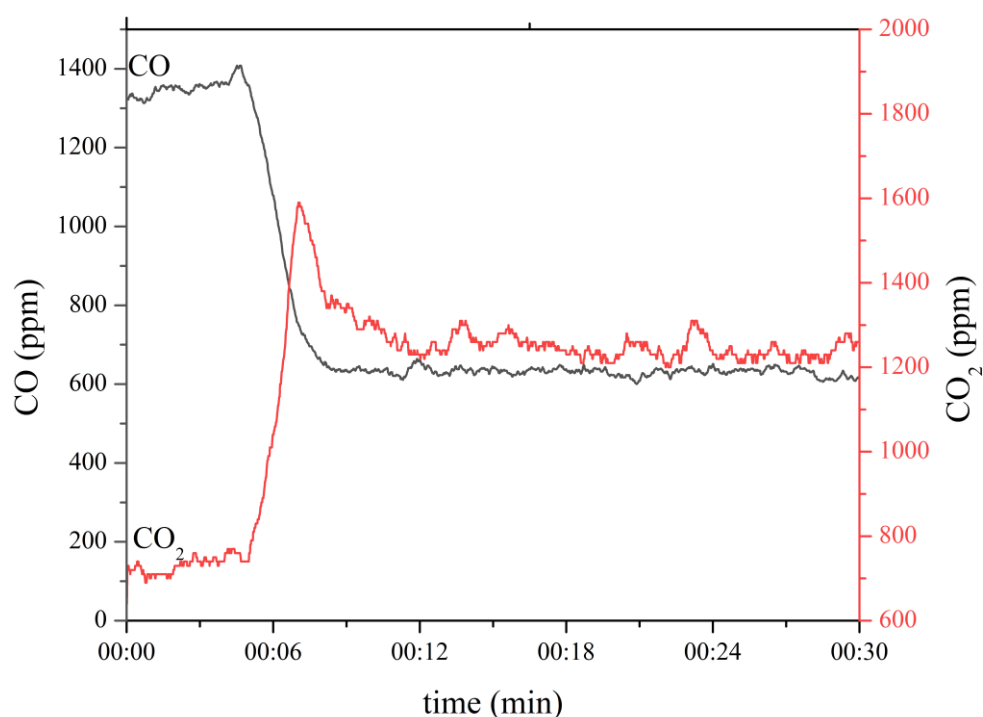
Figure 4.31. CO concentration (ppm) and CO_2 concentration (ppm) during CO oxidation on $0.5\%Pd/TiO_2$

As seen in Figure 4.31, for 0.5% Pd/TiO_2 catalyst, a decrease in CO concentration after heater is turned on is detected. Around 10 minutes steady state CO and CO_2 concentration is reached.

4.4.1 Mass Transfer Limitation Tests

In order to check mass transfer and kinetic limitations, the same experiment was run on different reactor inlet flow rates on 0.1 gram 0.5%Pd/TiO$_2$ catalyst:
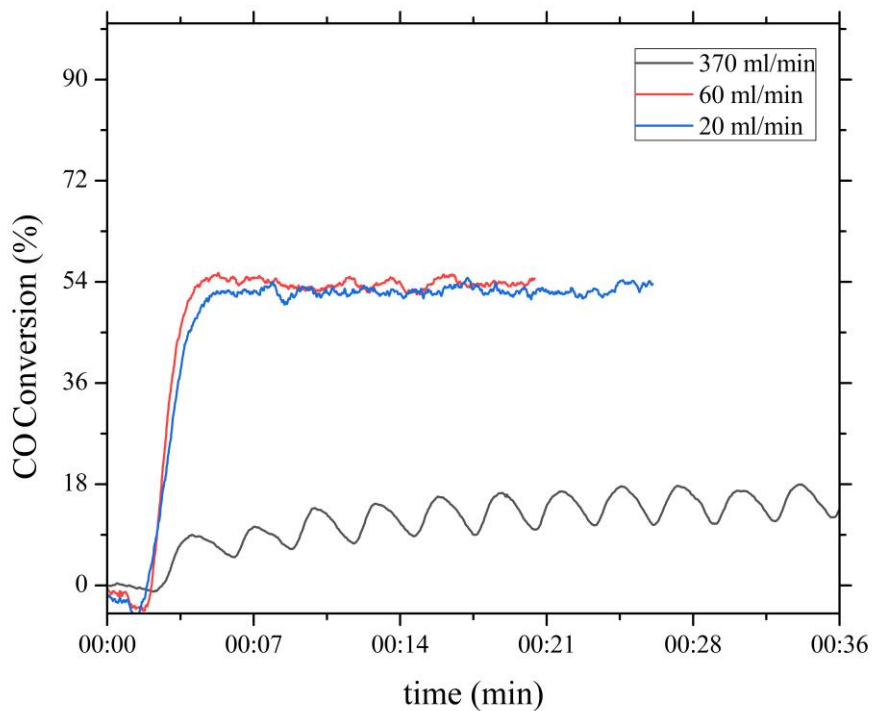
Figure 4.32. CO conversion (%) at different reactor inlet flow rates on 0.5%Pd/TiO$_2$

In Figure 4.32 given the change in CO conversion as a function of reaction time for 20, 60 and 370 ml/min reactor inlet flowrates. As seen, conversion decreases with increasing reactor inlet flowrate after 60 ml/min. However, conversion doesn't increase when flow rate is decreased below 60 ml/min which indicate mass transfer limitations may be dominant for flow rates below 60 ml/min.
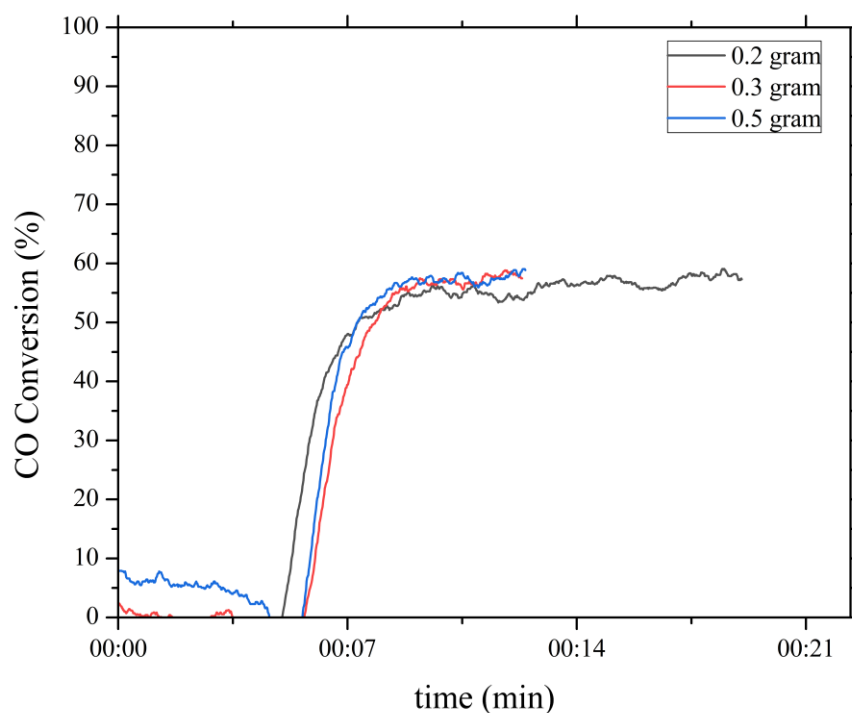
Figure 4.33. CO conversion (%) at different catalyst loadings at 20 ml/min reactor inlet gas flow rate

In Figure 4.33 dependence of CO conversion on the catalyst weight is examined to conclude that at 20 ml/min reactor inlet flow rate, conversion doesn't change when the catalyst amount is changed, indicating that at 20 ml/min mass transfer limitations are dominant.

Same analysis was done for 10%Pd/TiO$_2$ at different reactor inlet flow rates and catalyst weights and respective results are given in Figure 4.34:
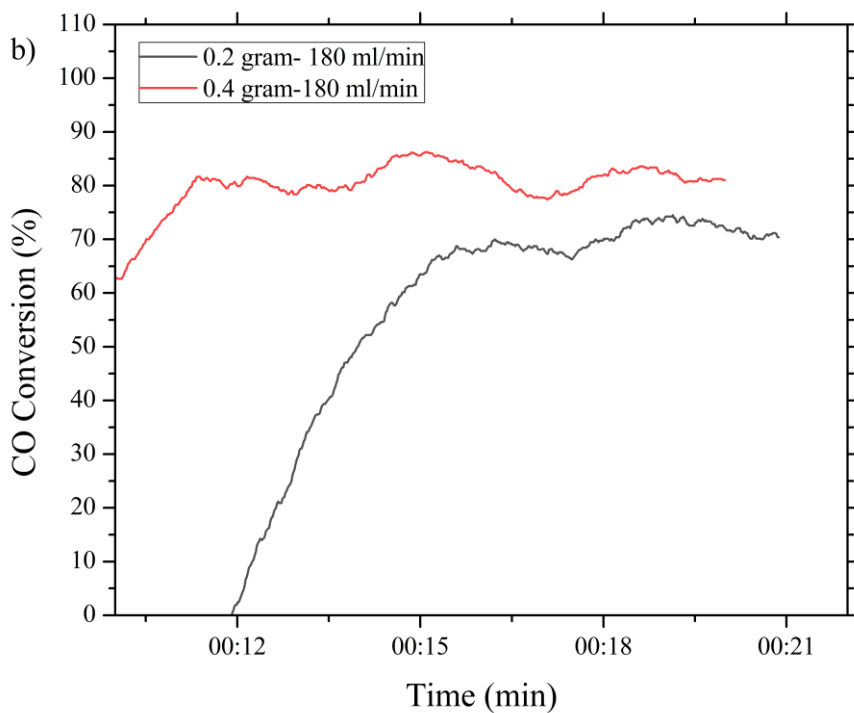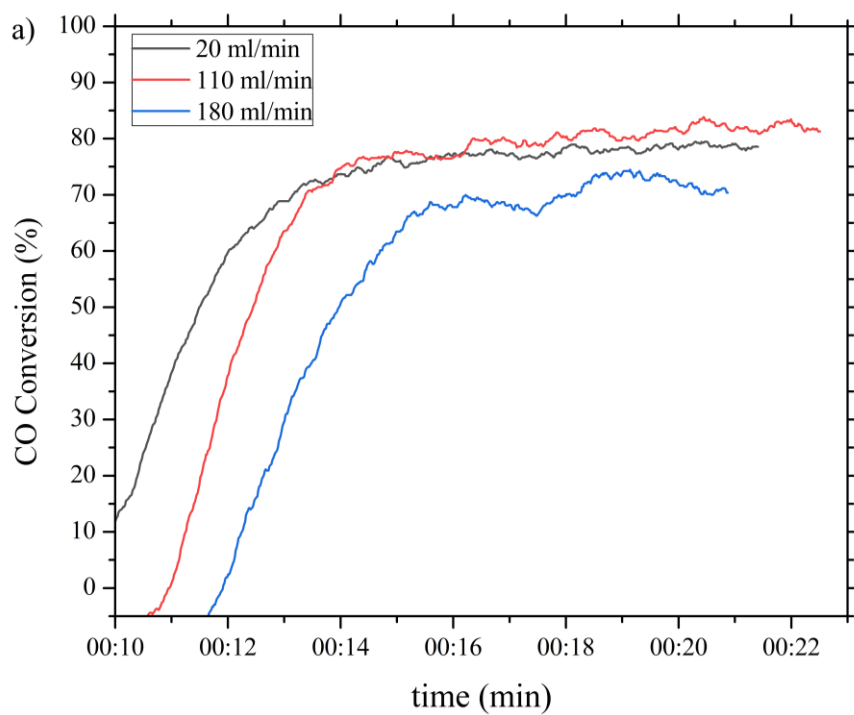
Figure 4.34. CO conversion (%) a) at different reactor inlet flow rates on 0.2 grams 10%Pd/TiO$_2$ b) for different catalyst weights at 180 ml/min

For 10% sample, in accordance with 0.5%, conversion decreases above 110 ml/min and conversion increases when catalyst amount is increased at 180 ml/min flow rate. Since the change in catalyst amount is reflected in conversion, the system is free of mass transfer limitation under gas flow rate of 180 ml/min.

4.4.2   Heat Transfer Limitations Tests

In order to reveal possible heat transfer limitations, exist in the system, reactor loaded with 0.4 grams of 0.5%Pd/TiO$_2$ catalyst was heated from room temperature to 300°C under 180 ml/min CO and air mixture flow rate (CO concentration~1100 ppm) then cooled under natural forces while CO inlet was kept constant. Changes in CO conversion and temperature values throughout the experiment is given below:
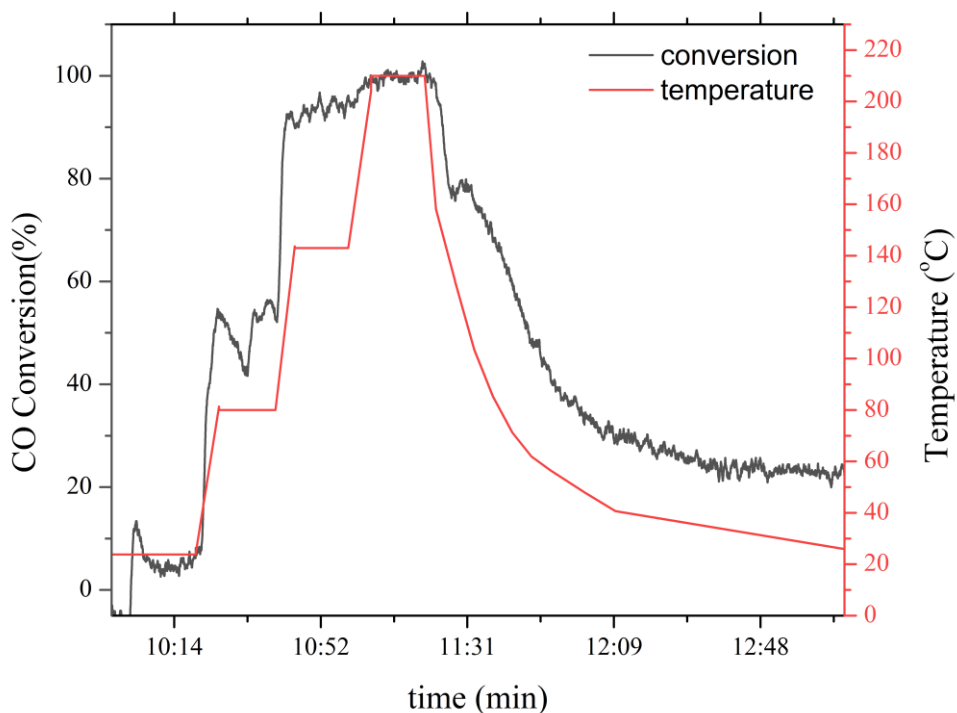
Figure 4.35. Heat transfer limitations test

At the end of this reaction test conversion values during heating and cooling cycles were compared:
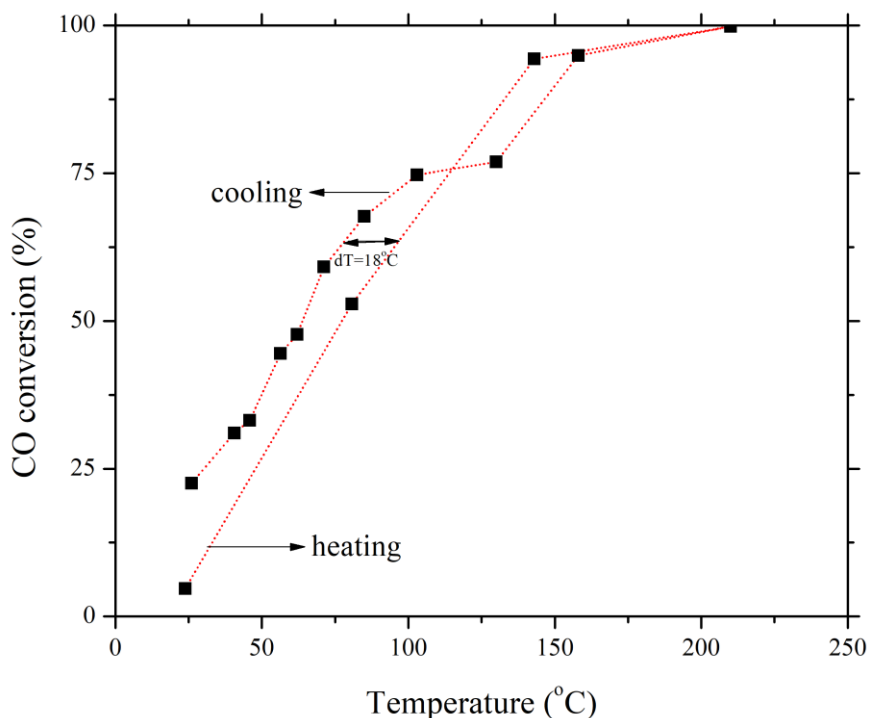
Figure 4.36. Hysteresis for heat transfer limitations test

As seen in figure above a hysteresis between heating and cooling cycles with a difference of 18°C is detected for the system.

4.4.3   Catalytic Activity Tests

CO conversion and CO_2 selectivity at different temperatures were also analyzed on 0.2 grams 0.5, 2 and 10%Pd/TiO_2 catalyst under dark and UV illuminated conditions with 20 ml/min reactor inlet flow rate (CO inlet concentration ~ 1100 ppm). Temperature is increased from room temperature to 200°C with 50°C increments while waiting the steady state to be reached at each temperature for 15 minutes and CO conversion and CO_2 selectivity changes during the experiment are given below:
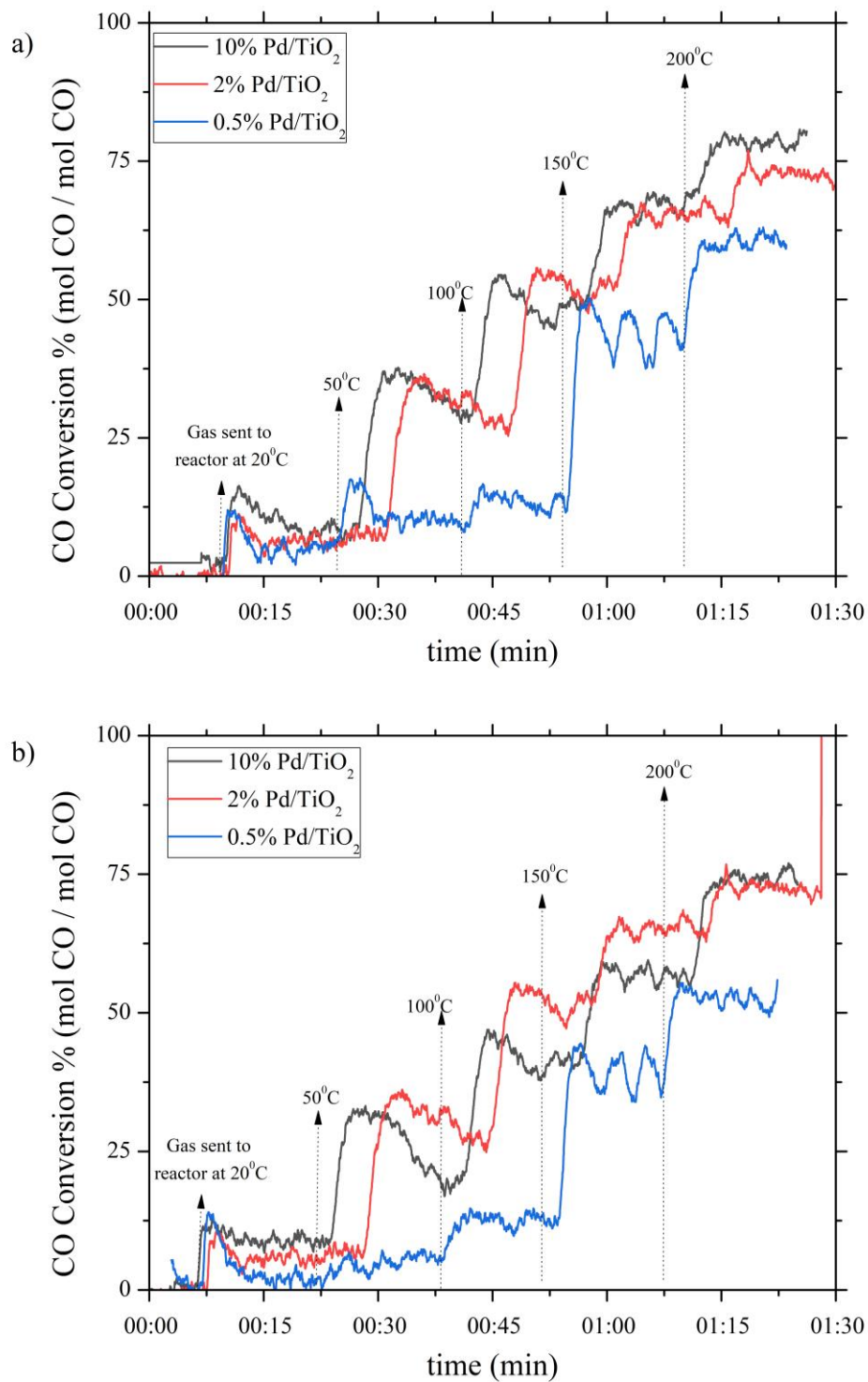
Figure 4.37. CO conversion vs time at different reactor temperatures for %Pd/TiO$_2$ at 20 ml/min gas flow rate a) Dark b) UV illuminated
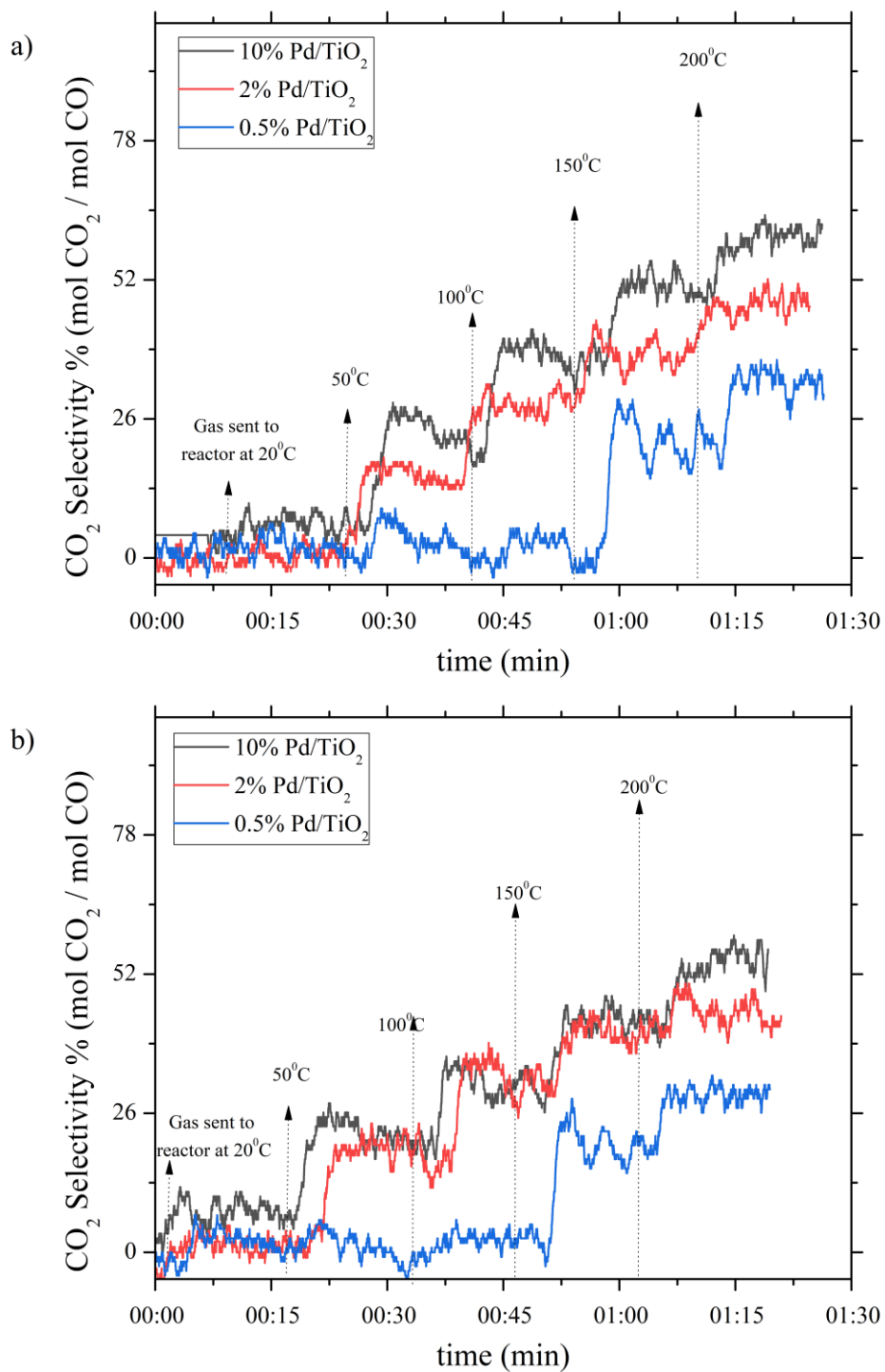
Figure 4.38. CO$_2$ selectivity vs time at different reactor temperatures for x%Pd/TiO$_2$ at 20 ml/min gas flow rate a) Dark b) UV illuminated

Steady state conversion value reached at each temperature is recorded and plotted on figure below:
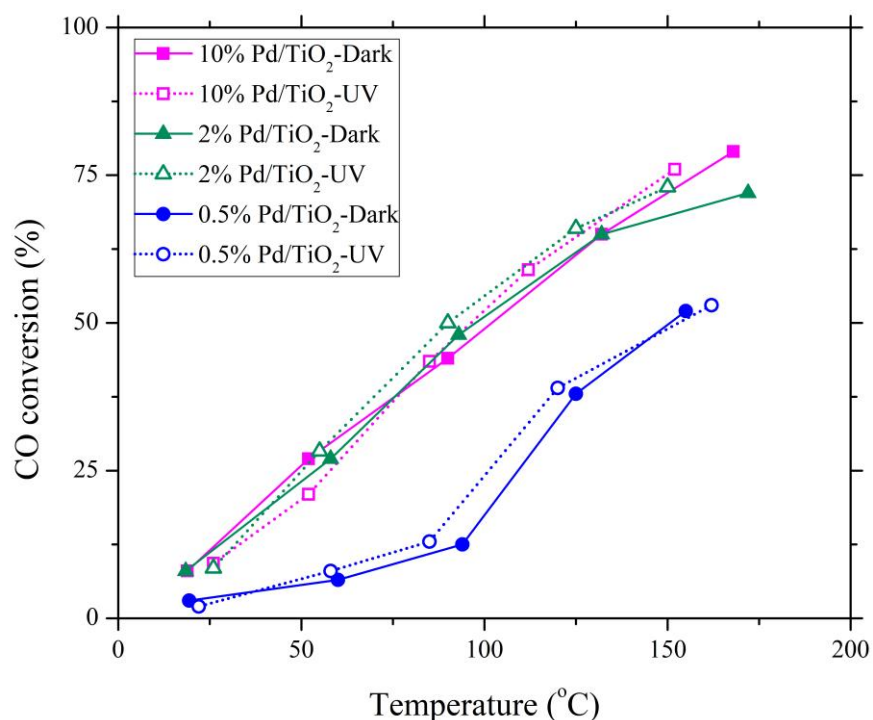
Figure 4.39. CO conversion as a function of temperature for 0.5, 2 and 10% Pd/TiO$_2$ at 20 ml/min gas flow rate under dark and UV illuminated conditions

CO oxidation is very slow for 0.5%Pd/TiO$_2$ for temperatures below 100°C whereas for 2% and 10% oxidation starts even at room temperature then increases with increasing temperature both under dark and UV illuminated conditions. CO conversion is the smallest for 0.5% and highest at 10% for all temperature both dark and illuminated. However, there is a higher increase in CO conversion changing from 0.5% to 2% than 2% to 10%. Since increase in CO conversion is more significant between 0.5% and 2%, the increase is related to 2D nature of the catalyst. For 10% 3D particles were proved to be formed and since the conversion doesn't change significantly at 10% it is also proved that 3D particles contribute less to CO conversion than 2D ones. In addition, CO conversion increases under UV

illumination only slightly at each temperature which is smaller than expected and reported increase in literature[109]. This may be due to reaction being mass transfer limited at 20 ml/min flow rate which was previously proven.

Same experiment was repeated with 0.4 grams of catalyst at 180 ml/min gas (CO concentration ~ 1100 ppm) flow rate at which previously proved that no mass transfer limitations are present and results are given in Figure 4.40, while CO conversion and CO_2 selectivity vs Pd loading plots produced by the data in Figure 4.40 are given in Figure 4.41:
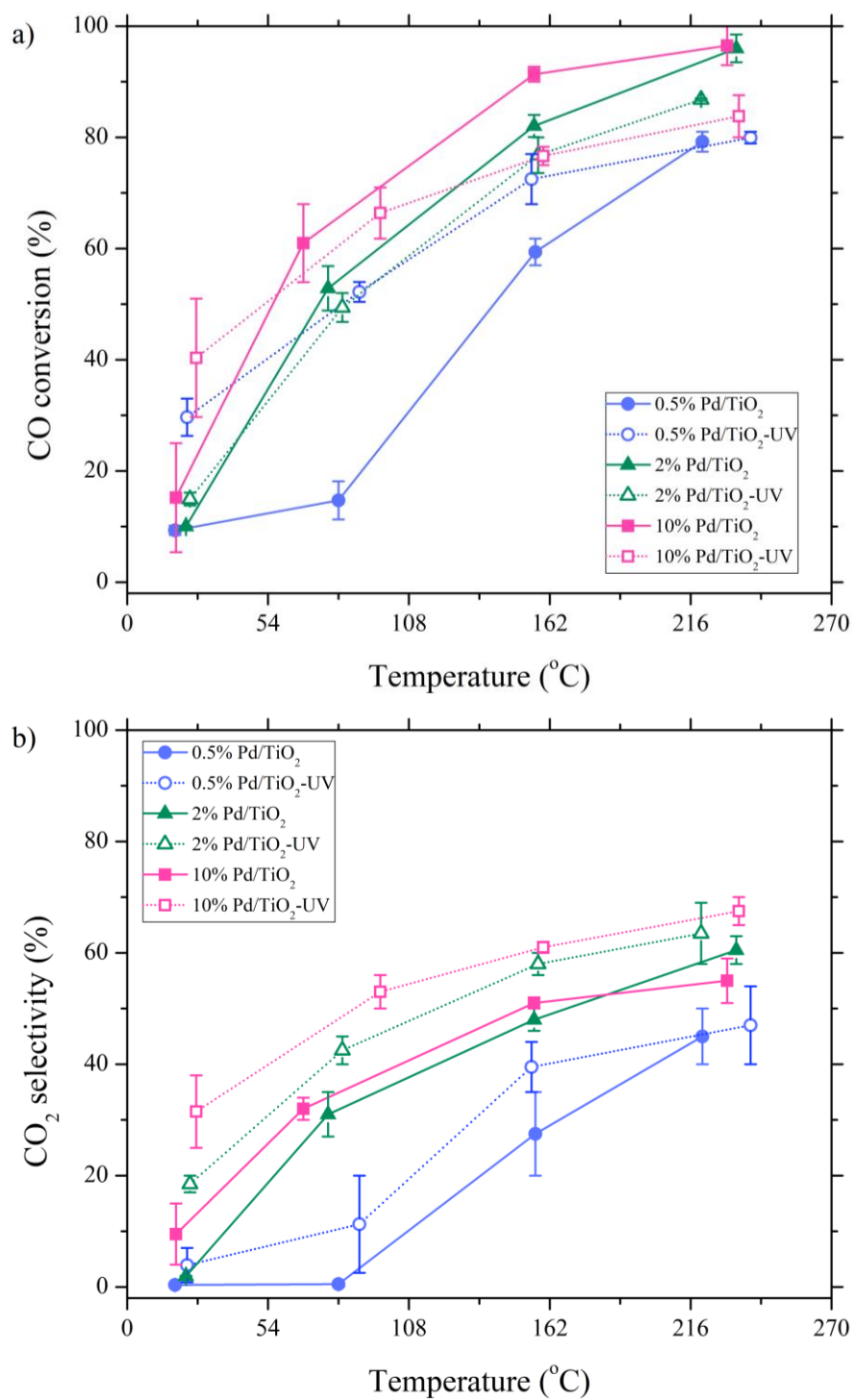
Figure 4.40. a) CO conversion b) CO_2 selectivity as a function of temperature for 0.5, 2 and 10% Pd/TiO_2 at 180 ml/min gas flow rate under dark and UV illuminated conditions
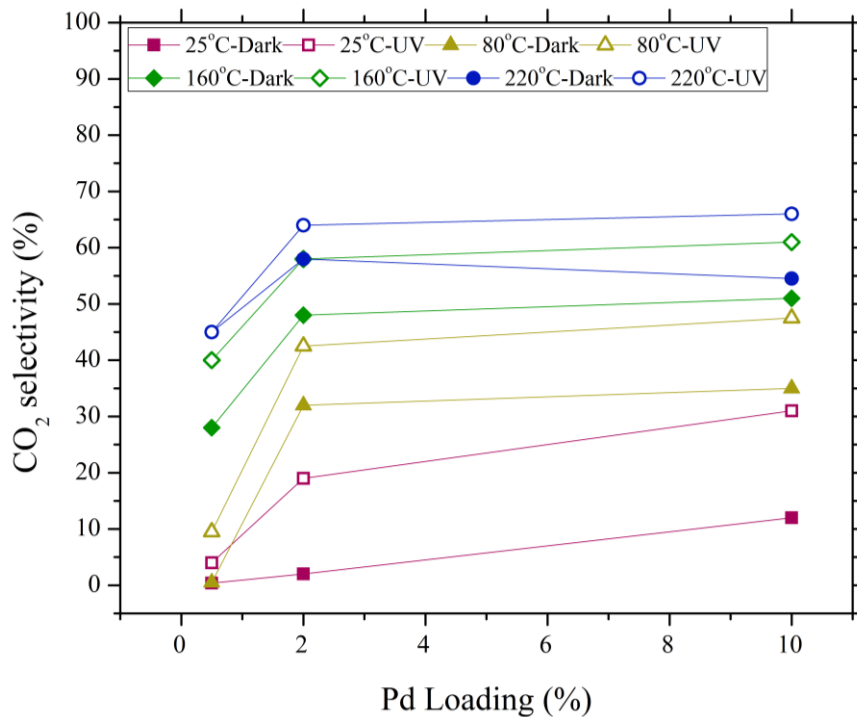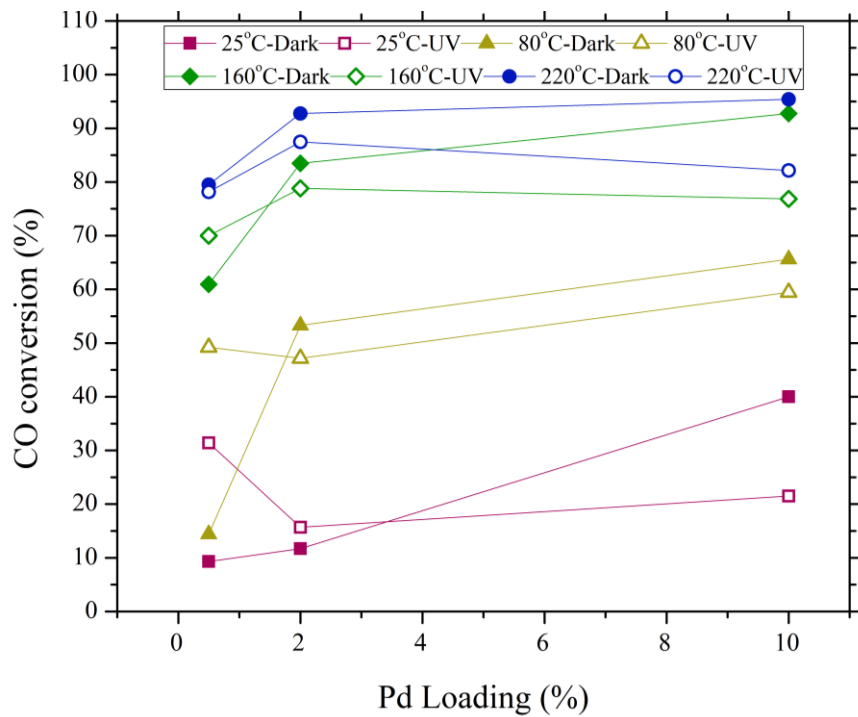
Figure 4.41. CO conversion and CO_2 selectivity vs Pd loading (%) plots

At 180 ml/min flow rate 2% and 10% samples follow a very close path of conversion values at each temperature under dark and UV illuminated conditions while 0.5% shows the lowest conversion in most cases. Since 4 times increase in Pd amount when using 2% instead of 0.5% is reflected on the conversion values, however 5 times more Pd on 10% than 2% doesn't affect the conversion, it can be concluded that only 2D Pd particles can effectively increase CO oxidation conversion while 3D particles cannot. Similarly, this explanation is valid for CO_2 selectivity. As seen in Figure 4.41, selectivity does not increase above 2% Pd loading.

At near ambient temperatures (25 and 80^oC) the most significant increase in CO conversion was detected for $0.5\%Pd/TiO_2$ catalyst. On the other hand, for loadings 2% and 10% CO conversion was decreased when irradiated with UV light, which may be due to coverage of Pd at high loadings preventing UV accessibility of titania surface, in line with solid UV-Visible spectroscopy results. At high temperatures no significant contribution by UV illumination on conversion values was observed for any catalyst.

A final remark should be made on the difference between selectivity and conversion values: conversion is calculated by change in CO amount divided by CO amount at the inlet and selectivity by change in CO_2 amount divided by CO amount at the inlet. Conversion and selectivity values calculated with mentioned methods for 10% Pd/TiO_2 sample at dark condition is given in Figure 4.42.a. As seen while CO conversion reaches 100%, CO_2 selectivity is 52% at the same moment. The difference is due to CO is being adsorbed on the surface which is evident by the experiment done after reaction is complete and both heater and CO inlet was turned off. As seen in Figure 4.42.b under this condition CO_2 concentration is dropped to base value in 5 minutes while CO is observed to be desorbed from the surface for around 3 hours after the reaction is stopped. That's why a difference between conversion and selectivity values calculated using decrease in CO and increase in CO_2 exists.

The mass balance of CO throughout the experiment can be expressed as follows:

$$Moles\ of\ CO\ sent\ in\ to\ the\ system\ through\ the\ experiment\ time$$
$$= Moles\ of\ CO\ leaves\ the\ system\ unreacted$$
$$+ Moles\ of\ CO\ converted\ to\ CO_2$$
$$+ Moles\ of\ CO\ desorbed\ after\ reaction$$

All this values in the mass balance can be calculated from area under curve for CO and CO_2 volume percent values recorded every second throughout the experiment. The conversion between volume percent to actual moles CO is done by the following method:

$$\frac{Moles\ CO}{s} = \frac{volume\ of\ CO\ (ppm)}{10^6 * volume\ of\ analysis\ gas} * \frac{1\ mol\ gas}{22.4\ L}$$
$$* \frac{180\ ml\ gas\ flow\ rate}{min} * \frac{1\ min}{60\ s} * \frac{1L}{10^3 mL}$$

For a sample reaction test and its desorption process after reaction following values are found: total CO inlet was found from measured CO value at reactor inlet and the time CO was sent to reactor. Moles of CO unreacted was found by CO ppm recorded at reactor outlet by gas analyzer and the time reaction continues and same way CO converted to CO_2 by CO_2 (%) at reactor outlet. Finally, moles of CO desorbed after reaction was found by CO ppm after reaction stops and CO flow is cut. For all the calculations rectangular rule was used to calculate the area under CO ppm or CO_2 (%) vs time curves given by gas analyzer. The calculation results are given below:

Table 4.5 CO Mass Balance Calculations

Moles of CO sent into the system through the experiment time	1.09E-03
Moles of CO desorbed after reaction	3.52E-04
Moles of CO converted to CO_2	1.16E-04
Moles of CO leaves the system unreacted	5.48E-04
Total :	1.02E-03

By the results given in Table 4.5, mass balance holds for CO with 6.41% error.
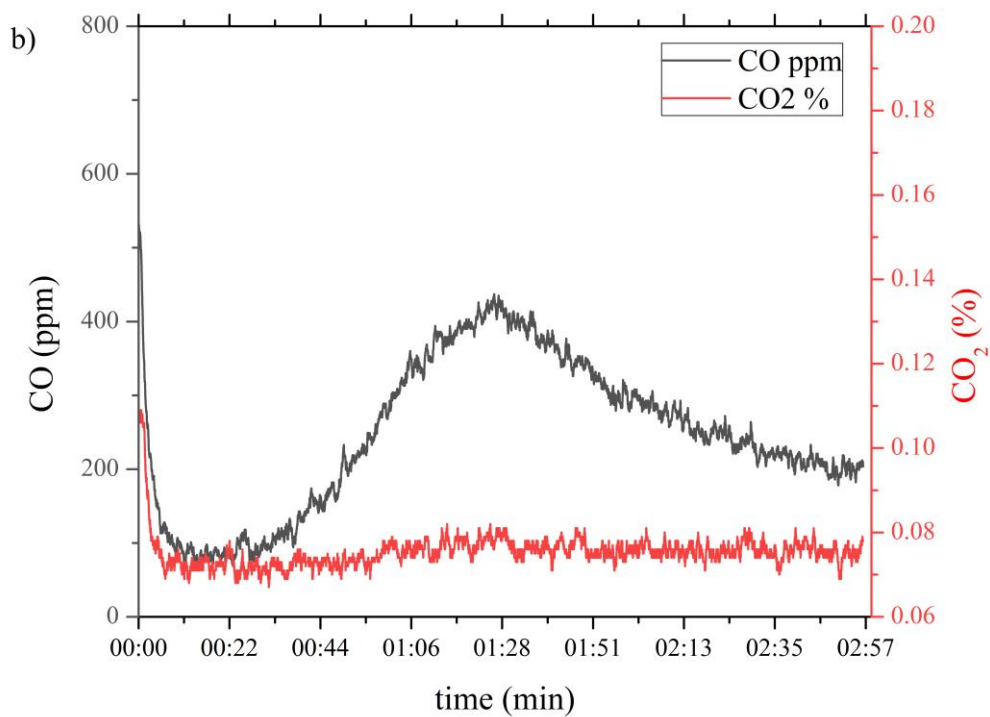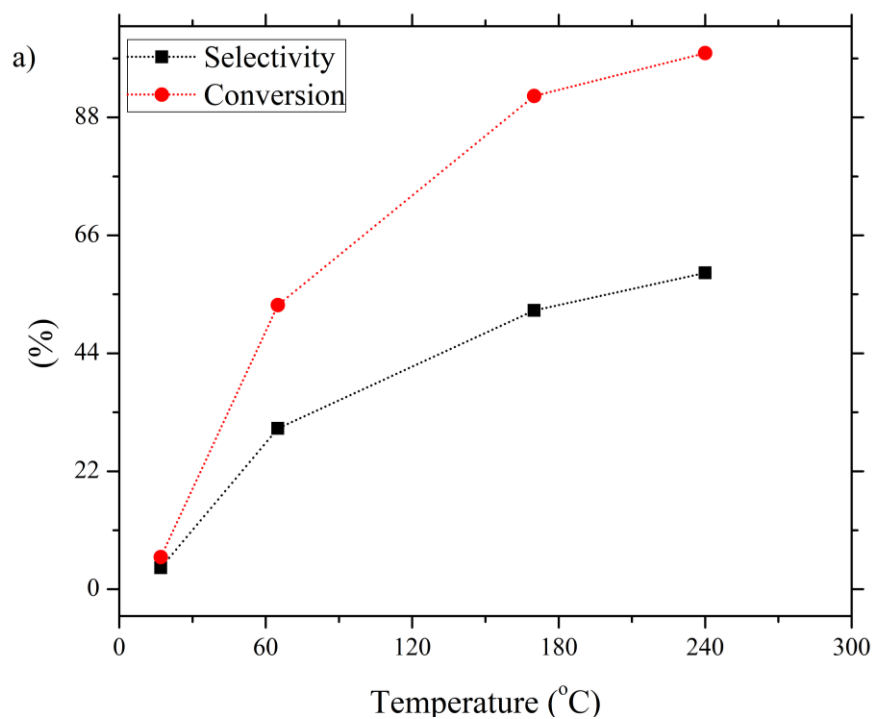
Figure 4.42. a) Conversion and selectivity comparison for 10% b) Change in CO (ppm) and CO_2 (%) concentration after reaction

4.4.4 Oscillatory Kinetics

Oscillatory behavior of rate of CO oxidation on Pt catalyst was first explained in detail by G. Ertl[167]. As explained in his Noble Lecture[168], on Pt (110) catalyst adsorption of CO causes a temporal change on Pt surface which leads to formation of new sites that O_2 dissociative binding is more probable. Hence, CO build-up causes an enhanced O_2 binding that improves CO oxidation rate eventually. When CO and O are consumed during this enhanced period of reaction, they will deplete until new CO layer will again buildup on surface. Overall, this principle leads to periodic oscillatory behavior of reaction where fast and slow reaction domains constantly follow each other.

This type of behavior was observed in this work on 0.5%Pd/TiO$_2$ catalyst at different flow rates: 165, 370 and 490 ml/min. To make CO buildup possible CO concentration in gas mixture was kept high (above 16000 ppm). Respective results at 200°C are given below:
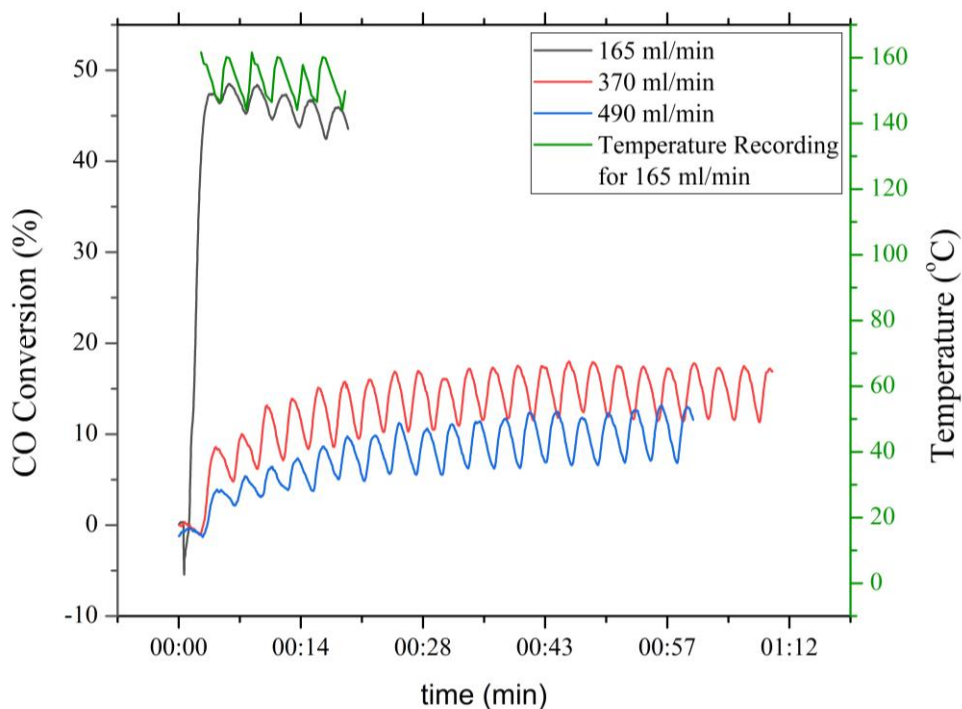
Figure 4.43. Periodic oscillations

84

CO oxidation on 0.1 gram 0.5%Pd/TiO$_2$ is observed to experience periodic oscillations with a period of nearly 3 minutes. For the reaction run under 165 ml/min gas flow rate, temperature changes on heater were also recorded. Heater was set at 200°C and when the temperature detected by the sensor of heater was deviated too much from set point, the heater turns on for 20 seconds and off until deviation is again higher than determined value by manufacturers. Consequently, the temperature induced by heater was also oscillating between 144-162°C. The oscillations were found to be following the change in temperature due to heater's working principle.

The oscillations were only detected when the CO concentration in gas mixture is high enough. It was not possible to detect oscillations when concentration was lower than 13000 ppm due to available CO was not being enough to cover surface such that O$_2$ binding sites required for oscillations are formed.

4.5   Na-Pd/TiO$_2$

4.5.1   TPR Analysis of Na promoted Pd/TiO$_2$

1:1 Na-Pd (1% and 5%)/TiO$_2$ samples were analysed with H$_2$-TPR starting from 200K and reaching 1100K under H$_2$ with 5K/min heating rate and results are given below in comparison to bare Pd/TiO$_2$ samples:
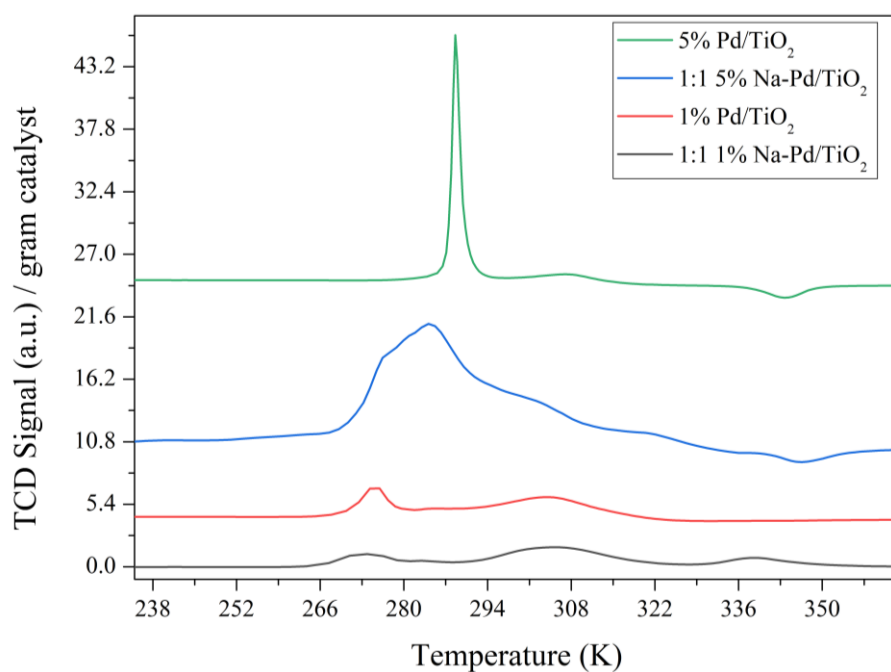
Figure 4.44. 1:1 Na-Pd/TiO$_2$ and Pd/TiO$_2$ H$_2$-TPR profiles

4.5.2　　Na-Pd/TiO$_2$ NMR Results

Na promoted Pd samples was exposed to NMR spectroscopy under 100 or 300 Torr H$_2$ pressure:
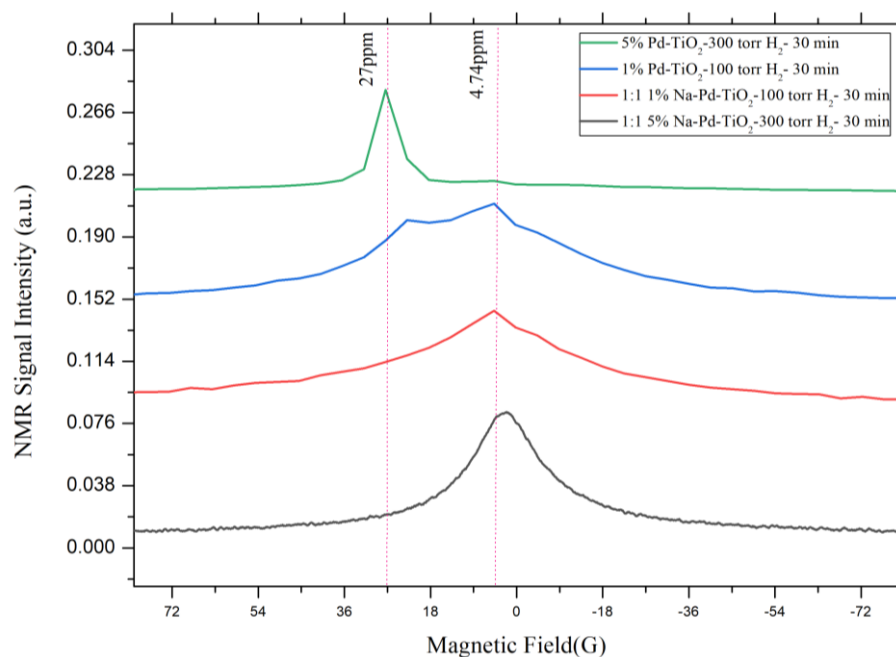
Figure 4.45. Na-Pd/TiO$_2$ and Pd/TiO$_2$ NMR spectra

As seen under the same hydrogen pressure values PdH peaks doesn't appear for Na promoted Pd/TiO$_2$ samples. Similar results were obtained by Uner et al.[169] previously for Na-Cs system where alkali promoter was found to restrict hydrogen mobility and spillover proved by NMR analysis. Although hydrogen mobility decrease was evident by absence of PdH peak, hydroxyl formation is still detected.

CHAPTER 5

CONCLUSIONS

In this work, effect of Pd amount on titania surface on the activity of Pd/TiO$_2$ catalyst for CO oxidation and titania surface reduction were investigated. When Pd used as a reduction promoter, titania surface was found to be reduced under mild-temperature and pressure condition hydrogen treatment. The atomic patch-like Pd structures was found on low Pd loaded titania sample that is responsible for reduction at mild conditions. As Pd content increased 2D structure was lost as well reduction of titania surface. H$_2$ temperature programmed reduction analysis of 0.5, 1, 2, 5 and 10%Pd/TiO$_2$ samples was conducted and quantification of peak was carried out. For each sample a reduction peak related to Pd species appeared around 280K and PdH decomposition peak was observed at 340K. An additional peak around 290K was observed for each sample and found to correspond to titania surface reduction by hydrogen dissociated by Pd. Nearly 70% of titania surface was found to be reduced at 290K for 1%Pd/TiO$_2$ by quantitative TPR studies through hydrogen spillover process. For low Pd loaded samples titania surface reduction at 290K was more significant than high loaded ones which was found to be arise fromo a stronger interaction of metal and support which was possible due to increased interface area at low Pd loadings.

Paramagnetic centers formed upon mild hydrogen treatment was monitored by ESR spectroscopy at room temperature. Oxygen vacancies were only possible to be formed when atomic patches of Pd metal was present on the surface of 0.5%Pd/TiO$_2$. The centers were accesible only in vacuum condition due to regulation of relaxation rate in vacuum proved by saturation recovery experiments. Low-pressure technique was found as an alternate for cryo-temperature technique through regulating the correlation time of fluctuations, consequently spin-lattice relaxation rate.

Hydrogen spillover rate was found to be affected by 2D structure on titania by *operando* NMR studies with quantification and modelling of growth of hydroxyl signal. Two separate spin-lattice relaxation processes were identified for hydroxyl and PdH species where only time constant of PdH was affected by H_2 pressure on the surface. On the other hand, a single spin-spin relaxation process was observed which indicate that the two species are correlated in terms of spin-spin interactions while independent in interaction with lattice.

Advancement in material by nanostructure change was also observed by CO oxidation reaction, as the activity was found to be increased significantly when Pd amount increased in 2D Pd region which was not the case in 3D region.

On the contrary, after high temperature hydrogen treatment, phase change from anatase to rutile was found to be taking place by XRD studies. The phase boundary formed between $Ti_{11}O_{21}$ and TiO_2 was able to adsorb and store hydrogen species at high temperature and desorb upon temperature decrease.

For future work, in order to answer the questions raised by CO oxidation results reported here following experiments are suggested: desorption analysis after reaction needs to be conducted both under dark and UV irradiated conditions to reveal any change in reaction mechanism or CO adsorption behavior, reaction tests without O_2 gas inlet to reactor needs to be carried out to understand whether Pd is capturing oxygen from titania by reverse spillover, reaction should be run with humidity capture at the inlet to eliminate water gas shift reaction pathway, to analyze possible changes in reaction mechanism under dark and illuminated conditions C-NMR or IR studies are suggested, visible light illuminated reactions can also be conducted to reveal any visible light interaction of mild temperature and pressure hydrogen reduced catalysts. On the other hand; TGA and TPO analyses of bulk Pd, bare TiO_2 and low-Pd loaded TiO_2 are suggested to examine oxygen uptake principles of Pd.

REFERENCES

[1]   J.H. Braun, A. Baidins, R.E. Marganski, TiO2 pigment technology: a review, Progress in Organic Coatings. 20 (1992) 105–138. https://doi.org/10.1016/0033-0655(92)80001-d.

[2]   A. Weir, P. Westerhoff, L. Fabricius, K. Hristovski, N. von Goetz, Titanium dioxide nanoparticles in food and personal care products, Environmental Science and Technology. 46 (2012) 2242–2250. https://doi.org/10.1021/es204168d.

[3]   M.J. Hajipour, K.M. Fromm, A. Akbar Ashkarran, D. Jimenez de Aberasturi, I.R. de Larramendi, T. Rojo, V. Serpooshan, W.J. Parak, M. Mahmoudi, Antibacterial properties of nanoparticles, Trends in Biotechnology. 30 (2012) 499–511. https://doi.org/10.1016/j.tibtech.2012.06.004.

[4]   D.R. Miller, S.A. Akbar, P.A. Morris, Nanoscale metal oxide-based heterojunctions for gas sensing: A review, Sensors and Actuators B: Chemical. 204 (2014) 250–272. https://doi.org/10.1016/j.snb.2014.07.074.

[5]   G.F. Fine, L.M. Cavanagh, A. Afonja, R. Binions, Metal Oxide Semi-Conductor Gas Sensors in Environmental Monitoring, Sensors. 10 (2010) 5469–5502. https://doi.org/10.3390/s100605469.

[6]   U. Bach, D. Lupo, P. Comte, J.E. Moser, F. Weissörtel, J. Salbeck, H. Spreitzer, M. Grätzel, Solid-state dye-sensitized mesoporous TiO2 solar cells with high photon-to-electron conversion efficiencies, Nature. 395 (1998) 583–585. https://doi.org/10.1038/26936.

[7]   B. O'Regan, M. Grätzel, A low-cost, high-efficiency solar cell based on dye-sensitized colloidal TiO2 films, Nature. 353 (1991) 737–740. https://doi.org/10.1038/353737a0.

[8]   F. Croce, G.B. Appetecchi, L. Persi, B. Scrosati, Nanocomposite polymer electrolytes for lithium batteries, Nature. 394 (1998) 456–458. https://doi.org/10.1038/28818.

[9]   J. Rivera-Utrilla, M. Sánchez-Polo, M.Á. Ferro-García, G. Prados-Joya, R. Ocampo-Pérez, Pharmaceuticals as emerging contaminants and their removal from water. A review, Chemosphere. 93 (2013) 1268–1287. https://doi.org/10.1016/j.chemosphere.2013.07.059.

[10]   X. Chen, S.S. Mao, Titanium dioxide nanomaterials: Synthesis, properties, modifications and applications, Chemical Reviews. 107 (2007) 2891–2959. https://doi.org/10.1021/cr0500535.

[11]   H. Peng, J. Li, S.-S. Li, J.-B. Xia, First-principles study of the electronic structures and magnetic properties of 3d transition metal-doped anatase TiO2, Journal of Physics: Condensed Matter. 20 (2008) 125207. https://doi.org/10.1088/0953-8984/20/12/125207.

[12]   A.L. Linsebigler, G. Lu, J.T. Yates, Photocatalysis on TiO2 Surfaces: Principles, Mechanisms, and Selected Results, Chem. Rev. 95 (1995) 735–758. https://pubs.acs.org/sharingguidelines.

[13]   L. bin Xiong, J.L. Li, B. Yang, Y. Yu, Ti 3+ in the surface of titanium dioxide: generation, properties and photocatalytic application, Journal of Nanomaterials. 2012 (2012). https://doi.org/10.1155/2012/831524.

[14]   A. Bumajdad, M. Madkour, Understanding the superior photocatalytic activity of noble metals modified titania under UV and visible light irradiation, Physical Chemistry Chemical Physics. 16 (2014) 7146–7158. https://doi.org/10.1039/c3cp54411g.

[15]   C. Xie, D. Yan, H. Li, S. Du, W. Chen, Y. Wang, Y. Zou, R. Chen, S. Wang, Defect Chemistry in Heterogeneous Catalysis: Recognition, Understanding, and Utilization, ACS Catalysis. 10 (2020) 11082–11098. https://doi.org/10.1021/acscatal.0c03034.

[16]   D. Glass, E. Cortés, S. Ben-Jaber, T. Brick, W.J. Peveler, C.S. Blackman, C.R. Howle, R. Quesada-Cabrera, I.P. Parkin, S.A. Maier, Dynamics of Photo-Induced Surface Oxygen Vacancies in Metal-Oxide Semiconductors Studied Under Ambient Conditions, Advanced Science. 6 (2019) 1901841. https://doi.org/10.1002/advs.201901841.

[17]   R. Schmitt, A. Nenning, O. Kraynis, R. Korobko, A.I. Frenkel, I. Lubomirsky, S.M. Haile, J.L.M. Rupp, A review of defect structure and chemistry in ceria and its solid solutions, Chemical Society Reviews. 49 (2020) 554–592. https://doi.org/10.1039/C9CS00588A.

[18]   G. Pacchioni, Oxygen Vacancy: The Invisible Agent on Oxide Surfaces, ChemPhysChem. 4 (2003) 1041–1047. https://doi.org/10.1002/cphc.200300835.

[19]   C. Renz, Lichtreaktionen der Oxyde des Titans, Cers und der Erdsäuren, Helvetica Chimica Acta. 4 (1921) 961–968. https://doi.org/10.1002/hlca.192100401101.

[20]   A. Fujishima, K. Honda, Electrochemical Evidence for the Mechanism of the Primary Stage of Photosynthesis, Bull Chem Soc Jpn. 44 (1971) 1148–1150. https://doi.org/10.1246/bcsj.44.1148.

[21]   N. Bityurin, L. Znaidi, A. Kanaev, Laser-induced absorption in titanium oxide based gels, Chemical Physics Letters. 374 (2003) 95–99. https://doi.org/10.1016/S0009-2614(03)00612-2.

[22]   F. Zuo, L. Wang, T. Wu, Z. Zhang, D. Borchardt, P. Feng, Self-Doped Ti3+ Enhanced Photocatalyst for Hydrogen Production under Visible Light, J Am Chem Soc. 132 (2010) 11856–11857. https://doi.org/10.1021/ja103843d.

[23]   L. Xiong, M. Ouyang, L. Yan, J. Li, M. Qiu, Y. Yu, Visible-light Energy Storage by Ti3+ in TiO2/Cu2O Bilayer Film, Chemistry Letters. 38 (2009) 1154–1155. https://doi.org/10.1246/cl.2009.1154.

[24] X. Pan, M.Q. Yang, X. Fu, N. Zhang, Y.J. Xu, Defective TiO2 with oxygen
      vacancies: Synthesis, properties and photocatalytic applications, Nanoscale.
      5 (2013) 3601–3614. https://doi.org/10.1039/c3nr00476g.

[25] G. Wang, H. Wang, Y. Ling, Y. Tang, X. Yang, R.C. Fitzmorris, C. Wang,
      J.Z. Zhang, Y. Li, Hydrogen-Treated TiO2 Nanowire Arrays for
      Photoelectrochemical Water Splitting, Nano Letters. 11 (2011) 3026–3033.
      https://doi.org/10.1021/nl201766h.

[26] L. Jing, B. Xin, F. Yuan, L. Xue, B. Wang, H. Fu, Effects of Surface
      Oxygen Vacancies on Photophysical and Photochemical Processes of Zn-
      Doped TiO2 Nanoparticles and Their Relationships, The Journal of Physical
      Chemistry B. 110 (2006) 17860–17865. https://doi.org/10.1021/jp063148z.

[27] D.-R. Park, J. Zhang, K. Ikeue, H. Yamashita, M. Anpo, Photocatalytic
      Oxidation of Ethylene to CO2 and H2O on Ultrafine Powdered TiO2
      Photocatalysts in the Presence of O2 and H2O, Journal of Catalysis. 185
      (1999) 114–119. https://doi.org/10.1006/jcat.1999.2472.

[28] T.L. Thompson, J.T. Yates, TiO2-based photocatalysis: Surface defects,
      oxygen and charge transfer, Topics in Catalysis. 35 (2005) 197–210.
      https://doi.org/10.1007/s11244-005-3825-1.

[29] X. Pan, Y.J. Xu, Defect-mediated growth of noble-metal (Ag, Pt, and Pd)
      nanoparticles on TiO2 with oxygen vacancies for photocatalytic redox
      reactions under visible light, Journal of Physical Chemistry C. 117 (2013)
      17996–18005. https://doi.org/10.1021/jp4064802.

[30] G. Wang, H. Wang, Y. Ling, Y. Tang, X. Yang, et al., Hydrogen-treated
      TiO2 nanowire arrays for photoelectrochemical water splitting, Nano
      Letters. 11 (2011) 3026–3033. https://doi.org/10.1021/nl201766h.

[31] H. Liu, H.T. Ma, X.Z. Li, W.Z. Li, M. Wu, X.H. Bao, The enhancement of
      TiO2 photocatalytic activity by hydrogen thermal treatment, Chemosphere.
      50 (2003) 39–46. https://doi.org/10.1016/S0045-6535(02)00486-1.

[32] U. Diebold, J. Lehman, T. Mahmoud, M. Kuhn, G. Leonardelli, et al., Intrinsic defects on a TiO2(110)(1×1) surface and their reaction with oxygen: a scanning tunneling microscopy study, Surface Science. 411 (1998) 137–153. https://doi.org/10.1016/S0039-6028(98)00356-2.

[33] F. Guillemot, M.C. Porté, C. Labrugère, C. Baquey, Ti4+ to Ti3+ conversion of TiO2 uppermost layer by low-temperature vacuum annealing: interest for titanium biomedical applications, Journal of Colloid and Interface Science. 255 (2002) 75–78. https://doi.org/10.1006/jcis.2002.8623.

[34] L.-Q. Wang, D.R. Baer, M.H. Engelhard, A.N. Shultz, The adsorption of liquid and vapor water on TiO2(110) surfaces: the role of defects, Surface Science. 344 (1995) 237–250. https://doi.org/10.1016/0039-6028(95)00859-4.

[35] J. Jun, M. Dhayal, J.-H. Shin, J.-C. Kim, N. Getoff, Surface properties and photoactivity of TiO2 treated with electron beam, Radiation Physics and Chemistry. 75 (2006) 583–589. https://doi.org/10.1016/j.radphyschem.2005.10.015.

[36] J.D. Zhang, S. Fung, L. Li-Bin, L. Zhi-Jun, Ti ion valence variation induced by ionizing radiation at TiO2/Si interface, Surface and Coatings Technology. 158–159 (2002) 238–241. https://doi.org/10.1016/S0257-8972(02)00218-9.

[37] X. Chen, L. Liu, P.Y. Yu, S.S. Mao, Increasing Solar Absorption for Photocatalysis with Black Hydrogenated Titanium Dioxide Nanocrystals, Science (1979). 331 (2011) 746–750. https://doi.org/10.1126/science.1200448.

[38] K. Zhang, W. Zhou, X. Zhang, B. Sun, L. Wang, K. Pan, B. Jiang, G. Tian, H. Fu, Self-floating amphiphilic black TiO2 foams with 3D macro-mesoporous architectures as efficient solar-driven photocatalysts, Applied Catalysis B: Environmental. 206 (2017) 336–343. https://doi.org/10.1016/J.APCATB.2017.01.059.

[39] J. Zheng, S. Bao, X. Zhang, H. Wu, R. Chen, P. Jin, Pd–MgNix nanospheres/black-TiO2 porous films with highly efficient hydrogen production by near-complete suppression of surface recombination, Applied Catalysis B: Environmental. 183 (2016) 69–74. https://doi.org/10.1016/J.APCATB.2015.10.031.

[40] N. Liu, C. Schneider, D. Freitag, M. Hartmann, U. Venkatesan, J. Müller, E. Spiecker, P. Schmuki, Black TiO2 Nanotubes: Cocatalyst-Free Open-Circuit Hydrogen Generation, Nano Letters. 14 (2014) 3309–3313. https://doi.org/10.1021/nl500710j.

[41] X. Chen, L. Liu, Z. Liu, M.A. Marcus, W.-C. Wang, N.A. Oyler, M.E. Grass, B. Mao, P.-A. Glans, P.Y. Yu, J. Guo, S.S. Mao, Properties of Disorder-Engineered Black Titanium Dioxide Nanoparticles through Hydrogenation, Scientific Reports. 3 (2013) 1510. https://doi.org/10.1038/srep01510.

[42] H. Lu, B. Zhao, R. Pan, J. Yao, J. Qiu, L. Luo, Y. Liu, Safe and facile hydrogenation of commercial Degussa P25 at room temperature with enhanced photocatalytic activity, RSC Adv. 4 (2014) 1128–1132. https://doi.org/10.1039/C3RA44493G.

[43] A. Naldoni, M. Allieta, S. Santangelo, M. Marelli, F. Fabbri, S. Cappelli, C.L. Bianchi, R. Psaro, V. Dal Santo, Effect of Nature and Location of Defects on Bandgap Narrowing in Black TiO 2 Nanoparticles, J Am Chem Soc. 134 (2012) 7600–7603. https://doi.org/10.1021/ja3012676.

[44] F. Teng, M. Li, C. Gao, G. Zhang, P. Zhang, Y. Wang, L. Chen, E. Xie, Preparation of black TiO2 by hydrogen plasma assisted chemical vapor deposition and its photocatalytic activity, Applied Catalysis B: Environmental. 148–149 (2014) 339–343. https://doi.org/10.1016/J.APCATB.2013.11.015.

[45] Z. Wang, C. Yang, T. Lin, H. Yin, P. Chen, D. Wan, F. Xu, F. Huang, J. Lin, X. Xie, M. Jiang, H-Doped Black Titania with Very High Solar Absorption and Excellent Photocatalysis Enhanced by Localized Surface Plasmon Resonance, Advanced Functional Materials. 23 (2013) 5444–5450. https://doi.org/10.1002/adfm.201300486.

[46] H. Yin, T. Lin, C. Yang, Z. Wang, G. Zhu, T. Xu, X. Xie, F. Huang, M. Jiang, Gray TiO2 Nanowires Synthesized by Aluminum-Mediated Reduction and Their Excellent Photocatalytic Activity for Water Cleaning, Chemistry - A European Journal. 19 (2013) 13313–13316. https://doi.org/10.1002/chem.201302286.

[47] Z. Zhang, M.N. Hedhili, H. Zhu, P. Wang, Electrochemical reduction induced self-doping of Ti3+ for efficient water splitting performance on TiO2 based photoelectrodes, Physical Chemistry Chemical Physics. 15 (2013) 15637. https://doi.org/10.1039/c3cp52759j.

[48] C. Xu, Y. Song, L. Lu, C. Cheng, D. Liu, X. Fang, X. Chen, X. Zhu, D. Li, Electrochemically hydrogenated TiO2 nanotubes with improved photoelectrochemical water splitting performance, Nanoscale Research Letters. 8 (2013) 391. https://doi.org/10.1186/1556-276X-8-391.

[49] Y. Xu, C. Zhang, L. Zhang, X. Zhang, H. Yao, et al., Pd-catalyzed instant hydrogenation of TiO2 with enhanced photocatalytic performance, Energy and Environmental Science. 9 (2016) 2410–2417. https://doi.org/10.1039/c6ee00830e.

[50] Y. Fan, X. Feng, W. Zhou, S. Murakami, K. Kikuchi, N. Nomura, L. Wang, W. Jiang, A. Kawasaki, Preparation of monophasic titanium sub-oxides of Magnéli phase with enhanced thermoelectric performance, J Eur Ceram Soc. 38 (2018) 507–513. https://doi.org/10.1016/j.jeurceramsoc.2017.09.040.

[51] J.F. Houlihan, L.N. Mulay, J.P. Houlimn1, Electronic Properties and Defect Structure of Ti,O, : Correlation of Magnetic Susceptibility, Electrical

Conductivity, and Structural Parameters via EPR Spectroscopy, Phys. Stat. Sol. (b). 61 (1974).

[52]   I.N. Martyanov, T. Berger, O. Diwald, S. Rodrigues, K.J. Klabunde, Enhancement of TiO2 visible light photoactivity through accumulation of defects during reduction-oxidation treatment, Journal of Photochemistry and Photobiology A: Chemistry. 212 (2010) 135–141. https://doi.org/10.1016/j.jphotochem.2010.04.006.

[53]   F.C. Walsh, R.G.A. Wills, The continuing development of Magnéli phase titanium sub-oxides and Ebonex® electrodes, Electrochimica Acta. 55 (2010) 6342–6351. https://doi.org/10.1016/j.electacta.2010.05.011.

[54]   R.J. Pollock, J.F. Houlihan, A.N. Bain, B.S. Coryea, Electrochemical properties of a new electrode material, Ti4O7, Materials Research Bulletin. 19 (1984). https://doi.org/10.1016/0025-5408(84)90005-9.

[55]   L.K. Keys, L.N. Mulay, Magnetic-Susceptibility Studies on the Magnéli Phases of the Titanium-Oxygen System, Journal of Applied Physics. 38 (1967). https://doi.org/10.1063/1.1709670.

[56]   R.R. Miller-Folk, R.E. Noftle, D. Pletcher, Electron transfer reactions at Ebonex ceramic electrodes, Journal of Electroanalytical Chemistry and Interfacial Electrochemistry. 274 (1989). https://doi.org/10.1016/0022-0728(89)87047-0.

[57]   J.R. Smith, F.C. Walsh, R.L. Clarke, Electrodes based on Magneli phase titanium oxides: the properties and applications of Ebonex materials, Journal of Applied Electrochemistry. 28 (1998) 1021–1033. https://doi.org/https://doi.org/10.1023/A:1003469427858.

[58]   Lj.M. Vračar, N.V. Krstajić, V.R. Radmilović, M.M. Jakšić, Electrocatalysis by nanoparticles – oxygen reduction on Ebonex/Pt electrode, Journal of Electroanalytical Chemistry. 587 (2006) 99–107. https://doi.org/10.1016/j.jelechem.2005.10.021.

[59] R. Alipour Moghadam Esfahani, A.H.A. Monteverde Videla, S. Vankova, S. Specchia, Stable and methanol tolerant Pt/TiOx-C electrocatalysts for the oxygen reduction reaction, International Journal of Hydrogen Energy. 40 (2015) 14529–14539. https://doi.org/10.1016/j.ijhydene.2015.05.131.

[60] B.H. Lee, J. Coughlin, G. Kim, G.C. Bazan, K. Lee, Efficient solution-processed small-molecule solar cells with titanium suboxide as an electric adhesive layer, Applied Physics Letters. 104 (2014) 213305. https://doi.org/10.1063/1.4880095.

[61] E. Verrelli, D. Tsoukalas, Cluster beam synthesis of metal and metal-oxide nanoparticles for emerging memories, Solid-State Electronics. 101 (2014) 95–105. https://doi.org/10.1016/j.sse.2014.06.017.

[62] E.E. Farndon, D. Pletcher, Studies of platinized Ebonex® electrodes, Electrochimica Acta. 42 (1997) 1281–1285. https://doi.org/10.1016/S0013-4686(96)00299-X.

[63] H. Okamoto, O-Ti (Oxygen-Titanium), Journal of Phase Equilibria and Diffusion. 32 (2011) 473–474. https://doi.org/10.1007/s11669-011-9935-5.

[64] C.M. Ghimbeu, C. Zlotea, R. Gadiou, F. Cuevas, E. Leroy, M. Latroche, C. Vix-Guterl, Understanding the mechanism of hydrogen uptake at low pressure in carbon/palladium nanostructured composites, Journal of Materials Chemistry. 21 (2011) 17765–17775. https://doi.org/10.1039/c1jm12939b.

[65] N.M. Martin, M. Van Den Bossche, H. Grönbeck, C. Hakanoglu, J. Gustafson, S. Blomberg, M.A. Arman, A. Antony, R. Rai, A. Asthagiri, J.F. Weaver, E. Lundgren, Dissociative adsorption of hydrogen on PdO(101) studied by HRCLS and DFT, Journal of Physical Chemistry C. 117 (2013) 13510–13519. https://doi.org/10.1021/jp4036698.

[66] L.F. Chen, J.A. Wang, M.A. Valenzuela, X. Bokhimi, D.R. Acosta, O. Novaro, Hydrogen spillover and structural defects in a PdO/zirconia

nanophase synthesized through a surfactant-templated route, Journal of Alloys and Compounds. 417 (2006) 220–223. https://doi.org/10.1016/j.jallcom.2005.08.070.

[67] C.W. Chou, S.J. Chu, H.J. Chiang, C.Y. Huang, C.J. Lee, S.R. Sheen, T.P. Perng, C.T. Yeh, Temperature-programmed reduction study on calcination of nano-palladium, Journal of Physical Chemistry B. 105 (2001) 9113–9117. https://doi.org/10.1021/jp011170g.

[68] Y.T. Lee, J.M. Lee, Y.J. Kim, J.H. Joe, W. Lee, Hydrogen gas sensing properties of PdO thin films with nano-sized cracks, Nanotechnology. 21 (2010). https://doi.org/10.1088/0957-4484/21/16/165503.

[69] W. Lin, Y.X. Zhu, N.Z. Wu, Y.C. Xie, I. Murwani, E. Kemnitz, Total oxidation of methane at low temperature over Pd/TiO2/Al2O3: effects of the support and residual chlorine ions, Applied Catalysis B: Environmental. 50 (2004) 59–66. https://doi.org/10.1016/J.APCATB.2004.03.009.

[70] U.S. Ozkan, M.W. Kumthekar, G. Karakas, Characterization and temperature-programmed studies over Pd/TiO2 catalysts for NO reduction with methane, Catalysis Today. 40 (1998) 3–14. https://doi.org/10.1016/S0920-5861(97)00112-0.

[71] C. Zhang, Y. Li, Y. Wang, H. He, Sodium-Promoted Pd/TiO2 for Catalytic Oxidation of Formaldehyde at Ambient Temperature, Environmental Science & Technology. 48 (2014) 5816–5822. https://doi.org/10.1021/es4056627.

[72] W.J. Shen, M. Okumura, Y. Matsumura, M. Haruta, The influence of the support on the activity and selectivity of Pd in CO hydrogenation, Applied Catalysis A: General. 213 (2001) 225–232. https://doi.org/10.1016/S0926-860X(01)00465-3.

[73] H. Huang, X. Ye, H. Huang, L. Zhang, D.Y.C. Leung, Mechanistic study on formaldehyde removal over Pd/TiO2 catalysts: Oxygen transfer and role of

water vapor, Chemical Engineering Journal. 230 (2013) 73–79. https://doi.org/10.1016/j.cej.2013.06.035.

[74]   M. Che, C.O. Bennett, The Influence of Particle Size on the Catalytic Properties of Supported Metals, in: D.D. Eley, H. Pines, P.B. Weisz (Eds.), Advances in Catalysis, 1989: pp. 55–172. https://doi.org/10.1016/S0360-0564(08)60017-6.

[75]   G.R. Bamwenda, S. Tsubota, T. Nakamura, M. Haruta, The influence of the preparation methods on the catalytic activity of platinum and gold supported on TiO2 for CO oxidation, Catalysis Letters. 44 (1997) 83–87. https://doi.org/10.1023/A:1018925008633.

[76]   M. Haruta, S. Tsubota, T. Kobayashi, H. Kageyama, M.J. Genet, B. Delmon, Low-Temperature Oxidation of CO over Gold Supported on TiO2, α-Fe2O3, and Co3O4, Journal of Catalysis. 144 (1993). https://doi.org/10.1006/jcat.1993.1322.

[77]   L.S. Al-Mazroai, M. Bowker, P. Davies, A. Dickinson, J. Greaves, D. James, L. Millard, The photocatalytic reforming of methanol, Catalysis Today. 122 (2007) 46–50. https://doi.org/10.1016/J.CATTOD.2007.01.022.

[78]   C. Li, L. Zong, Q. Li, J. Zhang, J. Yang, Z. Jin, Photocatalytic Oxidation of Propylene on Pd-Loaded Anatase TiO2 Nanotubes Under Visible Light Irradiation, Nanoscale Research Letters. 11 (2016). https://doi.org/10.1186/s11671-016-1486-6.

[79]   C. Wang, Y. Li, C. Zhang, X. Chen, C. Liu, W. Weng, W. Shan, H. He, A simple strategy to improve Pd dispersion and enhance Pd/TiO2 catalytic activity for formaldehyde oxidation: The roles of surface defects, Applied Catalysis B: Environmental. 282 (2021) 119540. https://doi.org/10.1016/J.APCATB.2020.119540.

[80]   K.S. Novoselov, D. Jiang, F. Schedin, T.J. Booth, V. v. Khotkevich, S. v. Morozov, A.K. Geim, Two-dimensional atomic crystals, Proceedings of the

National Academy of Sciences. 102 (2005) 10451–10453. https://doi.org/10.1073/PNAS.0502848102.

[81]   R. Mas-Ballesté, C. Gómez-Navarro, J. Gómez-Herrero, F. Zamora, 2D materials: To graphene and beyond, Nanoscale. 3 (2011) 20–30. https://doi.org/10.1039/c0nr00323a.

[82]   X. Huang, C. Tan, Z. Yin, H. Zhang, 25th anniversary article: Hybrid nanostructures based on two-dimensional nanomaterials, Advanced Materials. 26 (2014) 2185–2204. https://doi.org/10.1002/adma.201304964.

[83]   S. Khoobiar, Particle to Particle Migration of Hydrogen Atoms on Platinum—Alumina Catalysts from Particle to Neighboring Particles, The Journal of Physical Chemistry. 68 (1964). https://doi.org/10.1021/j100784a503.

[84]   R. Prins, Hydrogen spillover. Facts and fiction, Chemical Reviews. 112 (2012) 2714–2738. https://doi.org/10.1021/cr200346z.

[85]   S.K. Beaumont, S. Alayoglu, C. Specht, N. Kruse, G.A. Somorjai, A nanoscale demonstration of hydrogen atom spillover and surface diffusion across silica using the kinetics of CO2 methanation catalyzed on spatially separate Pt and Co nanoparticles, Nano Letters. 14 (2014) 4792–4796. https://doi.org/10.1021/nl501969k.

[86]   W. Karim, C. Spreafico, A. Kleibert, J. Gobrecht, J. Vandevondele, Y. Ekinci, J.A. van Bokhoven, Catalyst support effects on hydrogen spillover, Nature. 541 (2017) 68–71. https://doi.org/10.1038/nature20782.

[87]   W.C. Conner, J.L. Falconer, Spillover in heterogeneous catalysis, Chem. Rev. 95 (1995) 759–788. https://doi.org/10.1021/cr00035a014.

[88]   J.M. Cíes, J.J. Delgado, M. López-Haro, R. Pilasombat, J.A. Pérez-Omil, S. Trasobares, S. Bernal, J.J. Calvino, Contributions of electron microscopy to understanding CO adsorption on powder Au/ceria-zirconia catalysts,

Chemistry - A European Journal. 16 (2010) 9536–9543.
https://doi.org/10.1002/chem.201000866.

[89]   Y.Y. Wu, N.A. Mashayekhi, H.H. Kung, Au-metal oxide support interface
        as catalytic active sites, Catalysis Science and Technology. 3 (2013) 2881–
        2891. https://doi.org/10.1039/c3cy00243h.

[90]   V.V. Gorodetskii, A.A. Sametova, A.V. Matveev, V.M. Tapilin, From single
        crystals to supported nanoparticles in experimental and theoretical studies of
        H2 oxidation over platinum metals (Pt, Pd): Intermediates, surface waves
        and spillover, Catalysis Today. 144 (2009).
        https://doi.org/10.1016/j.cattod.2008.12.014.

[91]   F. Faccin, F.F. Guedes, E.V. Benvenutti, C.C. Moro, A FTIR study of the
        metal-support interactions and hydrogen spillover on Pd/TiO2 and Ni/TiO2,
        Eclética Química. 27 (2002). https://doi.org/10.1590/S0100-
        46702002000100008.

[92]   H. Lin, The study of oxygen spillover and back spillover on Pt/TiO2 by a
        potential dynamic sweep method, Journal of Molecular Catalysis A:
        Chemical. 144 (1999) 189–197. https://doi.org/10.1016/S1381-
        1169(98)00381-1.

[93]   D.C. Grinter, C. Muryn, A. Sala, C.M. Yim, C.L. Pang, T.O. Menteş, A.
        Locatelli, G. Thornton, Spillover Reoxidation of Ceria Nanoparticles,
        Journal of Physical Chemistry C. 120 (2016) 11037–11044.
        https://doi.org/10.1021/acs.jpcc.6b03670.

[94]   D. Kaya, D. Singh, S. Kincal, D. Uner, Facilitating role of Pd for hydrogen,
        oxygen and water adsorption/desorption processes from bulk CeO2 and
        CeO2/γ-Al2O3, Catalysis Today. 323 (2019) 141–147.
        https://doi.org/10.1016/j.cattod.2018.04.063.

[95]   S.Y. Christou, A.M. Efstathiou, Effects of Pd particle size on the rates of
        oxygen back-spillover and CO oxidation under dynamic oxygen storage and

release measurements over Pd/CeO2 catalysts, in: Topics in Catalysis, 2007: pp. 351–355. https://doi.org/10.1007/s11244-007-0204-0.

[96] A. Lund, M. Shiotani, S. Shimada, Principles and Applications of ESR Spectroscopy, 1st ed., Springer, Dordrecht, 2010.

[97] D. Goldfarb, S. Stoll, EPR Spectroscopy Fundamentals and Methods, 1st ed., Wiley, 2018.

[98] J.A. Weil, J.R. Bolton, Electron Paramagnetic Resonance, John Wiley & Sons, Inc., Hoboken, NJ, USA, 2006. https://doi.org/10.1002/0470084987.

[99] M. L. Sehgal, K. N. Kaul, M. Javed, Calculation of ESR Spin- Spin Relaxation Times (1/T_2) Transition Metal Ion Complexes: A DFT Application, Oriental Journal of Chemistry. 33 (2017). https://doi.org/10.13005/ojc/330115.

[100] S.A. Dikanov, A.R. Crofts, Electron paramagnetic resonance spectroscopy, in: D.R. Vij (Ed.), Handbook of Applied Solid State Spectroscopy, 1st ed., Springer US, Boston, MA, 2006: pp. 97–149. https://doi.org/10.1007/0-387-37590-2_3.

[101] S.S. Eaton, G.R. Eaton, Saturation recovery EPR, in: S.S. Eaton, G.R. Eaton, L.J. Berliner (Eds.), Biomedical EPR, Part B: Methodology, Instrumentation, and Dynamics, 1st ed., Kluwer Academic Publishers-Plenum Publishers, New York, 2005: pp. 3–18. https://doi.org/10.1007/0-306-48533-8_1.

[102] M.H. Levitt, Spin Dynamics Basics of Nuclear Magnetic Resonance Second edition, Chichester: John Wiley & Sons, 2008.

[103] Y. Zhou, Z. Wang, C. Liu, Perspective on CO oxidation over Pd-based catalysts, Catalysis Science and Technology. 5 (2015) 69–81. https://doi.org/10.1039/c4cy00983e.

[104] L. Meng, A.-P. Jia, J.-Q. Lu, L.-F. Luo, W.-X. Huang, M.-F. Luo, Synergetic Effects of PdO Species on CO Oxidation over PdO–CeO2 Catalysts, The Journal of Physical Chemistry C. 115 (2011) 19789–19796. https://doi.org/10.1021/jp2056688.

[105] Y. Xu, J. Ma, Y. Xu, H. Li, H. Li, P. Li, X. Zhou, CO oxidation over Pd catalysts supported on different supports: A consideration of oxygen storage capacity of catalyst, in: Advanced Materials Research, 2012: pp. 3298–3301. https://doi.org/10.4028/www.scientific.net/AMR.347-353.3298.

[106] V. Bratan, C. Munteanu, C. Hornoiu, A. Vasile, F. Papa, R. State, S. Preda, D. Culita, N.I. Ionescu, CO oxidation over Pd supported catalysts —In situ study of the electric and catalytic properties, Applied Catalysis B: Environmental. 207 (2017) 166–173. https://doi.org/10.1016/j.apcatb.2017.02.017.

[107] S.F. Chen, J.P. Li, K. Qian, W.P. Xu, Y. Lu, W.X. Huang, S.H. Yu, Large scale photochemical synthesis of M@TiO2 nanocomposites (M = Ag, Pd, Au, Pt) and their optical properties, CO oxidation performance, and antibacterial effect, Nano Research. 3 (2010) 244–255. https://doi.org/10.1007/s12274-010-1027-z.

[108] N.S. Kolobov, D.S. Selishchev, A.V. Bukhtiyarov, A.I. Gubanov, D.V. Kozlov, UV-LED Photocatalytic Oxidation of CO over the Pd/TiO2 Catalysts Synthesized by the Decomposition of Pd(acac)2, Materials Today: Proceedings. 4 (2017) 11356–11359. https://doi.org/10.1016/j.matpr.2017.09.008.

[109] D.S. Selishchev, N.S. Kolobov, A. v. Bukhtiyarov, E.Y. Gerasimov, A.I. Gubanov, D. v. Kozlov, Deposition of Pd nanoparticles on TiO2 using a Pd(acac)2 precursor for photocatalytic oxidation of CO under UV-LED irradiation, Applied Catalysis B: Environmental. 235 (2018) 214–224. https://doi.org/10.1016/j.apcatb.2018.04.074.

[110] Z. Wang, B. Li, M. Chen, W. Weng, H. Wan, Size and support effects for CO oxidation on supported Pd catalysts, in: Science China Chemistry, 2010: pp. 2047–2056. https://doi.org/10.1007/s11426-010-4109-6.

[111] S. Odabaşi, Effect of Cobalt Doping on Photocatalytic Activity of Lead Titanate, 2018. https://doi.org/[M.S. - Master of Science].

[112] D. Uner, N.A. Tapan, I. Özen, M. Üner, Oxygen adsorption on Pt/TiO2 catalysts, Applied Catalysis A: General. 251 (2003) 225–234. https://doi.org/10.1016/S0926-860X(03)00317-X.

[113] T. Theivasanthi, M. Alagar, Titanium dioxide (TiO2) Nanoparticles XRD Analyses: An Insight, Chemical Physics. (2013).

[114] X. Wei, G. Zhu, J. Fang, J. Chen, Synthesis, characterization, and photocatalysis of well-dispersible phase-pure anatase TiO2 nanoparticles, International Journal of Photoenergy. 2013 (2013). https://doi.org/10.1155/2013/726872.

[115] C. Byrne, R. Fagan, S. Hinder, D.E. Mccormack Cd, S.C. Pillai, New approach of modifying the anatase to rutile transition temperature in TiO2 photocatalysts, RSC Advances. (2016). https://doi.org/10.1039/c6ra19759k.

[116] D.L. Liao, B.Q. Liao, Shape, size and photocatalytic activity control of TiO2 nanoparticles with surfactants, Journal of Photochemistry and Photobiology A: Chemistry. 187 (2007) 363–369. https://doi.org/10.1016/j.jphotochem.2006.11.003.

[117] K.H. Leong, H.Y. Chu, S. Ibrahim, P. Saravanan, Palladium nanoparticles anchored to anatase TiO2 for enhanced surface plasmon resonance-stimulated, visible-light-driven photocatalytic activity, Beilstein Journal of Nanotechnology. 6 (2015) 428–437. https://doi.org/10.3762/bjnano.6.43.

[118] F. Hardcastle, Raman Spectroscopy of Titania (TiO2) Nanotubular Water-Splitting Catalysts, J Ark Acad Sci. 65 (2011) 43–48.

[119] E.J. Ekoi, A. Gowen, R. Dorrepaal, D.P. Dowling, Characterisation of titanium oxide layers using Raman spectroscopy and optical profilometry: Influence of oxide properties, Results in Physics. 12 (2019) 1574–1585. https://doi.org/10.1016/j.rinp.2019.01.054.

[120] F.D. Hardcastle, H. Ishihara, R. Sharma, A.S. Biris, Photoelectroactivity and Raman spectroscopy of anodized titania (TiO 2) photoactive water-splitting catalysts as a function of oxygen-annealing temperature, Journal of Materials Chemistry. (2011). https://doi.org/10.1039/c0jm03106b.

[121] S.A. Abdullah, M.Z. Sahdan, N. Nafarizal, H. Saim, C.H. Cik Rohaida, F. Adriyanto, XRD and Raman spectroscopy study on the effects of post-annealing temperature of TiO2 thin films, 2019 IEEE International Conference on Sensors and Nanotechnology, SENSORS and NANO 2019. (2019) 2019–2022. https://doi.org/10.1109/SENSORSNANO44414.2019.8940092.

[122] S. Yuvaraj, L. Fan-Yuan, C. Tsong-Huei, Y. Chuin-Tih, Thermal Decomposition of Metal Nitrates in Air and Hydrogen Environments, The Journal of Physical Chemistry B. 107 (2003) 1044–1047. https://doi.org/10.1021/jp026961c.

[123] E.A. Cochran, D.-H. Park, M.G. Kast, L.J. Enman, C.K. Perkins, R.H. Mansergh, D.A. Keszler, D.W. Johnson, S.W. Boettcher, Role of Combustion Chemistry in Low-Temperature Deposition of Metal Oxide Thin Films from Solution, Chemistry of Materials. 29 (2017) 9480–9488. https://doi.org/10.1021/acs.chemmater.7b03618.

[124] J. Li, G. Lu, G. Wu, D. Mao, Y. Guo, Y. Wang, Y. Guo, Effect of TiO2 crystal structure on the catalytic performance of Co3O4/TiO2 catalyst for low-temperature CO oxidation, Catalysis Science and Technology. 4 (2014) 1268–1275. https://doi.org/10.1039/c3cy01004j.

[125] H. Zhu, Z. Qin, W. Shan, W. Shen, J. Wang, Pd/CeO2-TiO2 catalyst for CO oxidation at low temperature: A TPR study with H2 and CO as reducing agents, Journal of Catalysis. 225 (2004) 267–277. https://doi.org/10.1016/j.jcat.2004.04.006.

[126] S. Kuhaudomlap, O. Mekasuwandumrong, P. Praserthdam, S.I. Fujita, M. Arai, J. Panpranot, The H2-treated TiO2 supported Pt catalysts prepared by strong electrostatic adsorption for liquid-phase selective hydrogenation, Catalysts. 8 (2018). https://doi.org/10.3390/catal8020087.

[127] J.D. Cox, D.D. Wagman, V.A. Medvedev, CODATA Key Values for Thermodynamics, Hemisphere Publishing Corp., New York. 1. (1984).

[128] L. Glasser, Systematic thermodynamics of Magnéli-phase and other transition metal oxides, Inorganic Chemistry. 48 (2009) 10289–10294. https://doi.org/10.1021/ic901395z.

[129] W. Mao, M. Wilde, S. Ogura, J. Chen, K. Fukutani, H. Matsuzaki, T. Terai, Hydrogen-Accelerated Phase Transition and Diffusion in TiO2 Thin Films, Journal of Physical Chemistry C. 122 (2018) 23026–23033. https://doi.org/10.1021/acs.jpcc.8b06893.

[130] I.M. Low, H. Albetran, V.M. Prida, V. Vega, P. Manurung, M. Ionescu, A comparative study on crystallization behavior, phase stability, and binding energy in pure and Cr-doped TiO $_2$ nanotubes, Journal of Materials Research. 28 (2013) 304–312. https://doi.org/10.1557/jmr.2012.275.

[131] V. Bratan, C. Munteanu, C. Hornoiu, A. Vasile, F. Papa, R. State, S. Preda, D. Culita, N.I. Ionescu, CO oxidation over Pd supported catalysts —In situ study of the electric and catalytic properties, Applied Catalysis B: Environmental. 207 (2017) 166–173. https://doi.org/10.1016/j.apcatb.2017.02.017.

[132] B. Rusinque, S. Escobedo Salas, H. de Lasa, Photoreduction of a Pd-doped mesoporous TiO2 photocatalyst for hydrogen production under visible light, Catalysts. 10 (2020). https://doi.org/10.3390/catal10010074.

[133] J. Girardon, E. Quinet, A. Gribovalconstant, P. Chernavskii, L. Gengembre, A. Khodakov, Cobalt dispersion, reducibility, and surface sites in promoted silica-supported Fischer–Tropsch catalysts, Journal of Catalysis. 248 (2007) 143–157. https://doi.org/10.1016/j.jcat.2007.03.002.

[134] J. Hong, E. Marceau, A.Y. Khodakov, L. Gaberová, A. Griboval-Constant, J.-S. Girardon, C. la Fontaine, V. Briois, Speciation of Ruthenium as a Reduction Promoter of Silica-Supported Co Catalysts: A Time-Resolved in Situ XAS Investigation, ACS Catalysis. 5 (2015) 1273–1282. https://doi.org/10.1021/cs501799p.

[135] S.L. Soled, E. Iglesia, R.A. Fiato, J.E. Baumgartner, H. Vroman, S. Miseo, Control of Metal Dispersion and Structure by Changes in the Solid-State Chemistry of Supported Cobalt Fischer–Tropsch Catalysts, Topics in Catalysis. 26 (2003) 101–109. https://doi.org/10.1023/B:TOCA.0000012990.83630.f9.

[136] G. Jacobs, W. Ma, P. Gao, B. Todic, T. Bhatelia, D.B. Bukur, S. Khalid, B.H. Davis, Fischer-tropsch synthesis: Differences observed in local atomic structure and selectivity with pd compared to typical promoters (Pt, Re, Ru) of Co/Al 2O 3 catalysts, Topics in Catalysis. 55 (2012) 811–817. https://doi.org/10.1007/s11244-012-9856-5.

[137] C.P. Romero, J.I. Avila, R.A. Trabol, H. Wang, A. Vantomme, M.J. van Bael, P. Lievens, A.L. Cabrera, Pd as a promoter to reduce Co cluster films at room temperature, International Journal of Hydrogen Energy. 35 (2010) 2262–2267. https://doi.org/10.1016/j.ijhydene.2010.01.026.

[138] Y. Chen, Y. Wang, W. Li, Q. Yang, Q. Hou, L. Wei, L. Liu, F. Huang, M. Ju, Enhancement of photocatalytic performance with the use of noble-metal-

decorated TiO2 nanocrystals as highly active catalysts for aerobic oxidation under visible-light irradiation, Applied Catalysis B: Environmental. 210 (2017) 352–367. https://doi.org/10.1016/j.apcatb.2017.03.077.

[139] W. Liang, X. Du, Y. Zhu, S. Ren, J. Li, Catalytic oxidation of chlorobenzene over Pd-TiO2 /Pd-Ce/TiO2 catalysts, Catalysts. 10 (2020). https://doi.org/10.3390/catal10030347.

[140] Y. Fan, J. Bao, L. Shi, S. Li, Y. Lu, H. Liu, H. Wang, L. Zhong, Y. Sun, Photocatalytic Coupling of Methanol and Formaldehyde into Ethylene Glycol with High Atomic Efficiency, Catalysis Letters. 148 (2018) 2274– 2282. https://doi.org/10.1007/s10562-018-2465-6.

[141] K.H. Leong, H.Y. Chu, S. Ibrahim, P. Saravanan, Palladium nanoparticles anchored to anatase TiO2 for enhanced surface plasmon resonance-stimulated, visible-light-driven photocatalytic activity, Beilstein Journal of Nanotechnology. 6 (2015) 428–437. https://doi.org/10.3762/bjnano.6.43.

[142] K. Thamaphat, P. Limsuwan, B. Ngotaworndhai, Phase Characterization of TiO 2 Powder by XRD and TEM, Materials Science. 42 (2008) 357–361.

[143] Z. Cui, X. Bai, Ultrasonic-assisted synthesis of two dimensional coral-like Pd nanosheets supported on reduced graphene oxide for enhanced electrocatalytic performance, Ultrasonics Sonochemistry. 70 (2021) 105309. https://doi.org/10.1016/J.ULTSONCH.2020.105309.

[144] J. Jiang, W. Ding, W. Li, Z. Wei, Freestanding single-atom-layer Pd-based catalysts: oriented splitting of energy bands for unique stability and activity, Chem. 6 (2020) 431–447. https://doi.org/10.1016/j.chempr.2019.11.003.

[145] K.A. Fichthorn, Principles of Adsorption and Reaction on Solid Surfaces. Richard I. Masel, Journal of Catalysis. 170 (1997) 214–215. https://doi.org/10.1006/jcat.1997.1791.

[146] P. Liu, Y. Zhao, R. Qin, S. Mo, G. Chen, L. Gu, D.M. Chevrier, P. Zhang, Q. Guo, D. Zang, B. Wu, G. Fu, N. Zheng, Photochemical route for synthesizing atomically dispersed palladium catalysts, Science (1979). 352 (2016) 797–800. https://doi.org/10.1126/science.aaf5251.

[147] R.C. Roca, I. Kamiya, Change in Topography of InAs Submonolayer Nanostructures at the 2D to 3D Transition, Physica Status Solidi (b). 258 (2021) 2000349. https://doi.org/10.1002/pssb.202000349.

[148] R. Liang, A. Hu, J. Persic, Y. Norman Zhou, Palladium nanoparticles loaded on carbon modified TiO2 nanobelts for enhanced methanol electrooxidation, Nano-Micro Letters. 5 (2013) 202–212. https://doi.org/10.5101/nml.v5i3.p202-212.

[149] C. Alegre, E. Modica, C. Lo Vecchio, S. Siracusano, A.S. Aricò, V. Baglio, Pd supported on Ti-suboxides as bifunctional catalyst for air electrodes of metal-air batteries, International Journal of Hydrogen Energy. 41 (2016) 19579–19586. https://doi.org/10.1016/j.ijhydene.2016.03.095.

[150] C. Lo Vecchio, C. Alegre, D. Sebastián, A. Stassi, A.S. Aricò, V. Baglio, Investigation of supported Pd-based electrocatalysts for the oxygen reduction reaction: Performance, Materials. 8 (2015) 7997–8008. https://doi.org/10.3390/ma8125438.

[151] J. Strunk, W.C. Vining, A.T. Bell, A study of oxygen vacancy formation and annihilation in submonolayer coverages of TiO2 dispersed on MCM-48, The Journal of Physical Chemistry C. 114 (2010) 16937–16945. https://doi.org/10.1021/jp100104d.

[152] J.M. Cho, W.J. Yun, J.-K. Lee, H.S. Lee, W.W. So, et al., Electron spin resonance from annealed titania nanotubes, Applied Physics A. 88 (2007) 751–755. https://doi.org/10.1007/s00339-007-4063-0.

111

[153] T. Sekiya, H. Takeda, N. Kamiya, S. Kurita, T. Kodaira, EPR of anatase titanium dioxide under uv light irradiation, Physica Status Solidi (c). 3 (2006) 3603–3606. https://doi.org/10.1002/pssc.200672152.

[154] K. Komaguchi, H. Nakano, A. Araki, Y. Harima, Photoinduced electron transfer from anatase to rutile in partially reduced TiO2 (P-25) nanoparticles: An ESR study, Chemical Physics Letters. 428 (2006) 338–342. https://doi.org/10.1016/j.cplett.2006.07.003.

[155] I.R. Macdonald, S. Rhydderch, E. Holt, N. Grant, J.M.D. Storey, et al., EPR studies of electron and hole trapping in titania photocatalysts, Catalysis Today. 182 (2012) 39–45. https://doi.org/10.1016/j.cattod.2011.08.039.

[156] D.A. Wheeler, Y. Ling, R.J. Dillon, R.C. Fitzmorris, C. Dudzik, et al., Probing the nature of bandgap states in hydrogen-treated TiO2 nanowires, Journal of Physical Chemistry C. 117 (2013) 26821–26830. https://doi.org/10.1021/jp409857j.

[157] A.L. Attwood, D.M. Murphy, J.L. Edwards, T.A. Egerton, R.W. Harrison, An EPR study of thermally and photochemically generated oxygen radicals on hydrated and dehydrated titania surfaces, Research on Chemical Intermediates. 29 (2003) 449–465. https://doi.org/10.1163/156856703322148991.

[158] T. Berger, M. Sterrer, O. Diwald, E. Knözinger, D. Panayotov, et al., Light-induced charge separation in anatase TiO2 particles, Journal of Physical Chemistry B. 109 (2005) 6061–6068. https://doi.org/10.1021/jp0404293.

[159] Y. Nakaoka, Y. Nosaka, ESR Investigation into the effects of heat treatment and crystal structure on radicals produced over irradiated TiO2 powder, Journal of Photochemistry and Photobiology A: Chemistry. 110 (1997) 299–305. https://doi.org/10.1016/S1010-6030(97)00208-6.

[160] Y. Zeng, Y. Wang, S. Zhang, Q. Zhong, A study on the NH3-SCR performance and reaction mechanism of a cost-effective and environment-

friendly black TiO2 catalyst, Physical Chemistry Chemical Physics. 20 (2018) 22744–22752. https://doi.org/10.1039/c8cp02270d.

[161] Y. Chen, H. Yin, F. Li, J. Zhou, L. Wang, J. Wang, S. Ai, Polydopamine-sensitized WS2/black-TiO2 heterojunction for histone acetyltransferase detection with enhanced visible-light-driven photoelectrochemical activity, Chemical Engineering Journal. 393 (2020) 124707. https://doi.org/10.1016/j.cej.2020.124707.

[162] F. Zhang, G. Feng, M. Hu, Y. Huang, H. Zeng, Liquid-plasma hydrogenated synthesis of gray titania with engineered surface defects and superior photocatalytic activity, Nanomaterials. 10 (2020). https://doi.org/10.3390/nano10020342.

[163] N. Liu, X. Zhou, N.T. Nguyen, K. Peters, F. Zoller, I. Hwang, C. Schneider, M.E. Miehlich, D. Freitag, K. Meyer, D. Fattakhova-Rohlfing, P. Schmuki, Black Magic in Gray Titania: Noble-Metal-Free Photocatalytic H2 Evolution from Hydrogenated Anatase, ChemSusChem. 10 (2017) 62–67. https://doi.org/10.1002/cssc.201601264.

[164] J. Rocker, D. Cornu, E. Kieseritzky, A. Seiler, O. Bondarchuk, et al., High field electron paramagnetic resonance spectroscopy under ultrahigh vacuum conditions—a multipurpose machine to study paramagnetic species on well defined single crystal surfaces, Review of Scientific Instruments. 85 (2014) 083903. https://doi.org/10.1063/1.4893729.

[165] G. Hochstrasser, J.F. Antonini, Surface states of pristine silica surfaces, Surface Science. 32 (1972) 644–664. https://doi.org/10.1016/0039-6028(72)90192-6.

[166] J. Crank, The Mathematics of Diffusion, 2nd ed., Clarendon Press, 1975.

[167] R. Imbihl, G. Ertl, Oscillatory Kinetics in Heterogeneous Catalysis, Chemical Reviews. 95 (1995) 697–733. https://doi.org/10.1021/cr00035a012.

[168] G. Ertl, Reactions at Surfaces: From Atoms to Complexity (Nobel Lecture), Angewandte Chemie International Edition. 47 (2008) 3524–3535. https://doi.org/10.1002/anie.200800480.

[169] D.O. Uner, M. Pruski, T.S. King, The role of alkali promoters in Fischer-Tropsch synthesis on Ru/SiO2 surfaces, Topics in Catalysis. 2 (1995) 59–69. https://doi.org/10.1007/BF01491955.

APPENDICES

A. Sample Calculation for Pd Amount

Amount of Pd in synthesised samples were calculated as follows:

$$m_{TiO_2(P25)} = 4.0015\ grams$$

$$m_{(Pd(NO_3)_2)solution} = 0.1670\ grams$$

$(Pd(NO_3)_2)_{solution}$ is ~12%Pd:

$$m_{Pd} = 0.12\ x\ m_{(Pd(NO_3)_2)solution} = 0.0200\ grams$$

$$\%_{Pd} = \frac{m_{Pd}}{m_{TiO_2} + m_{Pd}}\ x\ 100 = \frac{0.0200\ gram}{4.0015 + 0.0200\ gram}\ x\ 100 = 0.5\%$$

B. TPR Experimental Procedure

1. Fill the quartz reactor with sample to be analysed.
2. Use two layers of quartz wool to stabilize the position of sample inside the U-tube reactor.
3. Close the oven around the reactor.
4. Place the reactor filled with sample to the sample port.
5. Turn on He and H_2 gas cylinder valves while shorth path, bypass routes and He inlet port are selected on Micrometrics ChemiSorb 2750.
6. Turn on Micrometrics ChemiSorb 2750, temperature controller equipment and computer.
7. Install cold trap filled with water, ice and isopropyl alcohol.
8. Cover the oven and cold trap with insulating material.
9. Start TPx software on computer and define a document for the experiment using File→Open→Sample path and fill in sample information and analysis condition as TPR.
10. Then hit Unit 1→ Start Analysis in the software.
11. Switch to sample and long paths on ChemiSorb equipment.
12. Wait until signal is stabilized.
13. Switch to H_2 gas and again wait until TCD Signal baseline is stabilized.
14. Programme temperature ramp and maximum temperature settings on temperature controller.
15. Start the signal recording and temperature programme.
16. Wait until programme is completed, then purge the system with He: all the long and shorth paths and sample and bypass paths.
17. Save the TCD signal recording data.
18. Disconnect reactor and cold trap after bypass and shorth paths are selected.
19. Turn off the computer, temperature controller and TPx system.
20. Close the valves on gas cylinders.

C. ESR Experimental Procedure

1. Load the sample to ESR tube at a volume specified by Bruker (at least 30mm sample height is needed in tube from the bottom and place an o-ring at 96mm above from bottom).
2. Turn ESR on using the switch on backside of the machine.
3. Start microESR software.
4. On Spectrometer tab; specify file name, single or multiple runs, magnetic field sweep range, microwave power, modulation amplitude, digital gain and number of scan values.
5. On Tuning tab, hit Auto Tune and Tune buttons.
6. Wait until sample is tuned and light on the screen turn to green from red.
7. Click on Start Sweep and wait until experiment is done.
8. Turn off the software, ESR computer and machine.
9. Disconnect ESR tube.

D. NMR Experimental Procedure

1. Turn on the NMR Spectrometer, computer and Expert Software.
2. Choose ^{1}H experiment on software and perform shimming procedure with D_2O.
3. Then, load the sample in NMR tube at a height specified by manufacturer using the NMR sample height adjusting tool.
4. Install NMR tube into the spectrometer.
5. Specify ^{1}H, T_1 (inversion recovery) or T_2 (decay) experimental parameters and click on run button.
6. When the experiment is done, turn off the software.
7. Disconnect NMR tube.
8. Turn off the spectrometer.

E. CO Catalytic Test Procedure

1. Fill the reactor with catalyst to be analysed and connect to CO oxidation setup.
2. Start air pump and CO gas inlet at desired values when the gas goes through the bypass line.
3. CO gas flow rate can be fixed with MKS Mass Flow Controller and its readout.
4. Calibration of readout should be done by soap-bubble flowmeter, separately.
5. Set reactor inlet flow rate by the valve at the mixer outlet.
6. The value of the flow here can be checked by soap bubble flowmeter prior to experiment.
7. For dark experiments cover the reactor with the box with reflective inner walls
8. For UV irradiated experiments turn UV light on.
9. Turn on computer and gas analyser.
10. On the front panel of CO analyser turn on the CO and CO_2 detectors by the respective switches.
11. Select appropriate detector configuration (for CO and CO_2 one should select SV3 path)
12. Start Dali08 computer programme.
13. CO and CO_2 analysis data starts to be recorded immediately.
14. Wait until CO and CO_2 ppm and %s reach a steady value.
15. Then turn the from bypass to reactor line.
16. If needed turn the heater on at desired temperature and keep the actual temperature reached by an external thermocouple.
17. At any temperature one should wait around 20 minutes for steady state to be reached.

F. Quantitative Analysis of TPR

Calibration of TPR peaks were done using Ag_2O. Ag_2O inside the TPR reactor with a mass of 0.0235 grams was reduced showing a peak at 129°C. Peak temperature is in the range recorded by Micrometrics which is $119 \mp 15°C$.
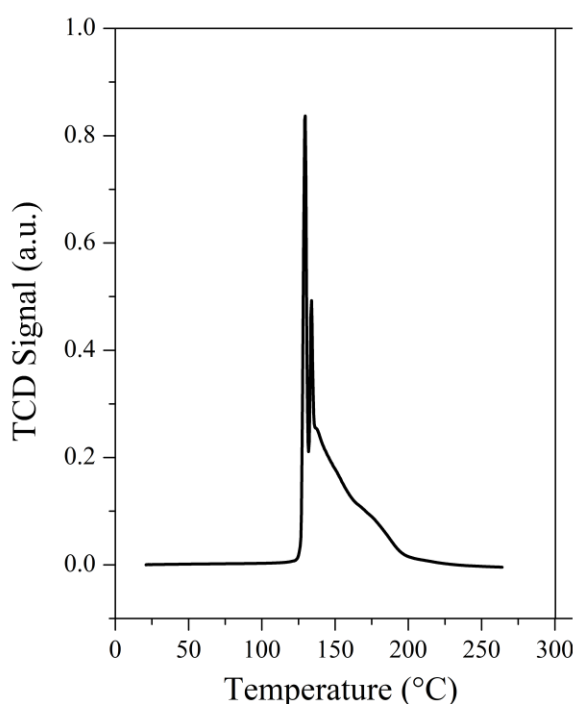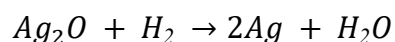

Figure F.1. Silver oxide TPR calibration curve

In order to find consumed H_2 amount during TPR, first calibration is done using Ag_2O. Reduction of Ag_2O gives a single peak at TPR, the area of this peak can be used to determine how much H_2 is used, since 1 mol H_2 is needed to reduce 1 mol Ag_2O:

$$Ag_2O \ + \ H_2 \ \rightarrow 2Ag \ + \ H_2O$$

Sample mass: 0.0235g

Sample mole: $\dfrac{0.235g}{231.735 \ g \ Ag_2O/mol} = 1.01*10^{-4}$ mol

H$_2$ needed to be used to reduce all silver-oxide: $1.01*10^{-4}$ mol

Peak area (found by OriginLab Peak Fit Tool): 10.73

Calibration $= \dfrac{1.01*10^{-4}mol}{10.73 area} = 9.45*10^{-6}$ mol/area

Each Temperature Programmed Reduction peak was fitted using OriginLab Peak Fit tool using Gaussian-Lorentz Cross Product Function given by the formula (the steps of peak fitting is explained in Appendix G):

$$y = y_0 + \frac{A}{1 + \dfrac{e^{\frac{0.5(1-s)(x-x_c)^2}{w^2}}s(x-xc)^2}{w^2}}$$

where y_0 is base, x_c is center, A is amplitude, w is width, s is shape and taken as 1.
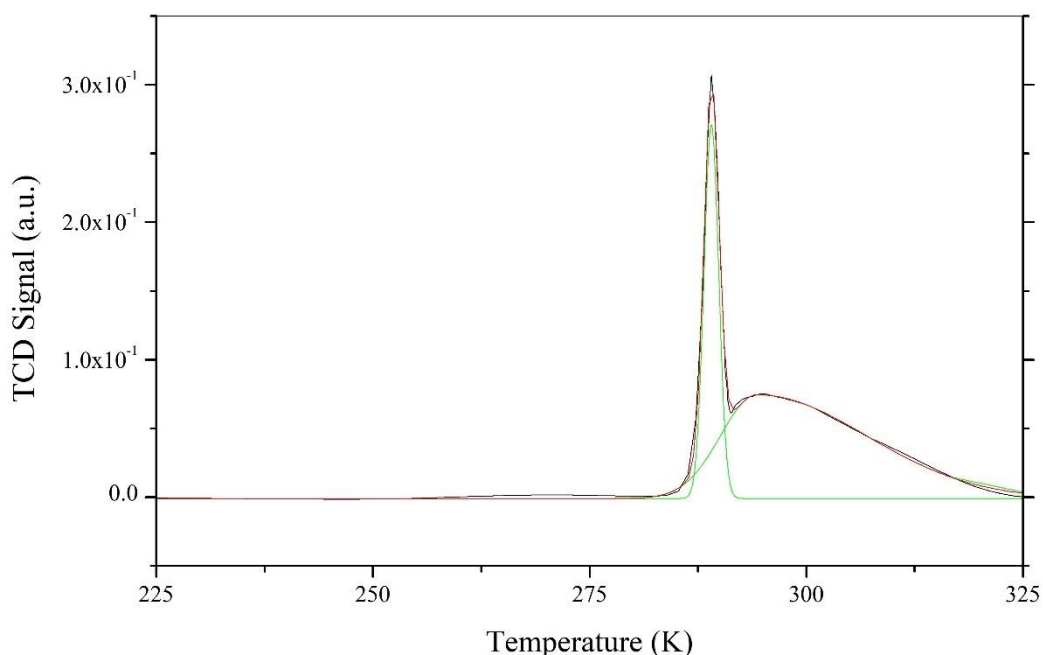
An example fit for 1%Pd/TiO$_2$ is given below:

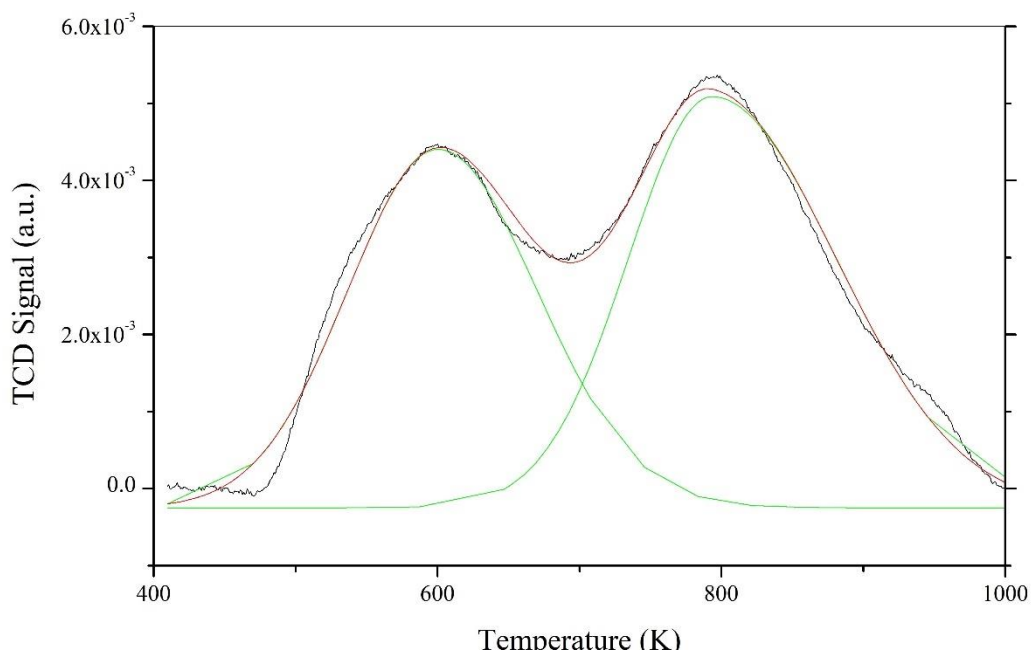Figure F.2. OriginLab 1%Pd/TiO$_2$ TPR peak fitting between 225-325K

Figure F.3. OriginLab 1%Pd/TiO$_2$ TPR peak fitting between 400-100K

Quantitative TPR analysis to find amount of hydrogen consumed and percent of titania reduced during the experiment was carried out using silver-oxide calibration explained above and the fitted areas of respective peaks. Results of quantitative analysis for 1%Pd/TiO$_2$ is given in Table F.1:

Table F.1 Quantitative TPR Analysis for 1%Pd/TiO$_2$

Peak Temperature	280K	341K	
Amount of Hydrogen Consumed or Released	5.58E-06	4.79E-07	
Amount of Pd Present in the Sample (moles)	5.14E-06	5.14E-06	
Hydrogen Consumed per Pd (mol/mol)	1.09	-	
PdHx Stoichiometry	-	PdH$_{0.19}$	
Peak Temperature	300K	595K	796K
Amount of Hydrogen Consumed	6.84E-04	6.84E-04	6.84E-04
Amount of TiO$_2$ Reduced to Ti$_2$O$_3$ (moles)	3.06E-05	1.50E-05	1.88E-05
Percent TiO$_3$ Reduced (%)	4.48	2.19	2.74

H/Pd (mol/mol) values for $\beta - PdH$ phase formed on each Pd/TiO_2 sample was calculated by quantitative analysis of $\beta - PdH$ decomposition TPR peak with the following analysis:

$$Calibration = 9.45 \; x \; 10^{-6} \; mol \; H_2/ \; area$$

$$Mol \; H \; desorbed \; in \; PdH \; peak = Calibration \left(\frac{mol \; H_2}{area}\right) * Area * \frac{2 \; mol \; H}{1 \; mol \; H_2}$$

$$Mol \; Pd \; in \; TPR \; sample = \frac{x \; (\%)Pd \; loading}{100 \; g \; catalyst} * \frac{1 \; mol \; Pd}{106.42 \; g \; Pd} * g \; catalyst$$

$$\frac{H}{Pd}\left(\frac{mol}{mol}\right) = \frac{moles \; of \; H \; desorbed \; in \; PdH \; peak}{moles \; of \; Pd \; in \; TPR \; sample}$$

Table F.2 H/Pd Calculation Results

Pd loading (%)	TPR PdH Peak Area	Mol H desorbed in PdH Peak	Gram catalyst	Mol H/ gram catalyst	Mol Pd in TPR sample	Mol Pd/ gram catalyst	H/Pd
0.5	0.01072	2.03E-07	0.049	4.16E-06	2.29E-06	4.70E-05	0.09
1	0.04705	8.90E-07	0.050	1.78E-05	4.70E-06	9.40E-05	0.19
2	0.14515	2.75E-06	0.040	6.87E-05	7.52E-06	1.88E-04	0.37
5	0.50414	9.54E-06	0.050	1.91E-04	2.35E-05	4.70E-04	0.41
10	1.07896	2.04E-05	0.041	4.95E-04	3.87E-05	9.40E-04	0.53

G. Steps of TPR Peak Fitting

1. Transfer the TPR profile data to OriginLab.
2. Plot the profile with Plot>Line option.
3. Click on Analysis Tab>Peak Analysis>Open Dialog.
4. On the pop-up window select Peak Fitting.
5. Then apply baseline subtraction if needed.
6. The peak points should be selected by add peak option.
7. Then by Fit Control option, one can choose fitting formula and other parameters.
8. Then fit is run until results converge.

H. ESR Simulation

ESR spectra obtained was simulated with MATLAB software Easy-spin package. The experimental parameters such as band frequency of the spectrometer, magnetic field range, modulation amplitude and ambient temperature was defined as simulation parameters and kept constant. Then signals were defined with respect to g-factors, broadness and signal weight (intensity). These parameters were changed and additional signals were added until simulated signals correspond to experimental ESR spectra.

A sample code is presented below:

```
Sys1.g = 2.00; %Oxygen vacancy
Sys1.lwpp = 3; %Broadness of oxygen vacancy signal
Sys1.weight = 1;
Sys2.g = 1.97; %Ti+3
Sys2.lwpp = 0.8; %Broadness of Ti+3 signal
Sys2.weight = 0.006;
Exp.mwFreq = 9.5; %X-band
Exp.Range = [320.1 369.7]; %Magnetic Field Range in mT
Exp.Temperature = 298; %Temperature in Kelvin
Exp.ModAmp = 0.4; %0.4 mT (4 G) modulation amplitude, peak-to-peak
pepper ({Sys1, Sys2}
```